Ultrafast electron diffuse scattering and its application to 2D materials

Mark J. Stern

Doctor of Philosophy

Department of Physics

McGill University

Montréal, Québec, Canada

2018-08-15

A thesis submitted to McGill University in partial fulfillment of the requirements of the degree of Doctor of Philosophy

©Mark J. Stern, 2018

For Dana,

you are amazing

ACKNOWLEDGEMENTS

This work was made possible by the unwavering and dedicated support of my friends, family and colleagues. Most importantly, I would like to thank, Dr. Bradley Siwick. I could not have asked for a more brilliant or considerate supervisor. His encouragement and understanding through many difficult months allowed me to make something great from my time at McGill. This is also true of my fellow graduate students, Martin Otto and Laurent René de Cotret, who are outstanding physicists and great friends. I would also like to thank the past members of the Siwick Group, especially Dr. Vance Morrison and Dr. Robert Chatelain for their companionship and teaching me how to use their home built ultrafast diffractometer. I also extend my thanks to the past and present members of the Kambhampati Group for hundreds of interesting and hilarious conversations. I am also grateful for several inspiring discussions with Dr. Mark Sutton as well as the aid I recieved from many of McGill's technical staff including Richard Talbot, Pascal Bourseguin, Jean-Philippe Guay, Richard Rossi, Weihua Wang and Jeannie Mui. A special thanks goes to my parents and my sisters for being patient and supportive through nearly a decade of graduate school. I must also thank the McGill University Physics Department, for being my home for so long. And finally, I lovingly thank my wife, Dana, who just makes everything in life better.

ABSTRACT

The nature of the couplings within and between lattice and charge degrees of freedom is central to condensed matter and materials physics. Despite their fundamental role, detailed momentum-dependent information on the strength of electron-phonon and phonon-phonon couplings across all momenta has proved elusive. Ultrafast electron diffuse scattering provides the answer by measuring momentum-dependent phonon population dynamics similar to how time and angle resolved photoemission spectroscopy views the momentum-dependent occupation dynamics of electronic states. This method proves particularly effective in the study of 2D materials. A sophisticated analysis applied to ultrafast electron scattering measurements of graphite, follows the cascade of electron-phonon and phonon-phonon couplings after pulsed laser excitation in this well studied benchmark system. In a similar experiment on titanium diselenide, electron-phonon coupling is measured by observing the effect of photoexcitation on the renormalized phonon frequencies with the characteristic momentum of titanium diselenide's charge density wave transition. Through its sensitivity to transient phonon occupancies and frequencies, ultrafast electron diffuse scattering is a novel and powerful method to unravel the physics of complex phases and properties determined through interplay between the electron and lattice systems.

ABRÉGÉ

La nature du couplage entre le réseau d'atomes et les porteurs de charges d'un cristal est centrale au domaine de la physique de la matière condensée. Malgré leurs rôles fondamentaux, les couplages électron-phonon et phonon-phonon demeurent mystérieux. La diffraction ultrarapide diffusé par électrons permet de répondre aux questions concernant l'occupation des populations phononiques dans l'entièreté de l'espace réciproque. Plus spécifiquement, les excitations optiques sur un cristal de graphite, initiées par une impulsion laser femtoseconde, génèrent une population électronique excitée particulière, appelée cônes de Dirac. Ces excitations creés un plasma d'électrons et de trous de densité variable, contrôlée par l'intensité de l'impulsion laser. Cette thèse présente une analyse sophistiquée de données de diffraction ultrarapide diffusé par électrons faisant la lumière sur la relaxation du système électronique excité par impulsion ultrarapide, passant par le couplage avec le réseau d'atomes, puis finissant en relaxation des modes phononiques avec l'environnement. Dans le cas du disélénure de titane (TiSe2), le couplage électron-phonon est mesuré de façon complètement différente; en observant l'effet de la photo-excitation sur les fréquences de phonons renormalisées aux vecteurs d'ondes caractéristiques de la phase d'ondes de charges de $TiSe_2$. À travers la sensitivité aux occupations phononiques temporaires, la diffraction ultrarapide diffusé par électrons permet de décortiquer la physique des phases complexes de la matière, et d'élucider la relation entre le système électronique et le réseau d'atomes.

TABLE OF CONTENTS

. ii

ACKNOWLEDGEMENTS iii

ABSTRACT iv

ABRÉGÉ v

LIST OF FIGURES viii

Preface 1

1 Phonons and their interactions 3

1.1 Introduction 7
1.2 Crystals and vibrations 9
1.3 Calculating the phonon dispersion and polarizations 15
1.4 Density functional theory 20
1.5 Electron-phonon and phonon-phonon coupling 23

2 Scattering theory 27

2.1 Scattered waves 27
2.2 The first Born approximation 29
2.3 Electron scattering 30
2.4 Scattering from a crystal 32
2.5 Structure factors 36
2.6 Application and analysis 39
2.7 Diffuse scattering selection rules 42

3 Experimental methods 46

3.1 Pump probe techniques 46
3.2 Ultrafast electron diffraction 47
3.3 Optical Setup and pulse generation 51

3.4 RF cavity and synchronization 53
3.5 Sample chamber 55

4 Phonon couplings in Graphite 60

4.1 Structure of graphite 61
4.2 Photoexcitation dynamics 65
4.3 UEDS results 73
4.4 Strongly coupled optical modes 75
4.5 Acoustic modes 80

5 Phonon renormalization in titanium diselenide 86

5.1 Properties of $TiSe_2$ 87
5.2 UEDS results 90
5.3 Impulsive phonon hardening 94
5.4 Conclusions and outlook 96

LIST OF FIGURES

Figure page

1–1 Interplay between microscopic degrees of freedom shared by electron, lattice and spin systems leads to a complex zoology of ordered phases and diverse electronic properties. 4

1–2 A simplified diagram of a pump-probe electron diffraction experiment. An ultrashort pump (laser) pulse strikes the sample, initiating some physical process of interest at t=0, followed by a probe pulse that captures a snapshot at a particular time delay after excitation, Δt. A series of ultrafast snapshots constitute an ultra high speed 'movie' of the process. In the case of electron diffraction, the probe pulse diffracts off the sample producing elastic scattering peaks as well as inelastic or diffuse scattering at all other scattering angles. The position and intensity of the peaks encode the atomic structure of the sample and the diffuse scattering features are determined by vibrations. 5

1–3 Geometry of a hexagonal lattice. (Left) The real space unit cell and lattice vectors with $|\vec{a_1}| = |\vec{a}_2| = a$ and $|\vec{a_3}| = c$. (Right) The Brillouin zone and reciprocal lattice vectors with the high symmetry points labelled. Figure taken with permission from Reference [1]. . 11

2–1 Scattering geometry diagram for an incident plane wave Ψ_0, showing the definitions for the distances $\vec{r}$ and $\vec{r}\,'$. 29

2–2 Visualization of the Laue condition for elastic scattering. If the Ewald sphere, shown as the blue circle, intersects with a reciprocal lattice point (black dots), a Bragg peak may appear at the scattering vector, $\vec{k} - \vec{k}_0 = \vec{q} = \vec{H}$, as long as the geometric structure factor, $F_0(\vec{q})$, is not zero. The Ewald sphere is much flatter (low curvature) for short wavelength electrons compared to x-rays. Therefore more Bragg peaks corresponding to a single plane of reciprocal lattice vectors will be visible in a single diffraction pattern. . . . 38

2–3 Diffuse scattering geometry. (a) Vector diagram of the reduced wave vector, $\vec{k} = \vec{q} - \vec{H}$, overlaying a diffraction pattern of graphite. Select Bragg peaks are labelled by Miller indices, using the primitive reciprocal lattice vectors as a basis. (b) The structure factor map for the TA mode of graphite, the white dots indicate the locations of Bragg peaks (Γ points) and the hexagons show the BZ edges. The first diffuse scattering rule is demonstrated by the bowtie shaped feature parallel to the [110] lattice vector. The phonon polarizations that determine the third diffuse scattering rule are shown constructively and destructively interfering at $\vec{q}_1$ near a bright Bragg peak, [110], and at $\vec{q}_2$ near a weak Bragg peak, [200], respectively. 43

3–1 Reversal of the space charge effect on electron pulses using a radio frequency cavity operating in a transverse magnetic mode. When synchronized correctly, the cavity fields (shown with blue arrows) invert the position-momentum (z-p_z) distribution of the electron pulse. After the RF cavity interaction, the electron pulse ballistically compresses itself during propagation. 49

3–2 Schematic diagram of the UED instrument. The laser system outputs 3 mJ, 35fs infrared pulses which are split into two separate paths. The first path is followed by the pump pulse and is variably delayed by a retroreflector mounted on a motorized linear stage before arriving at the specimen. The second path provides the electron probe pulse by first frequency tripling to a UV wavelength by non-linear optics before photoexciting the copper cathode to emit electrons. The electron beam is accelerated by a 95 kV DC field and travels through the RF compression cavity (which is synchronized to the oscillator output), steered and focused by magnetic solenoid lenses, towards the specimen. Last, the diffraction pattern is detected at a CCD camera which can capture the total scattering from many probe pulses in a single exposure. 50

3–3 Image and drawing of the sample chamber with the various control features and important components labelled. The electron beam direction is shown in blue. 56

3–4 Picture and sectioned drawing of the spring loaded wedge mechanism for angluar control about the transverse axis (tilt). Linear motion of the wedge controlled by the screw action stage at the lowest end of the chamber modulates the angle with up to 35° of range. 57

3–5 Top down sectioned view of the sample chamber. The electron beamline is shown in blue and the laser beamline is shown in red. the electron beam is steered through the sample with a magnetic solenoid lens. The pump beam is steered into the chamber using exterior optics and focused onto a point a few mm left of the sample depending on the desired beam size and fluence. The outgoing laser beam is measured by a photodiode as an alignment diagnostic tool. The mirrors shown in the diagram (7mm dia., silver) are fixed and mounted inside the vacuum chamber. 58

4–1 The structure of graphite with AB stacking. $a = 2.46$ Å, $c/2 = 3.35$ Å. The solid black lines represent strong covalent bonds and the dashed lines represent Van der Walls forces. 62

4–2 Electron band structure of graphite in the first BZ near ϵ_F showing Dirac cones at the K points. Taken with permission from Reference [2]. 64

4–3 (Top) Experimental (inelastic x-ray scattering) and calculated phonon dispersion of the optical modes of graphite showing Kohn anomalies at the Γ and K points. (Bottom) Full phonon dispersion of graphite calculated using density functional theory. Figures taken with permission from References [3] and [4]. 65

4–4 Sketch of the in-plane electronic band structure of graphite at the Fermi energy and close to the K point where the valence and conduction bands slightly overlap. Arrows indicate possible direct (DOT) and indirect (IOT) optical transitions induced by the probe pulse. (b) Brillouin zone perpendicular to the [001] axis. Nested vectors of the Fermi surface are located around the K points. Arrows mark possible scattering events of electrons and correspond to wave vector changes that are confined to the vicinity of the Γ and K points. Figure taken with permission from Reference [5]. 66

4–5 Main stages of energy relaxation of photoexcited carriers. First the high energy ($\epsilon = hf/2$) carriers lose energy to carrier-carrier and phonon scattering. These processes lead to fast thermalization, producing a relatively long-lived hot carrier distribution. In the second stage, electron-lattice cooling mediated by phonons takes place over longer time scales relaxing the hot carrier distribution back to equilibrium, T_0. Figure taken with permission from Reference [6]. 67

4–6 (a) Energy (E_{bin}) and momentum ($k_{\|}$) resolved photoemission intensity around the Dirac cone (no pump). (b) Equilibrium high-resolution spectrum. (Inset) Brillouin zone with measurement direction (dashed red line). (c)-(e) Spectra taken at increasing time delays. (f)-(h) Change with respect to the spectrum before the pump pulse (difference spectra). Figure taken with permission from Reference [7]. 69

4–7 (a-b) Electron energy distribution curves derived from trARPES data illustrating the deviation from a thermalized electron distribution shortly after photoexcitation. (c) Nonthermal component of the energy distribution curves as a function of t. (d) Electron temperature transients derived from Fermi-Dirac fits to the energy distribution curves. Figure taken with permission from Reference [8]. . . 70

4–8 TRR graphite results, showing temporal dynamics of the Γ-E_{2g} phonon following pump excitation. (a) Experimental anti-Stokes Raman intensity, which is proportional to the phonon mode population. (b) Measured shifts of the Γ-E_{2g} mode frequency. (c) Temperature of the Γ-E_{2g} phonons inferred from the mode population in (a). Figure taken with permission from Reference [9]. 71

4–9 Phonon dispersion of graphite with the strongly coupled optical modes indicated. The orange bars indicate half the energy of the K-A_1' and Γ-E_{2g} modes. The dominant energy and momentum-conserving decay pathways are indicated with coloured arrows. For example, the green arrows labelled A_1':TA-LA on the left represent the decay from the strongly coupled A_1' mode at K to both TA and LA modes at the midpoint of the Γ-K line. Dotted arrows should be thought of as going in the opposite momentum direction. Side bar (red) provides a schematic of the non-equilibrium LA/TA phonon distribution produced through the decay of Γ-E_{2g} and K-A_1' phonons. Figure taken with permission from Reference [10]. 72

4–10 $\Delta_f I(\vec{q}, 100\text{ps})$ at various steps in the image processing procedure. a) shows the raw diffraction pattern after averaging the experimental repetitions. Artifacts from the beam block and camera read out are indicated. b) Diffraction pattern after masking of the artificial signals. c) Pattern after six-fold averaging. d) Pattern after Gaussian smoothing. 75

4–11 Evolution of $\Delta_f I(\vec{q}, \tau)$ following photo-excitation of graphite. The dramatic changes reflect the non-equilibrium phonon populations and their time dependence. a) Raw diffraction pattern of graphite with select BZs indicated with dashed lines. b) Differential scattering flat-field at a time before optical excitation indicating signal-to-noise. c) At early times the diffuse intensity provides a map of the relative strength of the q-dependent EPC coupling through the increased occupancy of strongly-coupled modes. Peaks in $\Delta_f I(\vec{q}, 0.5$ ps) at certain $K-$points (circled) result from the increase in K-A_1' population. Strong coupling to the entire transverse acoustic (TO) branch is evident in the vicinity of [200] as ridges of intensity radiating from Γ to K points. (c) By 1.5 ps, a halo of scattered intensity the around the [110] peak appears due to dominant anharmonic decay pathways of the strongly coupled modes. (b) Scattered intensity collects along Γ-M lines perpendicular to the scattering vector. By diffuse scattering selection rules 1 and 2 this is scattering from the TA mode. These dynamics demonstrate interband and intraband pathways from the mid-BZ TA and LA modes. By 100 ps (c) the intensity has tightened around the Γ-M lines lines and the diffuse intensity now has the same shape as the TA structure factor map in Figure 4–12(upper right). This steady state increase in TA mode occupancy is consistent with the lack of allowed anharmonic decay pathways for transverse acoustic modes [11, 12]. 76

4–12 Visualizing momentum dependance of one-phonon structure factors. (Left) Numerically computed structure factor maps for the acoustic modes in graphite. TO mode activity matching the early diffuse scattering features in Figure 4–11(c) is outlined in red. The shape of the TA mode activity features match the shape of the diffuse scattering features after 5 ps in Figure 4–11(e-f). (Right) Phonon dispersion curves weighted by structure factor. The darker curves have stronger structure factors along the paths indicated in the structure factor map insets, allowing the mode activity to be easily determined along high symmetry lines and at high symmetry points (note that light grey is zero for these curves). Along the magenta path, for example, the LA mode is active along both Γ-M and Γ-K lines where the LA mode is only active on the Γ-K line. In contrast, the TA mode is the only dominant mode along most of the pink path. The paths with only one dominant mode indicate where single mode occupancy dynamics can be extracted directly via Eq. 2.30. 79

4–13 Ultrafast electron diffuse scattering at early times. a) Intensity of the [110] Bragg peak showing non-exponential Debye-Waller dynamics [13]. b) $\Delta_f I(\vec{q}, \tau)$ at select points in the BZ (inset) and the E_{2g} occupancy dyanamics measured with TR-Raman[9] shown in grey. The rate of increase in the the population of the TO K-A_1' phonon from electronic coupling (red, 280 fs) is faster than that for the Γ-E_{2g} (cyan, 430 fs) and matches the fast Bragg peak dynamics. The population K-LO phonons (green, 730 fs) rises much slower that both TO K-A_1' and Γ-E_{2g} phonons. The rise in diffuse intensity at the M-point (blue, 2.1 ps) is almost an order of magnitude slower than that associated with the TO K-A_1' phonon. The slow timescale decay evident in the Bragg peak and reported in earlier ARPES measurements [14] does not emerge from the dynamics of any single mode, but is a composite of the decay in population of the strongly coupled optical modes (e.g. red, 1.7 ps) and the increase in population of all other modes. 81

4–14 Transient differential phonon population spectra. Blue arrows indicate anharmonic decay from optical modes to mid-BZ acoustic modes. Red arrows indicate inter and intraband decay of acoustic modes. (a) TA occupation dynamics along the Γ-M line. By 5 ps, a peak appears around $0.5M$. Population then collects near Γ and M points.(b) (a) TA occupation dynamics along the Γ-K line. In contrast with (a), the population decreases near the BZ edge. (a) LA occupation dynamics along the Γ-K line. The rapid increase near K is due to the TO mode which strongly couples to the photoexcited electron system and has a significant structure factor at these scattering vectors 4–11(lower right). Subsequently, LA mode population decreases everywhere along the Γ-K line. 85

5–1 The structure of $TiSe_2$. (a) Atomic configuration of two stacked unit cells. (b) Brillouin zones in the normal phase (thick outline) and the CDW phase (thin outline). Red arrows indicate the in-plane wavevectors of the CDW and the gray contours illustrate the topology of the equi-energy contours. (c) Electronic structure in the normal phase. There is an indirect band gap across Γ to M and a negative indirect band gap across Γ to L. Excitonic behaviour at these wave vectors provides an alternate mechanism for the CDW transition. Figures taken with permission from References [15] and [16] 88

5–2 Simulated phonon dispersion curves of $TiSe_2$, showing the severity of the TA mode renormalization as a function of temperature. In order to quantitatively calculate the CDW transition temperature, the Fermi-Dirac distribution is used to smear the electronic functions, where the smearing factor takes on a physical meaning to directly increase the electronic temperature and has the effect of increasing the TA phonon frequency at the M and L points. . . . 90

5–3 Static diffraction patterns of $TiSe_2$. (Left) Diffraction at normal incidence along [001]. Select BZs indicated by reciprocal lattice coordinates. (Right) Diffraction along $[10\bar{1}]$, the BZ edge is indicated with M and L high symmetry points. 92

5–4 Evolution of $\Delta_f I(\vec{q}, \tau)$ following photo-excitation of $TiSe_2$. By 0.5 ps, negative diffuse scattering features (green) appear at M-points surrounding the [110] family of peaks forming a gear-shaped pattern. Through 1 and 2 ps, the M-point signals fade into a uniform diffuse scattering increase at all points away from the Bragg peaks. 93

5–5 Fractional scattered intensity changes. (a) Bragg peak dynamics showing showing Debye-Waller suppression. (b) Diffuse scattering dynamics at high symmetry points. All three curves increase during the first 2 ps after photoexcitation, corresponding to an overall phonon occupancy increase due to coupling with photoexcited electrons. An extremely fast dip in diffuse intensity that recovers in about 1 ps appears at M points where the TA mode is active and dominant as shown in the computed weighted dispersion curve (c). 95

PREFACE

The author, Mark J. Stern, affirms that the work presented in this thesis constitutes original scholarship and a distinct contribution to the field of condensed matter physics. The experimental technique which is the subject of this work, ultrafast electron diffuse scattering, produces time and momentum resolved diffuse scattering patterns from which the time resolved phonon occupancy spectra for individual phonon modes in graphite are extracted revealing the details of electron-phonon and phonon-phonon couplings. No other technique exists which is sensitive to the transient amplitude and frequency of phonon modes with non-zero momentum, so the measurement alone is a new and impactful contribution. Moreover, the technique's sensitivity to the energy of phonon modes at high symmetry points reveals a near instantaneous stiffening of phonon modes related to the charge density wave transition in titanium diselenide and the screening of phonons by electrons. This is also an unprecedented result due to the location of the characteristic charge density wave momentum at the edge of the Brillouin zone, the vanishingly small size of the signal and the extremely short duration of the effect. Both of these results reveal novel insights into charge-lattice interactions in 2D materials and are a direct product of the experimental and theoretical work of the author.

The specific contributions of the author and co-workers to the work presented in this thesis are summarized here. The experiments were performed with a home

built ultrafast electron diffractometer configured mainly by Dr. Vance R. Morrison and Dr. Robert P. Chatelain. Upgrades to the instrument, enabling angular sample manipulation and improvements to the laser beam line were designed and installed by the author with support from professional technicians in the McGill Physics Department, Richard Talbot and Pascal Bourseguin, as well as co-workers Martin R. Otto and Laurent P. René de Cotret. The experiments on graphite were performed by Dr. Robert Chatelain and the experiments on titanium diselenide were performed by the author with support from Martin R. Otto and Laurent P. René de Cotret. The data processing was greatly aided by the *iris* software package developed by Laurent P. René de Cotret. The development and execution of the data analysis are solely the work of the author. The interpretation and discussion of the results were written by the author with support from Dr. Mark Sutton. Finally, support from the author's graduate supervisor, Dr. Bradley J. Siwick, was generously given throughout.

CHAPTER 1
Phonons and their interactions

A thorough understanding of the properties of condensed matter is built upon the fundamental concepts of the atomic lattice and electronic structure. The simplest theoretical models, built to explain basic thermal and electronic properties of materials, restrict their focus to isolated electrons, spins or phonons, the building blocks of these systems, assuming no interactions occur. But in order to describe more complex and subtle phenomena in solid-state physics, such as electrical and thermal resistance in semiconductors [17] or conventional superconductivity [18], charge/lattice couplings must not be neglected (Figure 1–1). An excitation in either system can rapidly provoke other excitations, exchanges that can occur on time scales faster than a picosecond (10^{-12} s).

Many methods and techniques have been designed to the study electronic/lattice structure and dynamics. Elastic x-ray and electron diffraction, for example, are the primary methods for solving the structure of crystalline materials where inelastic x-ray scattering provides information on electronic structure and both electronic and lattice excitations [19, 20]. Similarly, elastic neutron scattering is used to study the arrangement of electron spins and unpaired electron density distributions where inelastic electron scattering probes excitations and spin correlations [21]. Angle resolved photoemission spectroscopy (ARPES) directly maps the density of single-particle electronic excitations in momentum space [22]

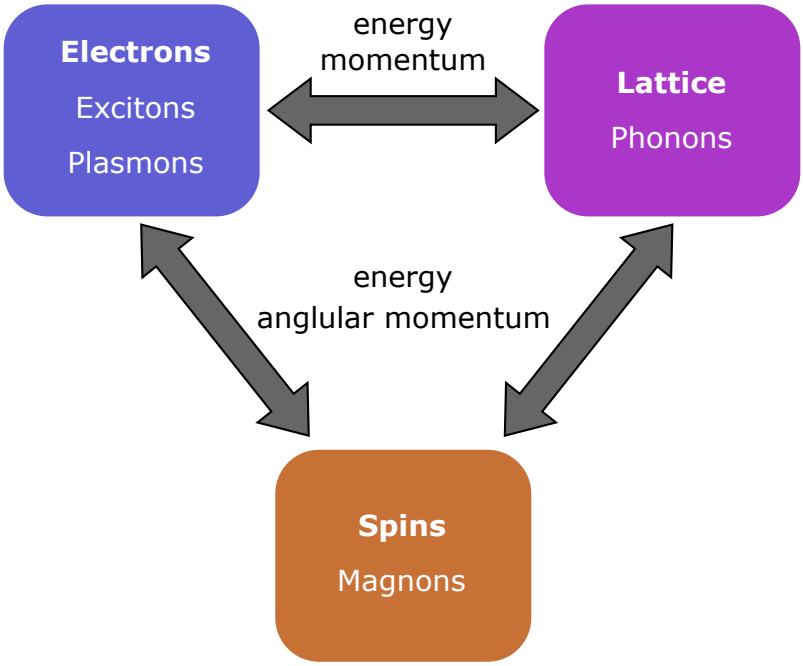

Figure 1–1: Interplay between microscopic degrees of freedom shared by electron, lattice and spin systems leads to a complex zoology of ordered phases and diverse electronic properties.

and Raman/Brillouin spectroscopy is used to observe molecular and crystal vibrations [23]. However, conventional techniques can only provide indirect information on the strength of interactions and the lack temporal resolution needed to follow these exchanges in real time. Phonon-phonon couplings, in particular, have typically been the province of theory or molecular dynamics simulations [24, 25] only due to the lack of techniques capable of probing these interactions in any substantial detail. During the last few decades, the development of femtosecond laser technology has delivered the capability to observe non-equilibrium effects of electron-phonon and phonon-phonon coupling by implementing *pump-probe*

techniques which achieve time resolution by manipulating an adjustible delay between an excitation pulse (pump) pulse and an ultrashort ($\sim 10^{-14}$ s) interrogation (probe) pulse (Figure 1–2).

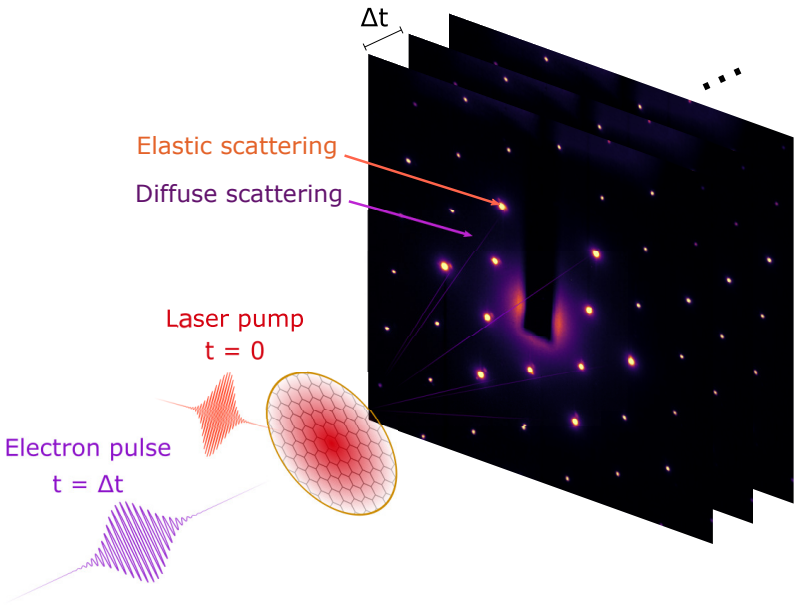

Figure 1–2: A simplified diagram of a pump-probe electron diffraction experiment. An ultrashort pump (laser) pulse strikes the sample, initiating some physical process of interest at t=0, followed by a probe pulse that captures a snapshot at a particular time delay after excitation, Δt. A series of ultrafast snapshots constitute an ultra high speed 'movie' of the process. In the case of electron diffraction, the probe pulse diffracts off the sample producing elastic scattering peaks as well as inelastic or diffuse scattering at all other scattering angles. The position and intensity of the peaks encode the atomic structure of the sample and the diffuse scattering features are determined by vibrations.

Several of the conventional techniques mentioned above can be reconfigured into a pump-probe geometry providing ultrafast temporal resolution. Femtosecond lasers can be applied to conventional spectroscopies to observe excitations in

real time [26]. Ultrashort x-ray pulses can be generated for pump-probe x-ray scattering experiments using x-ray free electron lasers [27, 28] and a femtosecond laser can be used to photogenerate an ultrashort electron pulse [29] to observe transient structural changes through ultrafast diffraction. In this way, exchanges between electronic and lattice excitations can be measured as they occur, but any one method can only provide a piece of the full dynamically coupled electron-lattice picture depending on which excitations are observable using that technique. Electronic excitations can be tracked with time and energy resolution across large ranges of momentum using time resolved ARPES (trARPES) providing near complete information on the electronic part of the dynamics [14, 30, 31]. Time resolved Raman (TRR) spectroscopy [31] is sensitive to lattice excitations, but can only observe phonons with near zero momentum. Notably, the time resolved excitations of the remaining phonons have traditionally been inaccessible through experiment.

This work describes a novel pump-probe technique, ultrafast electron diffuse scattering (UEDS), which provides the missing piece of the dynamic electron-lattice picture by unravelling the individual phonon mode contributions to the time-resolved diffuse scattering of bright ultrafast electron pulses across all non-zero momenta [10]. This is the first ultrafast technique sensitive to these excitations and has the potential to provide previously unattainable insights into condensed matter phenomena related to phonons and their interactions.

1.1 Introduction

The development of UEDS has grown from its parent pump-probe technique, ultrafast electron diffraction (UED), which has been typically employed with the aim of tracking changes to atomic structure through variations in *elastic* electron scattering called Bragg peaks. Figure 1–2 shows a simplified picture of how UED experiments generate a series of time stamped diffraction images that constitute a 'movie' of the photoinduced structural dynamics. UED has been immensely successful in this regard, providing deep insights in multiple domains of condensed matter physics [29, 32, 33], including electron-lattice couplings [13]. After photoexcitation, coherent lattice excitations are observed through ultrafast oscillations in Bragg peak intensity while the incoherent phonons are measured via the rapid Debye-Waller suppression of the same peaks. UEDS expands on the ability of UED to view phonon dynamics by shifting the focus from the Bragg peaks, formed by elastically scattered electrons, to the inelastically scattered electrons, often called *diffuse* scattering, which are found at all other points of a diffraction pattern (Figure 1–2). Where elastic scattering encodes information on the atomic structure and electronic charge density, diffuse scattering intensity depends on the frequency, direction and amplitude of lattice vibrations. Both forms of scattering are simultaneously measured in a UED experiment although the relative intensity of diffuse scattering is at least 10^4 times weaker at any point in a diffraction pattern. Improvements in UED beam brightness, along with advances in temporal resolution [34–36] have produced detailed measurements of diffuse scattering, not only enabling UEDS experiments, but achieving an

extremely high level of signal-to-noise, resolving diffuse intensity changes of $< 1\%$ without sacrificing temporal resolution, matching the time scale of electron-phonon and phonon-phonon coupling lifetimes [10].

UEDS captures the scattering from all phonons with momenta in the scattering plane with a single image, producing complex patterns of rapidly modulating diffuse intensity. Each experiment provides an extremely rich data set, encoding the distribution of all transient in-plane lattice-excitations as a function of pump-probe delay. Consequently, the interpretation of these patterns is highly non-trivial. A calculation of momentum dependent vibrational frequencies and more importantly the phonon polarizations proves to be invaluable to the analysis, and can be executed (in many cases) using *ab initio* techniques based in density functional perturbation theory [37]. With the equilibrium phonon system characterized, the weight of the scattering contribution from each phonon mode at each scattering angle can be calculated. Even so, the amplitude of individual vibrational modes can only be solved with an understanding of how their polarizations are related to the scattering geometry. UEDS analysis techniques, based on the results of *ab initio* computations, can decrypt the complexities of time resolved diffuse scattering data and are derived and demonstrated in this thesis.

With behaviour of lattice excitations revealed through the UEDS technique, the cascade of phonon excitations and decay can be viewed directly and the implications on electron-phonon couplings can be understood in relation to complimentary results from trARPES experiments. All the theoretical and practical information needed to understand and operate a UEDS experiment and

navigate between a time series of diffraction snapshots and phonon dynamics with momentum, time and energy (mode) resolution is presented in this work. Chapter 1 lays out the theoretical foundations for lattice vibrations, electronic structure and their interactions as well as a method for the calculation of phonon dispersions and polarizations using density functional theory. Chapter 2 includes a first-principles derivation of the relationship between diffuse electron scattering from a crystal and lattice vibrations, as well as practical methods for the extraction of phonon spectra from UEDS patterns using the theoretical basis established in the first chapter. Chapter 3 contains the details of the experimental methodology UEDS including the instrumental configuration and most recent improvements designed with UEDS in mind. Chapters 4 and 5 each present a demonstration of the UEDS technique applied to two very different 2D materials. In Chapter 4, the electron-lattice dynamics in thin film graphite are revealed through the results of a UEDS analysis as well as an unprecedented view of the anharmonic phonon decay pathways. Chapter 5 will focus on the role of electron-phonon coupling related to the charge density wave (CDW) transition in $TiSe_2$, demonstrating the direct effects of photoexcitation on the vibrational frequencies with the characteristic CDW momentum.

1.2 Crystals and vibrations

The primary goal of this introductory chapter is to lay out the fundamental theoretical descriptions of crystalline materials focusing on the necessary background needed to compute phonon frequencies and polarizations. This calculation is a necessary step in the analysis of UEDS data, as it will be used to relate the

geometry of electron scattering with the geometry of lattice vibrations. The final section will describe electron-phonon and phonon-phonon interactions, in particular the linear charge density response to a lattice distortion and its role in phonon frequency renormalization and the CDW phase transition.

The materials of interest for UEDS study are primarily crystalline solids, which have the property that their constituent atoms are periodically arranged in a Bravais lattice. That is to say that the neighbourhood around a point in the lattice will be the same as the neighbourhood of every other point under some translation [38, 39]. Any point in a crystal lattice can be written as a sum of three vectors, $\vec{R} = n_1\vec{a}_1 + n_2\vec{a}_2 + n_3\vec{a}_3$, where $\vec{a}_1$, $\vec{a}_2$ and $\vec{a}_3$ are linearly independent and called primitive vectors. The crystal's atoms will be found at fixed locations relative to any given lattice point, therefore a crystal structure is fully described by a choice of primitive vectors, $\{\vec{a}_3, \vec{a}_3, \vec{a}_3\}$, and the relative positions of the atoms within the volume defined by these vectors. This volume is called the primitive unit cell. An example of unit cell for a simple hexagonal lattice is shown in Figure 1–3(left).

'Hexagonal' is one category of crystal structures, defined by the relationships between the length of the lattice vectors and the angles between them. The materials discussed in this work, graphene, graphite and $TiSe_2$, all have hexagonal structures which have the following properties: $|\vec{a_1}| = |\vec{a}_2| \neq |\vec{a}_3|$, $\angle\vec{a_1}, \vec{a_2} = 120°$ and $\angle\vec{a_1}, \vec{a_3} = \angle\vec{a_2}, \vec{a_3} = 90°$. Since crystals are highly ordered materials, the study of crystallography employs the language of space groups which categorizes structures by their translational and point group symmetries. A comprehensive list

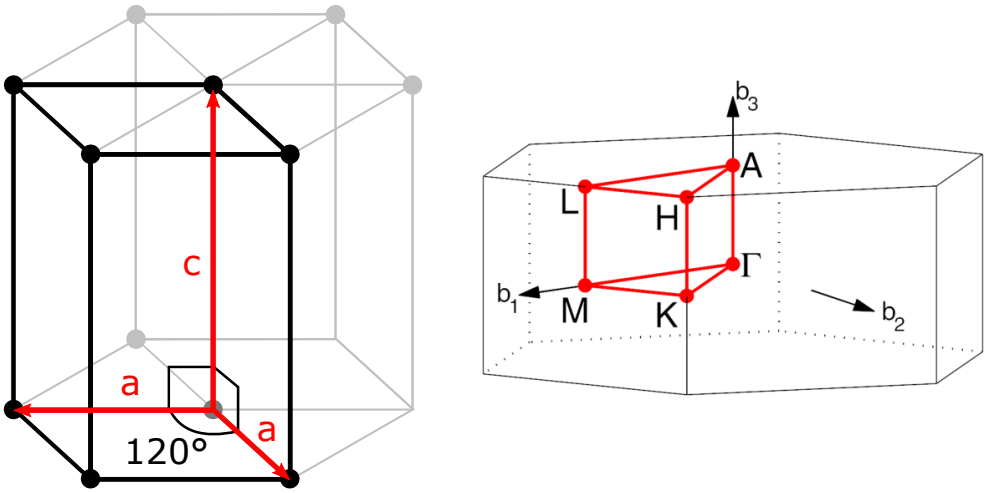

Figure 1–3: Geometry of a hexagonal lattice. (Left) The real space unit cell and lattice vectors with $|\vec{a_1}| = |\vec{a}_2| = a$ and $|\vec{a_3}| = c$. (Right) The Brillouin zone and reciprocal lattice vectors with the high symmetry points labelled. Figure taken with permission from Reference [1].

of the space groups and their properties can be found in the International Tables for Crystallography volume A [40].

The geometry of the crystal lattice can also be expressed in momentum space using a dual Bravais lattice known as the reciprocal lattice. The reciprocal and real space lattices are related through their lattice vectors by the constraint, $\vec{R} \cdot \vec{H} = 2\pi l$, where l is an integer, and $\vec{H}$ is a primitive vector of the reciprocal lattice [38]. Specifically, the reciprocal lattice primitive vectors are related to the

crystal lattice vectors by the following identities:

$$\begin{aligned}\vec{b}_1 &= 2\pi\frac{\vec{a}_2\times\vec{a}_3}{\vec{a}_1\cdot\vec{a}_2\times\vec{a}_3}\\ \vec{b}_2 &= 2\pi\frac{\vec{a}_3\times\vec{a}_1}{\vec{a}_1\cdot\vec{a}_2\times\vec{a}_3}\\ \vec{b}_3 &= 2\pi\frac{\vec{a}_1\times\vec{a}_2}{\vec{a}_1\cdot\vec{a}_2\times\vec{a}_3}\end{aligned} \tag{1.1}$$

The space of vectors that are closer to $\vec{H}$ than any other reciprocal lattice point is called the Brillouin zone (BZ), which is also a unit cell for the reciprocal lattice. The BZ for a hexagonal crystal is shown in Figure 1–3(right), showing the labels for the high symmetry points found at the center of the BZ (Γ) and at the vertices and midpoints of the BZ edges (M, K, L, H, A). The reciprocal lattice vectors predict where elastic scattering from a crystal will occur in scattering space, which can be derived using the following identity,

$$\sum_{m=1}^{M} e^{i\vec{q}\cdot\vec{R}_m} = M\sum_{l=1}^{M}\delta(\vec{q}-\vec{H}_l). \tag{1.2}$$

The proof of this identity can be found in Marder's solid state physics book in the appendix [39].

In a real material at non-zero temperature, the positions of the atoms will not rest at the equilibrium positions defined above but will be constantly in motion, storing kinetic energy which can be transported by heat diffusion. The instantaneous deflected atomic position can be written $\vec{r}'_{m,s} = \vec{R}_m + \vec{r}_s + \vec{u}_{m,s}$, where $\vec{R}_m$ is the lattice vector for unit cell m in a crystal with N unit cells and n atoms per unit cell. A small displacement, $\vec{u}_{m,s}$, from the equilibrium position, $\vec{r}_s$, will increase the potential energy of the lattice, which can be written as a function

of all atomic displacements, $U(\vec{u}_{1,1}, \vec{u}_{1,2}, \ldots, \vec{u}_{N,n})$. Since these displacements are small by definition, the potential energy change will correspondingly small and the Taylor expansion of U can be exploited.

$$U = U_0 + \sum \frac{\partial U}{\partial u^{\alpha}_{m,s}} u^{\alpha}_{m,s} + \frac{1}{2} \sum u^{\alpha}_{m,s} \frac{\partial^2 U}{\partial u^{\alpha}_{m,s} \partial u^{\beta}_{m',s'}} u^{\beta}_{m',s'} + \ldots, \tag{1.3}$$

Here α and β index the three Cartesian dimensions. This expansion can be simplified significantly by applying several assumptions. First, the zero order term is unchanging and can be neglected. Second, the first order term must vanish because the energy of the system will be minimized when the atoms are at their rest positions. Finally, by declaring the expansion terms above second order negligible only the second order term remains. This model is called the harmonic approximation, leaving the equation of motion in a very simple matrix form,

$$\mu_s \ddot{\vec{u}}_{m,s} = -\sum_{m',s'} \Phi_{m,s,m',s'} \vec{u}_{m',s'} \tag{1.4}$$

where μ_s is the atomic mass. The so-called Born-von Karman force constants are the quadratic coefficients defined as, $\Phi^{\alpha,\beta}_{m,s,m',s'} = -\dfrac{\partial^2 U}{\partial u^{\alpha}_{m,s} \partial u^{\beta}_{m',s'}}$. The final step to solving the vibrational motion is to expand the displacements into normal modes. The solution for equation 1.4 is assumed to be a plane wave of the form,

$$\vec{u}_{m,s} = \hat{e}_{j,s,\vec{k}} e^{i\vec{k}\cdot\vec{r}_m - i\omega_{j,\vec{k}} t} \tag{1.5}$$

For each vector $\vec{k}$ there will be one mode per Cartesian direction per unit cell atom ($3n$ modes per wave vector) which accounts for all translational degrees of freedom in the lattice. For the j-th mode with wave vector $\vec{k}$, $\hat{e}_{j,s,\vec{k}}$ is the direction

or polarization of the motion of the s-th atom in the unit cell and $\omega_{j,\vec{k}}$ is the angular frequency of the vibration. By substituting the solution 1.5 into equation of motion 1.4, the matrix equation becomes an eigenvalue problem,

$$\mathbf{D}(\vec{k})\hat{\vec{e}}_{j,s,\vec{k}} = \omega^2_{j,\vec{k}}\hat{e}_{j,s,\vec{k}} \tag{1.6}$$

$$\mathbf{D}^{\alpha,\beta}_{s,s'}(\vec{k}) = -\frac{1}{\sqrt{\mu_s\mu_{s'}}}\sum_{m}^{N}\Phi^{\alpha,\beta}_{0s,ms'}e^{-i\vec{k}\cdot\vec{r}'_m} \tag{1.7}$$

The dynamical matrix, $\mathbf{D}(\vec{k})$ is real and symmetric, constructed from the force constants and the atomic masses, μ_s, and is taken to be relative to the 0-th unit cell ($\vec{R}_0 = 0$) [39]. The boundary conditions chosen for this system are periodic. That is to say where a real crystal would have finite size, it is assumed that the lattice (including vibrations) repeats indefinitely in all directions which eliminates the need to worry about edge effects. Importantly for scattering, the phonon frequencies and polarization vectors will also be periodic. Specifically, $\omega_{j,\vec{k}} = \omega_{j,\vec{k}+\vec{H}}$ and $\hat{e}_{j,s,\vec{k}+\vec{H}}$ for all reciprocal lattice vectors which will make the derivation of diffuse scattering in the next chapter much simpler.

The scalar solutions to the eigenvalue equation 1.6 are the mode frequencies $\omega^2_{j,\vec{k}}$ which form j surfaces in momentum space known as the phonon dispersion. Although this derivation has been based on classical mechanics, the vibrational frequencies of a quantum mechanical lattice are the same as its classical counterpart [39]. In this case the energy of the oscillator is quantized to values of the form $\hbar\omega_{j,\vec{k}}(n_{j,\vec{k}} + 1/2)$ where $n_{j,\vec{k}}$ is a positive integer quantum number that counts if a phonon of this mode has been excited. An arbitrary number of phonons may occupy a given state, so an ensemble of phonons in the lattice will obey

Bose statistics. Which means the ensemble average of phonon occupancy can be expressed as a function of the Boltzmann constant, k_B, and lattice temperature, T:

$$\left\langle n_{j,\vec{k}} + \frac{1}{2} \right\rangle = \frac{1}{e^{\hbar\omega_{j,\vec{k}}/k_B T} - 1} + \frac{1}{2} = \coth\left(\frac{\hbar\omega_{j,\vec{k}}}{2k_B T}\right) \tag{1.8}$$

1.3 Calculating the phonon dispersion and polarizations

The phonon dispersion reflects the full harmonic behaviour of the lattice, and can be used to calculate thermal properties of the material (such as the specific heat). Furthermore it plays a fundamental role in diffuse scattering. The matrix equation 1.7 can be solved with elementary numerical (or in simple cases analytic) schemes for solving linear matrix equations as long as accurate values for the Born-von-Karman force constants are known. Finding reliable force constants is not a trivial task since they are functions of all relative atomic positions. Fortunately, the periodicity of the crystal means that the number of atoms for which the forces must be considered is limited to the unit cell, but each of the unit cell atoms feels the effect of every other atom in the crystal. To make this problem tractable the effects from distant atoms must be ignored, applying what is called a nearest-neighbour approximation. Once the number of forces are reduced to a manageable figure, the individual forces are modeled as simple spring forces proportional to atomic displacement weighted by an elastic constant. An analytical example of the derivation of a third nearest neighbour approach for the force constants of graphene is found in Falkovsky *et. al.* [41], in which the accounting of the simple geometry of the graphene lattice, specifically the angles and distances between atoms, is described in detail.

Values for the elastic constants of interatomic forces must come from some form of external knowledge gained either through measurement or first-principles calculation. A calculation of the force constants must be based on the electrostatic potentials of the crystal, and therefore an overview of the system of charges in a crystal is required before delving into advanced computational methods for calculating the force constants and subsequently the phonon dispersion. The following summary is based on chapters 6 and 7 of Marder's book, *Condensed Matter Physics* [39].

In general, the physics of electrostatic charges that make up matter can be described by a very simple Hamiltonian with a Coulomb potential,

$$\mathcal{H} = \sum \frac{\mathcal{P}^2}{2\mu} + \frac{1}{2} \sum \frac{qq'}{|\mathcal{R} - \mathcal{R}'|}, \tag{1.9}$$

where $\mathcal{P}$ and $\mathcal{R}$ are the momentum and position operators and the sums range over all electrons and nuclei in a solid. This expression is not complex on its face, but the sheer number of charges in a macroscopic material (10^{23}) make working with equation 1.9 impossible without a series of approximations. The simplest useful model is that of a free Fermi gas, which assumes that the electrons have no interaction with the nuclei nor each other, subject only to the Pauli exclusion principle. Despite the severity of this assumption, this model explains some properties of simple materials, such as alkali metals, quite well, but it is still limited in its applications. The next level of complexity combines all the nuclei and the core electrons into a single entity (the ionic crystal) that acts upon the conduction electrons as an external electrostatic field. This is known as

the Born-Oppenheimer approximation which effectively separates the ionic and electronic wave functions by making them independent. Once the ionic potential is established it can be applied while ignoring conduction electrons entirely, which is what was done in the previous section to describe phonons, or the influence of the ionic potential on the conduction electrons can be considered. This is the basis of the single-electron model. As the name implies, the inter-electron interactions are still ignored (except again for the Pauli principle) but this model serves as a foundation for the applications relevant to this work.

The single-electron Hamiltonian for a crystalline solid is,

$$\mathcal{H}_e = \frac{\mathcal{P}^2}{2\mu_e} + \varphi_{ext}, \tag{1.10}$$

where φ_{ext} is an external periodic electrostatic potential dependent on the equilibrium ionic positions. The consequences of the periodicity are that the Hamiltonian shares its eigenfunctions with the translation operator and these eigenfunctions are associated with a single value for momentum $\hbar\vec{k}$, where $\vec{k}$ is called the Bloch wave vector. For a given $\vec{k}$ there can be many energy eigenvalues, $\epsilon_{n,\vec{k}}$, which are labelled by the band index, n. The dispersion of these band energies as functions of momentum, also known as the electronic band structure, are extremely fundamental for the understanding of the electronic properties of materials. They contain information on whether a solid is a metal, insulator or semiconductor. The curvature of the bands represent electron velocities and can predict electrical transport properties. The shapes of bands can also be used to calculate minimum energy crystal structures and magnetic properties. In a macroscopic material, the

occupation probability of an electron in state n is given by the Fermi function $f_{n,\vec{k}} = \dfrac{1}{e^{\epsilon_{n,\vec{k}}/k_B T} + 1}$. Due to the Pauli exclusion principle, only two electrons are allowed at any point of the band structure, one per spin direction. Therefore, at the ground state energy of the N particle macroscopic system, the particles fill up all energy levels below a particular energy ϵ_F, called the Fermi energy, below which there are exactly N states. The Fermi surface is the energy surface in momentum space which separates occupied from unoccupied electron states in the zero temperature limit.

But how can the single-electron model be used to calculate the inter-atomic forces needed to solve the phonon problem? The Born-Oppenheimer approximation establishes that the single electron Hamiltonian only determines the physics of the conduction electrons and can be considered independent of the lattice dynamics. To determine the physics of the ions, the Hamiltonian for the ionic lattice is needed:

$$\mathcal{H}_i = -\sum_{m,s} \frac{\hbar^2}{2\mu_{m,s}} \frac{\partial^2}{\partial u_{m,s}^2} + U(\vec{u}_{1,1}, \vec{u}_{1,2}, \ldots, \vec{u}_{N,n}), \tag{1.11}$$

where m and s index the unit cell number and the atoms in the unit cell, and U is the energy of the lattice as a function of ionic position used for the phonon treatment in the previous section. U can be understood as the ground state energy of a system of interacting electrons moving in the field of fixed nuclei, called the Born-Oppenheimer energy surface [42]. The Hamiltonian that gives rise to this

ground state energy is,

$$\mathcal{H}_{BO} = -\sum_i \frac{\hbar^2}{2\mu_e}\frac{\partial^2}{\partial r_i^2} + \sum_{i\neq j} E_{ee}(\vec{r}_i, \vec{r}_j) + \sum_{i,m,s} E_{ne}(\vec{r}_i, \vec{u}_{m.s}) + \sum_{\substack{m,s \\ m',s'}} E_{nn}(\vec{u}_{m,s}, \vec{u}_{m',s'}). \tag{1.12}$$

Here $\vec{r}_i$ is the electron position and $\vec{u}_{m,s}$ is the atomic displacement from equilibrium. The three electrostatic interactions are the electron-electron (E_{ee}), electron-nucleus (E_{ne}), and nucleus-nucleus (E_{nn}) Coulombic potentials, each in the familiar form. Note that the inclusion of inter-electron forces in this step appears to be a departure from the single-electron model. But since the goal of this derivation is to find the matrix of second derivatives, or Hessian matrix, of the ground state energy U (*i.e.* the Born-von-Karman force constants), the Schrödinger equation will not need be solved for this Hamiltonian. In short, the inclusion of electron-electron interactions here is a technicality and does not invalidate previous assumptions made to avoid a many-body problem.

The mathematical tool needed to find the force constants from $\mathcal{H}_{BO}$ is the Hellman-Feynman theorem [42]. Which is applied to the ground state energy giving,

$$\frac{\partial U}{\partial u_{m,s}} = -\left\langle \Psi \left| \frac{\partial H_{BO}}{\partial u_{m,s}} \right| \Psi \right\rangle, \tag{1.13}$$

where Ψ is the ground state wavefunction of the Born-Oppenheimer Hamiltonian. To get from here to the Hessian matrix elements (force constatnts), simply apply a second partial derivative. The algebra for this can be found in Baroni *et.al.* [42] resulting in the following expression,

$$\Phi^{\alpha,\beta}_{m,s,m',s'} = \frac{\partial^2 U}{\partial u_{m,s}\partial u_{m',s'}}$$
$$= \int \frac{\partial \rho_e(\vec{r})}{\partial u_{m,s}} \frac{\partial E_{ne}}{\partial u_{m,s}} + \rho_e(\vec{r}) \frac{\partial^2 E_{ne}}{\partial u_{m,s}\partial u_{m',s'}} d\vec{r} + \frac{\partial^2 E_{nn}}{\partial u_{m,s}\partial u_{m',s'}}. \quad (1.14)$$

Here, $\rho_e(\vec{r})$ is the ground state electron charge density. Therefore, the interatomic force constants and the dynamical matrix require only a calculation of $\rho_e(\vec{r})$ and its linear response to atomic displacements $\frac{\partial \rho_e(\vec{r})}{\partial u_{m,s}}$. This leads the discussion towards a computational technique that is built on the characteristics of the charge density known as *density functional theory*.

1.4 Density functional theory

A theorem derived by Hohenberg and Kohn reveals the remarkable property of the electronic charge distribution, $\rho_e(\vec{r})$, which is the basis of density functional theory. It states that no two potentials acting on a system of electrons have the same ground state charge distribution [43]. That is to say that there is a one-one map or bijection between the set of all potentials and the set of all ground state electronic charge densities. This idea can be refined using tools of variational calculus. By applying the Rayleigh-Ritz variational principle of quantum mechanics, it can be proved that there exists a *universal functional*, $F[\rho_e]$ such that the energy functional [42],

$$E[\rho_e] = F[\rho_e] + \int \rho_e(\vec{r})\varphi(\vec{r})d\vec{r}, \quad (1.15)$$

is minimized by the ground state electron charge density corresponding to the external potential $\varphi(\vec{r})$. Although this is an enticing result, the application of

equation 1.15 is not obvious. It was shown by Kohn and Sham [44] that by choosing the appropriate form for the universal functional, F_{KS}, the many-body Hamiltonian that includes electron-electron interactions can be reduced to an equivalent problem analogous to the single-electron Hamiltonian. This is an extremely powerful feature since it allows for electron-electron coupling to be accounted for while using the familiar mathematics of single-electron model. The potential that is found by minimizing the functional $E[\rho_e]$ while using F_{KS} in equation 1.15, is called the *self-consistent field potential*, which has the form,

$$\varphi_{SCF}(\vec{r}) = \varphi_{ext}(\vec{r}) + e^2 \int \frac{\rho_e(\vec{r}\,')}{|\vec{r} - \vec{r}\,'|} d\vec{r}\,' + v_{xc}. \tag{1.16}$$

Here, φ_{ext} is the familiar ionic electrostatic potential and the last term, v_{xc}, is called the *exchange correlation potential* which represents the effect of many body interactions. The general form of the exchange correlation potential is not known. Several approximations exist which which can be applied to accurately calculate certain physical properties, such as the most commonly used local density approximation or the generalized-gradient approximation. A discussion on the various applications and nuances regarding the form of the exchange correlation potential is tangential to this work and can be found elsewhere [37].

If the self-consistent field potential is used in the single-electron Schrödinger's equation (1.10), the wave function solutions are known as the Kohn-Sham orbitals, ϕ_n, which are related to the electronic charge density by,

$$\rho_e(\vec{r}) = 2 \sum |\phi_n(\vec{r})|^2 \tag{1.17}$$

These two equations, 1.16 and 1.17, represent a mutual dependence between the electronic charge density and the self consistent field (via the Kohn-Sham orbitals). An iterative algorithm that repeatedly solves equations 1.16 and 1.17 can be used to converge on numerical values for φ_{SCF} and ρ_e. The calculations performed at each iteration of this algorithm are analogous to solving the eigenvalue problem for a single-electron Hamiltonian. Standard techniques for accomplishing this often use so-called *pseudopotentials* to approximate the external field because their solutions are in the form of plane waves. An overview of plane waves and pseudopotentials can be found in reference [39].

The algorithmic technique for finding ρ_e has been presented, but in order to calculate the force constants using equation 1.14, its linear response to ionic displacements, $\dfrac{\partial \rho_e}{\partial \vec{u}_{m,s}}$, is also needed. For this, a perturbative approach can be used on the Kohn-Sham Hamiltonian discussed above. The methods of density functional perturbation theory use a similar iterative algorithm to the one discussed above but is too complex and nuanced to be shown here. The details of the formulation be found in reference [42].

The application of these results to the calculation of phonon dispersions and polarizations is applied by two packages of the open source software suite Quantum Espresso, PWscf and PHonon [45, 46]. For a given material, the program input includes the chemical and geometric unit cell structure, pseudopotentials corresponding to the constituent atoms and a compatible exchange correlation potential. The PWscf program calculates the self consistent potential and the Kohn-Sham orbitals, effectively solving for ρ_e. The PHonon program

applies density functional perturbation theory to the output of the PWscf program and calculates both the linear response $\frac{\partial \rho_e}{\partial \vec{u}_{m,s}}$ and the Born-von Karman force constants. It also solves the dynamical matrix equation including both phonon dispersion and polarization vectors at any inputted wavevector. These programs were used to solve the phonon systems for graphite and $TiSe_2$, and the atomic positions, pseudopotentials, exchange correlation functionals and other input used for each case will be given in Chapters 4 and 5, respectively.

1.5 Electron-phonon and phonon-phonon coupling

Moving beyond the single-electron and harmonic approximations in order to understand the effects of interactions is a complex topic with several possible approaches. For the purposes of understanding UEDS results in the context of relevant literature, only simple perturbative methods will be presented here. In particular the screening of atomic vibrations by electrons, known as Kohn anomalies are relevant to both graphite and $TiSe_2$ systems [15, 47].

Electron-phonon interactions can be succinctly described using the language of second quantization. Let $a^{\dagger}_{n,\vec{q}}$ and $a_{n,\vec{q}}$ be the creation and annihilation operators for electrons with momentum $\vec{q}$ in the n-th energy band and $b^{\dagger}_{j,\vec{q}}$ and $b_{j,\vec{q}}$ be the equivalent operators for phonons. The Hamiltonian that includes electron-phonon interactions is called the Fröhlich Hamiltonian, which includes the term [48],

$$H_{e-ph} = \sum_{n,j,\vec{q},\vec{k}} g_{n,n',j,\vec{k},\vec{q}}\, a^{\dagger}_{n',\vec{k}+\vec{q}} a_{n,\vec{k}} (b^{\dagger}_{j,-\vec{q}} + b_{j,\vec{q}}) \tag{1.18}$$

Here $g_{n,n',j,\vec{k},\vec{q}}$ is the electron-phonon coupling constant which is proportional to the probability density of an electron in the n-th band with momentum $\vec{k}$ either

creating a phonon with momentum -$\vec{q}$ or absorbing a phonon with momentum $\vec{q}$ to create an electron in the n'-th band with momentum $\vec{k}+\vec{q}$.

It can be shown that in a mean field approximation where g is constant that the effect of the electron-phonon interaction on a phonon mode's frequency is proportional to the linear response of an electron gas to a time independent external field,

$$\rho^{\text{ind}}(\vec{q}) = \chi(\vec{q})\phi^{\text{ext}}, (\vec{q}) \tag{1.19}$$

where $\chi(\vec{q})$ is the so-called Lindhard response function, which for d dimensions is given by [48],

$$\chi(\vec{q},T) = \int \frac{d\vec{k}}{(2\pi)^d} \frac{f_{\vec{k}}(T) - f_{\vec{k}+\vec{q}}(T)}{\epsilon_{\vec{k}} - \epsilon_{\vec{k}+\vec{q}}}. \tag{1.20}$$

Here $f_{\vec{k}}$ is the Fermi function as defined in the previous section. From the form of equation 1.20 it is clear that $\chi(\vec{q},T)$ will diverge at momenta that join two degenerate points on the energy surface where the expected occupancy of the connected states are not be the same, *i.e.* at or near the Fermi surface. These vectors are called nesting vectors of the Fermi surface.

The renormalized phonon frequency with momentum $\vec{q}$ is reduced by [48],

$$\Delta\omega^2_{j,\vec{q}} = \frac{2g^2\omega_{j,\vec{q}}}{\hbar}\chi(\vec{q},T). \tag{1.21}$$

$\Delta\omega^2_{j,\vec{q}}$ is proportional to $\chi(\vec{q},T)$ and will therefore diverge at the nesting vectors of the Fermi surface. This effect on the phonon dispersion is called a Kohn anomaly.

It is considered anomalous because it is not predicted by the previously discussed methods for calculating phonon dispersions [49]. Advanced density functional perturbation theory methods can by applied to calculate the electron-phonon coupling constant and Lindhard response function from a perturbative potential and electron density [47].

The temperature dependence of $\chi(\vec{q}, T)$ causes the decrease in phonon frequency to be more extreme at low temperatures. Moreover the effect is stronger still in 2D or 1D materials [48]. If the electron-phonon coupling is strong enough the phonon frequency can be reduced all the way to zero, defining a phase transition called a charge density wave transition. In this new phase the phonon is 'frozen in', casing a periodic lattice distortion that is accompanied by a periodic charge density modulation, as the name suggests. Charge density wave transitions are a popular subject of study in condensed matter physics and will be the focus of Chapter 5 of this thesis.

Anharmonic phonon behaviour can be expressed in terms of scattering coefficients which are related to the probability of a corresponding phonon scattering event. The lowest order three-phonon scattering coefficients are given by a third degree partial derivative of the same ionic crystal potential U used for the harmonic approximation [25],

$$V^{(3)}_{j_1,\vec{k}_1,j_2,\vec{k}_2,j_3,\vec{k}_3} = \frac{1}{M} \frac{\partial^3 U}{\partial X_{j_1,\vec{k}_1} \partial X_{j_2,\vec{k}_2} \partial X_{j_3,\vec{k}_3}} \tag{1.22}$$

where $X_{j,\vec{k}}$ is an unitless variable related to, $u_{j,s,\vec{k}}$, the Fourier component of the atomic displacement via,

$$\frac{\partial}{\partial X_{j,\vec{k}}} = \sum_{s,\alpha} \sqrt{\frac{\hbar}{2\mu_s \omega j,\vec{k}}} \hat{e}^{\alpha}_{j,s,\vec{k}} \frac{\partial}{\partial u^{\alpha}_{j,s,\vec{k}}}. \tag{1.23}$$

Due to translational symmetry of the crystal, a momentum conservation law constrains $V^{(3)}_{j_1,\vec{k}_1,j_2,\vec{k}_2,j_3,\vec{k}_3} \neq 0$ only when the sum of the scattering vectors sum to a reciprocal lattice vector, $\vec{k}_1 + \vec{k}_2 + \vec{k}_3 = \vec{H}$. Energy conservation of the scattering process also guarantee that either $\omega_{k_1} - \omega_{k_1} - \omega_{k_1} = 0$ or $\omega_{k_1} + \omega_{k_1} - \omega_{k_1} = 0$ for a decay of one into two or two into one phonons respectively. The phonon lifetime due to the anharmonic phonon-phonon decay is inversely proportional to $V^{(3)}_{j_1,\vec{k}_1,j_2,\vec{k}_2,j_3,\vec{k}_3}$ and the occupancy of the initial phonon(s) [25]. The inverse of the phonon lifetime is in units of frequency and is called anharmonic broadening, therefore the decay rates of phonons can be visualized by a broadening of the phonon dispersion curve. Knowing the anharmonic scattering coefficients can determine the lattice thermal conductivity within the framework of the Boltzman transport equation [25]. So the ability to measure phonon decay via UEDS analysis, where previously these properties were only accessible via numerical computation, is invaluable to the understanding of thermal transport in crystalline materials and thermoelectric phenomena.

CHAPTER 2
Scattering theory

Armed with a methodology for computing phonon dispersions and polarizations, the effect of atomic vibrations on the scattering of radiation will be derived in this chapter. First, a theory for electron scattering will be constructed from first principles. The initial arguments will be based on those given in J.M. Cowley's book [50], and the expansion to elastic and diffuse scattering will be based on the work done by Xu. *et. al.* [51]. The relationships between scattering and macroscopic vibrational states of a sample will dictate the analysis needed to tease apart the diffuse scattering contributions from each phonon mode.

2.1 Scattered waves

Different sources of radiation, such as x-rays, electrons and neutrons, each have distinctive properties and behaviours, including their generation, detection and collisions with other particles. However, the manner in which they propagate and scatter can all be described by the same type of differential equation, the wave equation. For a charged particle wave function this is the Schrödinger equation,

$$\frac{\hbar^2}{2m}\nabla^2\Psi + e\varphi(\vec{r})\Psi = -i\hbar\frac{\partial\Psi}{\partial t}, \tag{2.1}$$

where Ψ is defined as the wave function such that $|\Psi|^2$ is the probability of an electron being present in unit volume and φ is the electrostatic potential. To

solve Equation 2.1, the form of the wave function is assumed to be $\Psi = \psi e^{i\omega t}$, describing a wave of a single frequency ω which is a assumed to be oscillating very quickly relative to the time dependence of φ. Equation 2.1 can then be simplified by applying $\frac{\partial \Psi}{\partial t} = -\omega^2 \Psi$, thus eliminating the explicit time dependence in the equation. A similar argument follows from Maxwell's equation for electromagnetic waves so the time independent wave equation is written in a general form that can be applied to any type of radiation:

$$\left[\nabla^2 + k_0^2 + \mu\varphi(\vec{r})\right] \Psi(r) = 0. \tag{2.2}$$

Here, the wave vector, k, and interaction strength μ depend on the type of scattering wave and scattered volume. In the crystallographic literature, the wavenumber, $2\pi k_0$, is often used in these equations, but here the solid-state physics convention will be used. Equation 2.2 is a linear differential equation with an impulse response or Green's function, $G(\vec{r}, \vec{r}\,')$. So, it can be written in the integral form,

$$\Psi(\vec{r}) = \Psi_0(\vec{r}) + \mu \int G(\vec{r}, \vec{r}\,')\varphi(\vec{r}\,')\Psi(\vec{r}\,')\mathrm{d}\vec{r}\,' \tag{2.3}$$

$$G(\vec{r}, \vec{r}\,') = \frac{e^{ik|\vec{r}-\vec{r}\,'|}}{4\pi|\vec{r}-\vec{r}\,'|} \tag{2.4}$$

Here, $\Psi_0(\vec{r})$ is the wave incident on the scattering field and the integral describes the scattered radiation, $\Psi_s(\vec{r})$. The geometry of this equation is shown in Figure 2–1.

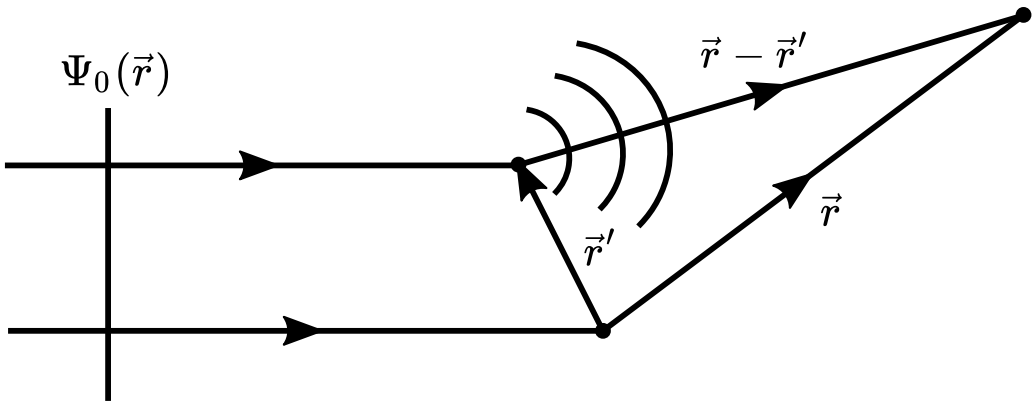

Figure 2–1: Scattering geometry diagram for an incident plane wave Ψ_0, showing the definitions for the distances $\vec{r}$ and $\vec{r}'$.

The equation for $G(\vec{r}, \vec{r}')$ represents the intensity of a spherical wave emitted from the point $\vec{r}'$ and measured at $\vec{r}$. Therefore the scattered wave consists of a sum of spherical waves, corresponding with the well known Hyugen's principle.

2.2 The first Born approximation

The integral equation 2.3 is very difficult to solve because the full scattered wave, $\Psi(\vec{r})$, appears on both sides of the equation. However, if the amplitude of the scattered wave is small compared to that of the incident wave, one may approximate $\Psi(\vec{r})$ to be equal to $\Psi_0(\vec{r})$ in the integral. This is known as the first Born approximation. For a planar incident wave $\Psi_0 = e^{-i\vec{k_0}\cdot\vec{r}}$, Equation 2.3 becomes,

$$\begin{aligned}\Psi(\vec{r}) &= \Psi_0(\vec{r}) + \Psi_s(\vec{r}) \\ &= e^{-i\vec{k_0}\cdot\vec{r}} + \frac{\mu}{4\pi}\int \frac{e^{ik|\vec{r}-\vec{r}'|}}{|\vec{r}-\vec{r}'|}\varphi(\vec{r}')e^{-i\vec{k_0}\cdot\vec{r}'}\mathrm{d}\vec{r}'. \end{aligned} \tag{2.5}$$

Next, a more straightforward approximation can be applied the generalized scattered wave, Ψ_s, assuming the point of observation, $r = R$ is much larger than the dimensions of the scattering field, *i.e.* $r' \ll R$. Then the scattered wave is given by,

$$\Psi_s(\vec{q}) = \frac{e^{-ik_0 R}}{R} f(\vec{q}) \tag{2.6}$$

where $\vec{q} = \vec{k} - \vec{k}_0$ is the scattering vector and $f(\vec{q})$ is known as the scattering amplitude,

$$f(\vec{q}) = \frac{\mu}{4\pi} \int \varphi(\vec{r}) e^{-i\vec{q}\cdot\vec{r}} \mathrm{d}\vec{r} \tag{2.7}$$

The scattering amplitude is defined by the nature of a scattered wave and its scattering potential. In other words, waves will scatter differently depending on the type of wave and the type of scatterer. For example, electrons will scatter off of electrostatic potential via the Lorentz force and x-rays will scatter by being re-emitted after accelerating a charged particle (Thomson scattering) [52]. Conveniently, Equation 2.7 demonstrates that $f(\vec{q})$ is simply the Fourier transform of the associated scattering potential, $\varphi(\vec{r})$, which allows for straightforward computation in many cases.

2.3 Electron scattering

The scattering potential of atoms, used in Schrödinger's equation (Equation 2.2) for electron scattering, is the electric potential of both the atomic nucleus and electron orbitals which are related to charge density by Poisson's equation of

electrostatics,

$$\nabla^2\varphi(\vec{r}) = \frac{|e|}{\epsilon_0}[\rho_n(\vec{r}) - \rho_e(\vec{r})]. \tag{2.8}$$

Here, ρ_n and ρ_e are the charge densities of the nucleus and electrons respectively. So the atomic scattering amplitude for electrons, $f_e(\vec{q})$ is simply the Fourier transform of the atomic potential. The interaction strength for electrons used in Equation 2.7 is $\mu = \frac{2m_e e}{h^2}$. The scattering amplitude is often assumed to be isotropic $f_e(\vec{q}) = f_e(q)$ and has been calculated and tabulated for most elements in the International Tables for Crystallography vol. C [53]. The units of $f_e(\vec{q})$ as it appears in Equation 2.7 are in volts times cubed angstroms(VÅ^3), however the values presented in tables are often in angstroms (Å). This discrepancy is due to a 'historical accident' in the early derivations of the Born approximation. The conversion factor to go from the tabled scattering amplitudes in angstroms to the ones used here, is $\sigma/\lambda = 2\pi m_0 e\gamma/h^2$ which may include a relativistic correction term $\gamma = \sqrt{1 + h^2/m_0^2c^2\lambda^2}$. Alternatively, one can use the Mott formula which relates the electron and x-ray scattering amplitudes,

$$f_e(q) = \frac{|e|(Z - f_x(q))}{4\pi^2\epsilon_0 q^2}. \tag{2.9}$$

Here, Z is the atomic number and $f_x(q)$ is the x-ray scattering amplitude. X-rays scatter off of the electron charge density only so $f_x(q)$ is easier to calculate than $f_e(q)$. Also, due to the popularity of x-ray scattering in many fields, tables of $f_x(q)$ are more detailed and more easily available. So it is often better to use the equation 2.9 instead of looking up $f_e(q)$ directly.

Typical electron scattering energies range from 100-400 keV [50]. A convenient formula for the wavelength of a relativistic electron beam relative as a function of accelerating voltage, E_0 (in volts) is given here:

$$\lambda = \left[\frac{12.2643}{\sqrt{E_0 + (0.97845 \times 10^{-6}) E_0^2}} \right] \text{ Å}. \tag{2.10}$$

2.4 Scattering from a crystal

The previous section describes the scattering of a single electron from a solitary atom. In order to extend this to an electron beam scattering from a crystal, a few assumptions must be made. First, the electron beam is assumed to be monochromatic, and thus described by a single value for k_0. Second, the electrons that comprise the beam do not interact, *i.e.* the scattered wave functions of all N electrons in the beam are identical can simply be added together, $\Psi_N(\vec{q}) = N\Psi(\vec{q})$.

The scattering amplitude of the crystal is simply the sum of the potentials of every atom in the lattice. In order to take into account lattice vibrations, the position of each atom is written to include atomic displacements, $\vec{r}_{\text{atom}} = \vec{R}_m + \vec{r}_s + \vec{u}_{m,s}$ where R_m is a lattice vector, r_s is the equilibrium position of the atom in the unit cell and $\vec{u}_{m,s}$ is the displacement as defined in Section 1.2. Here, s indexes the n atoms in the unit cell and m indexes the number of unit cells in the crystal, M. Then the observed scattered intensity $I(\vec{q}) = N \langle |\Psi_s(\vec{q})|^2 \rangle$ at scattering vector $\vec{q}$, is given by a time-averaged probability density [51],

$$I(\vec{q}) = N \left\langle \left| \sum_{m,s} f_s(q) e^{i\vec{q}\cdot(\vec{R}_m + \vec{r}_s + \vec{u}_{m,s})} \right|^2 \right\rangle$$
$$= N \sum_{m,m',s,s'} f_s(q) f_{s'}(q) e^{i\vec{q}\cdot(\vec{R}_{m,m'} + \vec{r}_{s,s'})} \left\langle e^{i\vec{q}\cdot(\vec{u}_{m,s} - \vec{u}_{m',s'})} \right\rangle \tag{2.11}$$

Here, $\vec{R}_{m,m'} = \vec{R}_m - \vec{R}_{m'}$ and $\vec{r}_{s,s'} = \vec{r}_s - \vec{r}_{s'}$, for short. To further simplify equation 2.11, the identity $\langle e^{ix} \rangle = e^{-\langle x^2 \rangle / 2}$ is used. This identity holds if x is small and has equal probability of being positive or negative, which is true for the atomic displacement, $\vec{u}_{m,s}$. The proof of this step can be found in Warren's book [19]. Continuing on, equation 2.11 becomes,

$$I(\vec{q}) = N \sum_{m,m',s,s'} f_s(q) f_{s'}(q) e^{i\vec{q}\cdot(\vec{R}_{m,m'} + \vec{r}_{s,s'})} e^{-\frac{1}{2}\left\langle [\vec{q}\cdot(\vec{u}_{m,s} - \vec{u}_{m',s'})]^2 \right\rangle} \tag{2.12}$$

In order to evaluate the exponent, $\frac{1}{2}\left\langle [\vec{q}\cdot(\vec{u}_{m,s} - \vec{u}_{m',s'})]^2 \right\rangle$, we write the atomic displacements as a superposition of all lattice vibration modes.

$$\vec{u}_{m,s} = \mathrm{Re}\left\{ \frac{1}{\mu_s} \sum_{\vec{k},j} a_{j,\vec{k}} \hat{e}_{j,s,\vec{k}} e^{i\vec{k}\cdot\vec{R}_m - i\omega_{j,\vec{k}} t + i\phi_{j,\vec{k}}} \right\} \tag{2.13}$$

Where $a_{j,\vec{k}}$ is the mode amplitude coefficient, $\omega_{j,\vec{k}}$ and $\hat{e}_{j,s,\vec{k}}$ are the mode frequency and polarization for unit cell atom s as defined in equation 1.5, μ_s is the mass of atom s and $\phi_{j,\vec{k}}$ is a phase offset. When evaluating the square in equation 2.12, the time averaged cross terms will cancel out leaving,

$$\frac{1}{2}\left\langle[\vec{q}\cdot(\vec{u}_{m,s}-\vec{u}_{m',s'})]^2\right\rangle$$
$$= M_s + M_{s'} - \sum_{j,\vec{k}} \frac{|a_{j,\vec{k}}|^2}{2\sqrt{\mu_s\mu_{s'}}}(\vec{q}\cdot\hat{e}_{j,s,\vec{k}})(\vec{q}\cdot\hat{e}_{j,s',\vec{k}})e^{i\vec{k}\cdot\vec{R}_{m,m'}}, \tag{2.14}$$

where the Debye-Waller factor is defined as,

$$M_s = \frac{1}{4\mu_s}\sum_{j,\vec{k}}|a_{j,\vec{k}}|^2|\vec{q}\cdot\hat{e}_{j,s,\vec{k}}|^2. \tag{2.15}$$

The square amplitudes, $|a_{j,\vec{k}}|^2$, are related to the ensemble averaged quantum number for phonon occupancy, $n_{j,\vec{k}}$. To derive this relation, consider the mean kinetic energy of the system,

$$\begin{aligned}\langle KE\rangle &= \frac{1}{2}\sum_{m,s}\mu_s\left\langle\dot{\vec{u}}_{m,s}^2\right\rangle \\ &= \frac{M}{4}\sum_{j,\vec{k}}|a_{j,\vec{k}}|^2\omega_{j,\vec{k}}^2\end{aligned} \tag{2.16}$$

Equation 2.16 will correspond with the kinetic energy of a quantum harmonic oscillator,

$$\langle KE\rangle = \frac{1}{2}\sum_{j,\vec{k}}\hbar\omega_{j,\vec{k}}\left(n_{j,\vec{k}}+\frac{1}{2}\right), \tag{2.17}$$

By combining equations 2.16 and 2.17 the squared amplitudes can be written as a function of phonon occupancy and frequency,

$$|a_{j,\vec{k}}|^2 = \frac{\hbar}{M\omega_{j,\vec{k}}}\left(n_{j,\vec{k}} + \frac{1}{2}\right) \tag{2.18}$$

Finally, the equation for total scattered intensity (2.12) can be further simplified using 2.13 and 2.18. From here the notation will be changed for ease and clarity. First, R_m can be set to zero thanks to translational symmetry and the index m' will be renamed to m. The full scattered intensity can now be written as a function of the individual phonon occupancies,

$$I(\vec{q}) = I_e \sum_{m,s,s'} f_s(q) f_{s'}(q) e^{-M_s - M_{s'}} e^{-i\vec{q}\cdot(\vec{R}_m + \vec{r}_{s,s'})} e^{F_{m,s,s'}(\vec{q})}, \tag{2.19}$$

where $I_e = MN$ and $F_{m,s,s'}(\vec{q})$ is shorthand for the function,

$$F_{m,s,s'}(\vec{q}) = \frac{\hbar}{2M\sqrt{\mu_s \mu'_s}} \sum_{j,\vec{k}} \frac{n_{j,\vec{k}} + \frac{1}{2}}{\omega_{j,\vec{k}}} (\vec{q}\cdot\hat{e}_{j,s,\vec{k}})(\vec{q}\cdot\hat{e}_{j,s',\vec{k}}) e^{i\vec{k}\cdot\vec{R}_m} \tag{2.20}$$

This equation is possible to calculate numerically, although it is computationally costly. To further simplify the calculation, equation 2.19 can be expanded around $F_{m,s,s'}(\vec{q})$ via the Taylor series of $e^{F_{m,s,s'}(\vec{q})}$,

$$I(\vec{q}) = I_0(\vec{q}) + I_1(\vec{q}) + I_2(\vec{q}) + \dots$$

$$I_0(\vec{q}) = MI_e \sum_{m,s,s'} f_s(q) f_{s'}(q) e^{-M_s - M_{s'}} e^{-i\vec{q}\cdot(\vec{R}_m + \vec{r}_{s,s'})} \tag{2.21}$$

$$I_1(\vec{q}) = MI_e \sum_{m,s,s'} f_s(q) f_{s'}(q) e^{-M_s - M_{s'}} e^{-i\vec{q}\cdot(\vec{R}_m + \vec{r}_{s,s'})} F_{m,s,s'}(\vec{q}) \tag{2.22}$$

$$I_2(\vec{q}) = MI_e \sum_{m,s,s'} f_s(q) f_{s'}(q) e^{-M_s - M_{s'}} e^{-i\vec{q}\cdot(\vec{R}_m + \vec{r}_{s,s'})} F_{m,s,s'}(\vec{q})^2/2 \tag{2.23}$$

This expansion divides the scattering contributions into elastic or Bragg scattering ($I_0(\vec{q})$) and diffuse scattering ($I_1(\vec{q}) + I_2(\vec{q}) + \ldots$).

2.5 Structure factors

The elastic scattering term $I_0(\vec{q})$ contains only one factor that depends on the unit cell index, so it can be evaluated independently using equation 1.2, $\sum_{m=1}^{M} e^{-i\vec{q}\cdot\vec{R}_m} = M \sum_{l=1}^{M} \delta(\vec{q} + \vec{H}_l)$. This factor represents the effect of the crystal periodicity on the scattering geometry, which localizes the elastic scattering at the reciprocal lattice points, $\vec{H}_l$, satisfying what is known as the Laue condition. In order to evaluate this sum, consider the set of all scattering vectors $\vec{q} = \vec{k} - \vec{k}_0$, which represent the direction of the scattered beam in reciprocal space. By applying equation 1.2, reindexing the sum over l such that $-\vec{H}_l = \vec{H}_{l'}$ and regrouping the double sum over s and s' into the square, Equation 2.21 can be written in its final form,

$$I_0(\vec{q}) = M I_e |F_0(\vec{q})|^2 \left[\sum_{l'} \delta(\vec{q} - \vec{H}_{l'}) \right] \tag{2.24}$$

In practice the Bragg peaks that are visible in a diffraction pattern will be only those that intersect with the so called Ewald sphere, which is a visualization of the Laue condition shown in figure 2–2. The intensity of each peak is weighted by the *geometric structure factor*,

$$F_0(\vec{q}) = \sum_{s} e^{-M_s} f_s e^{-i\vec{q}\cdot\vec{r}_s} \tag{2.25}$$

which, contains three dynamic multiplicative terms: the Debye-Waller factor, e^{-M_s}, the atomic form factor, f_s and a geometric phase factor, $e^{-i\vec{q}\cdot\vec{r}_s}$. As stated previously, f_s is calculated from the scattering potential of a single atom (the atomic electrostatic potential for electrons or electron density for x-rays) where $e^{-i\vec{q}\cdot\vec{r}_s}$ depends only on the atomic arrangement of the unit cell. For electron diffraction, the two latter terms, along with the Bragg peak positions, encode the full atomic and electronic structure of the lattice. However, the lattice configuration may not be easily solved because the complex phase of F_0 is lost by the modulus in Eq. 2.24. This is the so called 'phase problem' of crystallography. This problem may be overcome by one of many modern methodologies depending on the nature of the diffraction experiment and the sample [54]. Measuring $I_0(\vec{q})$ can also reveal thermal behaviour of the lattice. The Debye-Waller factor, M_s, is proportional to the mean square amplitude of atomic displacements and thus measurements of peak intensity dynamics reveal changes in overall lattice excitation [13]. Notably, measurements of $I_0(\vec{q})$ are only indirect measures of phonon behaviour, and cannot be used to track phonon dynamics with energy, momentum and time resolution. However, if a diffractometer has sufficient signal-to-noise to resolve optically induced changes to the diffuse scattering between Bragg peaks, $I_1(\vec{q})$, such measurements are possible.

The full expression of the diffuse intensity $I_1(\vec{q})$ is given by,

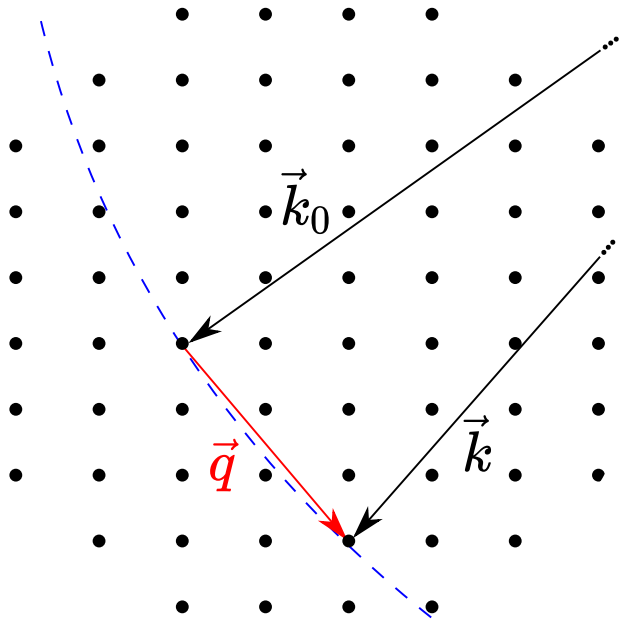

Figure 2–2: Visualization of the Laue condition for elastic scattering. If the Ewald sphere, shown as the blue circle, intersects with a reciprocal lattice point (black dots), a Bragg peak may appear at the scattering vector, $\vec{k} - \vec{k}_0 = \vec{q} = \vec{H}$, as long as the geometric structure factor, $F_0(\vec{q})$, is not zero. The Ewald sphere is much flatter (low curvature) for short wavelength electrons compared to x-rays. Therefore more Bragg peaks corresponding to a single plane of reciprocal lattice vectors will be visible in a single diffraction pattern.

$$I_1(\vec{q}) = \frac{\hbar I_e}{2} \sum_{m,s,s'} \sum_{j,\vec{k}} \frac{f_s(q) f_{s'}(q)}{\sqrt{\mu_s \mu_s'}} e^{-M_s - M_{s'}} \frac{n_{j,\vec{k}} + \frac{1}{2}}{\omega_{j,\vec{k}}} (\vec{q} \cdot \hat{e}_{j,s,\vec{k}})(\vec{q} \cdot \hat{e}_{j,s',\vec{k}}) e^{-i\vec{q} \cdot \vec{r}_{s,s'}} e^{-i(\vec{q} - \vec{k}) \cdot \vec{R}_m}. \tag{2.26}$$

Again, by using identity 1.2, $\sum_{m=1}^{M} e^{-i(\vec{q} - \vec{k}) \cdot \vec{R}_m} = M \sum_{l=1}^{M} \delta(\vec{k} - (\vec{q} + \vec{H}_l))$, then reindexing the sum over l such that $-\vec{H}_l = \vec{H}_{l'}$ and regrouping the double sum over s and s' into the square,

$$I_1(\vec{q}) = I_e \sum_{j,l'} \frac{(n_{j,\vec{q}-\vec{H}_{l'}} + \frac{1}{2})}{\omega_{j,\vec{q}-\vec{H}_{l'}}} \left| \sum_s e^{-M_s} \frac{f_s(q)}{\sqrt{\mu_s}} (\vec{q} \cdot \hat{e}_{j,s,\vec{q}-\vec{H}_{l'}}) e^{-i\vec{q}\cdot\vec{r}_s} \right|^2 . \tag{2.27}$$

Here the periodicity of the polarization vectors, $\hat{e}_{j,s',\vec{q}} = \hat{e}_{j,s',\vec{q}+\vec{H}_l}$, reduces the sum over l' to M identical terms dependent on the reduced wavevector of $\vec{q}$ defined as $\vec{k} = \vec{q} - \vec{H}$. Here, H is the nearest reciprocal lattice vector to $\vec{q}$ (Figure 2–3(a)) therefore $\vec{k}$ is always found in the first BZ of the reciprocal lattice. The expression for the diffuse scattering intensity at wavevector $\vec{q}$ is written in its final form,

$$I_1(\vec{q}) = M I_e \sum_j \frac{(n_{j,\vec{k}} + \frac{1}{2})}{\omega_{j,\vec{k}}} \left| F_{1j}(\vec{q}) \right|^2 , \tag{2.28}$$

with the *one-phonon structure factor* is defined as:

$$F_{1j}(\vec{q}) = \sum_s e^{-M_s} \frac{f_s(q)}{\sqrt{\mu_s}} (\vec{q} \cdot \hat{e}_{j,s,\vec{k}}) e^{-i\vec{q}\cdot\vec{r}_s}. \tag{2.29}$$

2.6 Application and analysis

These diffuse scattering equations, 2.28 and 2.29, have previously been applied to extract phonon dispersion relations from thermal diffuse scattering data [3, 51, 55, 56]. Typically, these methods assume a lattice temperature ($n_{j,\vec{k}}$ is known) and calculate or fit for $\omega_{j,\vec{k}}$ using the measured diffuse intensity. This is an appropriate approach for systems at equilibrium. For time resolved experiments, the goal is rather different; to determine the changes in $n_{j,\vec{k}}$ and $\omega_{j,\vec{k}}$ following optical excitation. This section will describe a method, developed by the author, for extracting $n_{j,\vec{k}}$ as a function of time from ultrafast diffuse scattering

measurements using predetermined values for the phonon dispersion relations and polarizations.

For every reduced wavevector, there exists an infinite set of scattering vectors, $\vec{q}$, that all share the same $\vec{k}$ due to translational and point group symmetries of the reciprocal lattice. Therefore, one can construct a system of equations using Eq. 2.28 for multiple equivalent scattering vectors, and each equation will be a linear combination of the $3n$ phonon mode occupancies, $n_{j,\vec{k}}$. This system can be expressed as a matrix equation $X\vec{n} = \vec{i}$, where $\vec{n}$ is an vector of length $3n$ whose entries are $n_{j,\vec{k}}$, and $\vec{i}$ is a vector containing the diffuse scattering intensity, $I_1(\vec{q})$, at $3n$ equivalent wavevectors. As long as the matrix X, with entries $x_{j,\vec{q}} = F_{1j}(\vec{q})/\omega_{j,\vec{k}}$. are known, the solution can be found. So the critical component that translates diffuse scattering intensity to phonon occupancies is the matrix of coefficients, $x_{j,\vec{q}}$, which means the phonon frequencies and the one phonon structure factors must be known.

The phonon dispersions for a wide variety materials are available in the literature, including many that use advanced methods to account for anomalous effects such as Kohn anomalies from electron-phonon interactions [47]. The one phonon structure factors, however, are more difficult to determine, primarily due to the lack of quantitative reporting on phonon polarizations. These are required to calculate the dot product $\vec{q} \cdot \hat{e}_{j,s,\vec{k}}$ and the Debye-Waller factor (Equation 2.15). So the methods for calculating phonon frequencies and polarizations described in Section 1.3 are needed more often than not.

Another barrier to finding a complete solution is acquiring sufficient signal at enough scattering vectors. The diffuse scattering signal is ~ 4 orders of magnitude weaker than the Bragg peak signal. Moreover, measurements must be made at at least $3n$, inequivalent (by symmetry) scattering vectors which may cover a large area of reciprocal space. For materials with small unit cells the vectors will be far apart, requiring a large detection area, and for materials with large unit cells, the number of unit cell atoms will be large, requiring more scattering vectors. Also, measurements at the edges of the detector may suffer form poor signal-to-noise and measurements near the center will be compromised by the center beam.

Because of these limitations, the full solution for the time dependent phonon occupancies is not demonstrated in this thesis. But this is often not necessary or even desirable. The focus and interest of a study is usually on a much smaller sub-set of phonons. Fortunately, a partial solution is possible in many systems by measuring only a single scattering vector. Consider Equation 2.29, each scattering vector will have $3n$ terms in the sum. If the one phonon structure factors at that scattering vector are small for all modes except one, call it j_0, the occupancy of that mode will be directly proportional to the diffuse scattered intensity.

$$
\begin{aligned}
I_1(\vec{q}) &\xrightarrow[j\neq j_0]{F_{1j}(\vec{q})=0} NI_e \frac{(n_{j_0,\vec{k}}(\tau)+\frac{1}{2})}{\omega_{j_0,\vec{k}}} |F_{1j_0}(\vec{q})| \\
n_{j_0,\vec{k}}(\tau) &= I_1(\vec{q}) \frac{\omega_{j_0,\vec{k}}}{NI_e|F_{1j_0}(\vec{q})|} - \frac{1}{2}
\end{aligned}
\tag{2.30}
$$

The identification of these scattering vectors enables single mode population dynamics to be measured individually without an energy resolved instrument and

without a full solution to the linear system. In order to find these wave vectors, results from analytical or numerical determinations of the structure factors can be presented in the form of reciprocal space maps. An example of these maps, calculated for the TA mode using the force constants of graphite, are shown in Figure 2–3(b), with the reciprocal lattice points (Bragg peaks) marked in white. These maps chart the *mode activity* as a function of position, similar to the way selection rules work for Raman and infrared spectroscopy. At locations where the one phonon structure factor is zero (blue in the figure), the associated mode is considered inactive. Unlike symmetry-based selection rules for Raman and infrared spectroscopy, these rules are not binary. This is advantageous because even if the one phonon structure factor of a mode is not exactly zero, it can be insignificant if it is much smaller than the structure factors of the other modes. These maps can be directly compared to diffuse scattering data that cover the same range of scattering vectors. Pump-probe diffraction patterns are often presented as intensity differentials so if the pattern 'lines up' with the structure factor map of a particular mode, then that mode's population has changed according to the measured differential intensity.

2.7 Diffuse scattering selection rules

Determination of mode activity simplifies considerably in the long wavelength limit (near zone-center) and can be fully generalized to apply to any ordered material. The following derivations for generalized diffuse scattering selection rules were developed and compiled by the author. Due to the inner product in Equation 2.29, $|F_{1j}(\vec{q})|$ is maximized when $\vec{q} = \vec{H} + \vec{k}$ is parallel to the polarization vectors

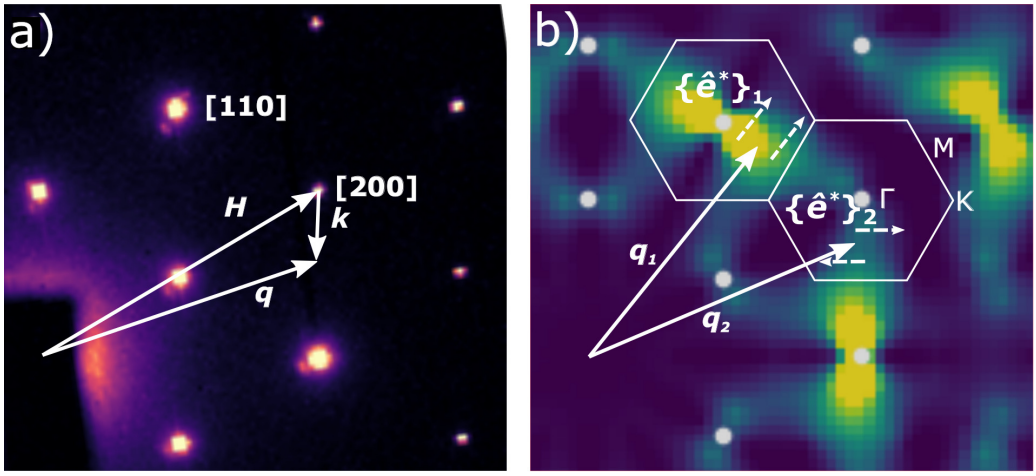

Figure 2–3: Diffuse scattering geometry. (a) Vector diagram of the reduced wave vector, $\vec{k} = \vec{q} - \vec{H}$, overlaying a diffraction pattern of graphite. Select Bragg peaks are labelled by Miller indices, using the primitive reciprocal lattice vectors as a basis. (b) The structure factor map for the TA mode of graphite, the white dots indicate the locations of Bragg peaks (Γ points) and the hexagons show the BZ edges. The first diffuse scattering rule is demonstrated by the bowtie shaped feature parallel to the [110] lattice vector. The phonon polarizations that determine the third diffuse scattering rule are shown constructively and destructively interfering at $\vec{q}_1$ near a bright Bragg peak, [110], and at $\vec{q}_2$ near a weak Bragg peak, [200], respectively.

$(\vec{q} \cdot \hat{\vec{e}}_{j,s,\vec{k}}) = |\vec{q}|$. Consider a transverse mode in the long wavelength limit, $\hat{\vec{e}}_{T,s,\vec{k}} \perp \vec{k}$. Then $(\vec{q} \cdot \hat{\vec{e}}_{j,s,\vec{k}})$ is maximized when $\vec{H} \parallel \hat{\vec{e}}_{T,s,\vec{k}}$, which is biconditional on $\vec{H} \perp \vec{k}$. This can be seen in the transverse acoustic (TA) mode structure factor map shown in Figure 2–3(b), where the features are oriented perpendicular to $\vec{H}$. A second rule is derived using a similar argument applied to longitudinal modes. A third rule can be derived by considering the geometric phase factor, $e^{-i\vec{q}\cdot\vec{r}_s}$, a complex phase found in both structure factors, F_0 and F_{1j}. F_0 has no other complex factor, so any phase difference between them can only be due to the other complex contribution

found in F_{1j}, the phonon polarization vector, $\hat{\vec{e}}_{j,s,\vec{k}}$. If the polarizations for every atom are in phase (*i.e.* long wavelength acoustic modes), this contribution factors out of the sum. Consequently, extinctions, reductions or enhancements of intensity in a Bragg peak due to $e^{-i\vec{q}\cdot\vec{r}_s}$ also affect the phonon scattering from LA and TA modes nearby. A schematic of the vectorial contributions to diffuse scattering of graphite is shown in Figure 2–3(b).

In summary, the three diffuse scattering selection rules for long wavelength modes are:

1. Transverse modes are active perpendicular to the radial direction.
2. Longitudinal modes are active along the radial direction.
3. Acoustic modes are active near the brightest Bragg peaks of a given order.

These rules can be combined to conclude that acoustic modes will be easiest to measure since they will always have areas where they are strongly active near bright Bragg peaks and they will be easily differentiated because they scatter in orthogonal directions.

Mode activity can also be determined qualitatively through context, which can be crucial to understand time resolved scattering signals. Take for example, a material in which a particular phonon mode couples very strongly to the electron system. If time resolved diffuse scattering is observed immediately after electronic excitation, the increases in scattering that happen on the shortest time scales at the corresponding scattering vectors can be attributed to the strongly coupled mode.

The proposed methodology is to apply these results in order to extract differential phonon population spectra from pump-probe ultrafast electron diffuse scattering measurements. The first step is to determine mode activity by mapping mode activity through structure factor maps, weighted dispersion curves, diffuse scattering selection rules and *a priori* knowledge of the scattering material. Then, at the scattering vectors with single mode activity, quantitatively determine the differential phonon population for each pump-probe time delay using Equation 2.30.

CHAPTER 3
Experimental methods

3.1 Pump probe techniques

When considering the experimental possibilities of studying structural and excitation dynamics, one must consider the temporal resolution required to observe any changes in real time. For example, an electron in a superposition of two stationary states will oscillate with a period of $T = 2\pi\hbar/\Delta E$. Typical electronic energy spacings range from 0.1 - 1000 eV which translates to oscillatory periods 0.001 - 10 fs. This is much faster than the typical vibrational periods in a crystal lattice, which range from 10 - 1000 fs (1 - 100 meV). To capture a 'movie' of how these excitations evolve requires an instrument that can execute a sequence of snapshots each illuminating the sample for an ultrashort interval. No mechanical shutter can be quick enough to capture ultrafast events, but the effect of minimizing the duration of illumination can be achieved by shortening the radiation pulse itself. Femtosecond laser technology delivers this capability, producing laser pulses around 30 fs in duration opening the door for time resolved experiments that can view of structural and excitation dynamics as they occur on their natural timescales. Moreover, the large energy bandwidth of ultrashort pulses, guaranteed by the uncertainty principle (30 fs $\sim$ 10 eV), is large enough to bridge the separation between electronic energy levels, and therefore femtosecond laser pulses can drive electronic excitations as well as observe the subsequent

dynamics. These properties enable a family of techniques called pump-probe experiments.

A simplified example of a pump-probe geometry is shown in Figure 1–2. Here the pump pulse arrives at the sample to initiate the process which is the subject of interest. After a fixed time delay the probe pulse arrives and an aspect of its character, such as its transverse intensity distribution or spectral content, is modulated by the average configuration of the sample before travelling to the detector, either by transmission or reflection. The optical techniques that can implement a pump-probe scheme include visible/IR/Raman spectroscopy [57–61], THz spectroscopy [62, 63], ARPES [64, 65], and x-ray/electron diffraction[27–29]. This chapter will cover the detailed configuration of the pump-probe electron diffractometer built and operated by the Siwick Research Group at McGill University which has the exceptional electron pulse brightness and time resolution required to execute UEDS measurements.

3.2 Ultrafast electron diffraction

Ultrafast electron diffraction techniques have been steadily improving since they were first used in 1984 to study the laser-induced melting of thin-film aluminum, measuring a transient signature on the 20-100 ps time scale [66]. The ultrashort electron pulses in this initial work were measured to be 100 ps long, much longer than the 15 ps laser pulses used in their generation via the photoelectric effect. An elongation of the electron pulse deteriorates the time resolution directly and is a fundamental problem for ultrafast electron microscopy techniques. The phenomenon is attributed to *space-charge* effects; the repulsive

Coulomb forces that act in the longitudinal direction along which the electrons are most densely packed. Although the application of femtosecond laser pulses would improve the time resolution to 1 ps [67], further improvements required methods that avoid or directly counteract space-charge effects.

The detailed characteristics of the elongation phenomenon was successfully modelled by Siwick *et. al.*, using mean field theory and N-body simulations to reveal the phase space behaviour of ultrashort electron pulses as they propagate [68]. The results show that the pulses become *chirped*, developing a linear relationship between electron velocity and longitudinal position (Figure 3–1). This correlation develops on the nanosecond time scale, and for electrons travelling at half the speed of light (100 keV electrons) this corresponds to a propagation distance of 15 cm. From this understanding, several solutions to the space-charge problem were developed. The simplest scheme, which is still commonly used in modern UED setups, is to ensure that the total electron path length is as short as possible to minimize the time that space-charge effects can occur [69]. Another solution is to use electron pulses with electron energies in the MeV range as high electron velocities near the speed of light will have a reduced effect from longitudinal broadening [70]. Relativistic UED instruments are being developed by several research groups [71, 72], despite their large scale and high cost compared to non-relativistic approaches.

Single-electron, compact and relativistic UED setups try to reduce space-charge broadening by designing instruments that minimize the space-charge effect. A third approach attacks the problem more directly by actively compressing the

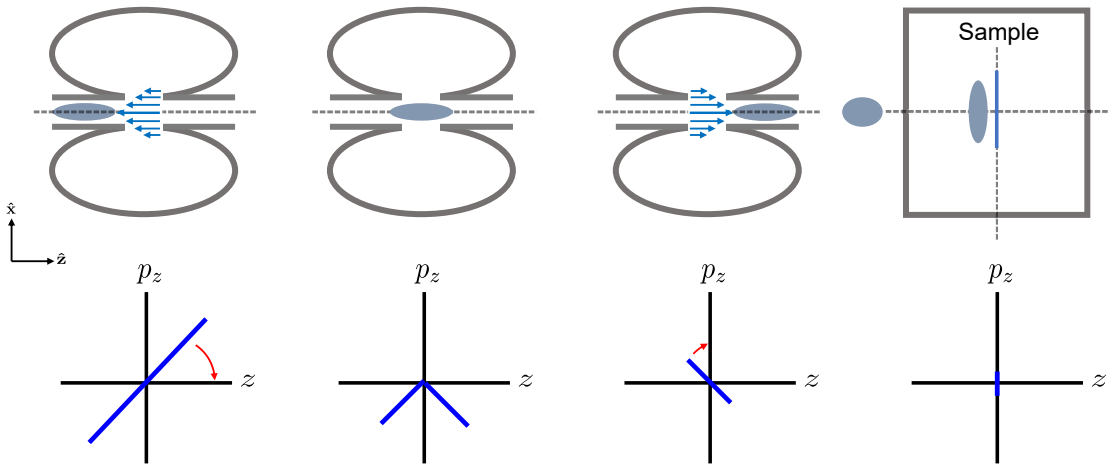

Figure 3–1: Reversal of the space charge effect on electron pulses using a radio frequency cavity operating in a transverse magnetic mode. When synchronized correctly, the cavity fields (shown with blue arrows) invert the position-momentum (z-p_z) distribution of the electron pulse. After the RF cavity interaction, the electron pulse ballistically compresses itself during propagation.

electron pulse. If the linear position momentum relationship shown in Figure 3–1 can be reversed, the pulse will ballistically compress as it continues to propagate. This approach has been applied by using a passive electrostatic mirror, called a reflectron [73], or by exposing the pulse to an electric field [34]. The latter technique, which is achieved by using a radio-frequency (RF) compression cavity (Figure 3–1), is used for the UEDS experiments discussed in the following two chapters.

The instrumental layout of the ultrafast electron diffractometer is shown in Figure 3–2. Broadly stated, the technique uses the pulsed output of a femtosecond

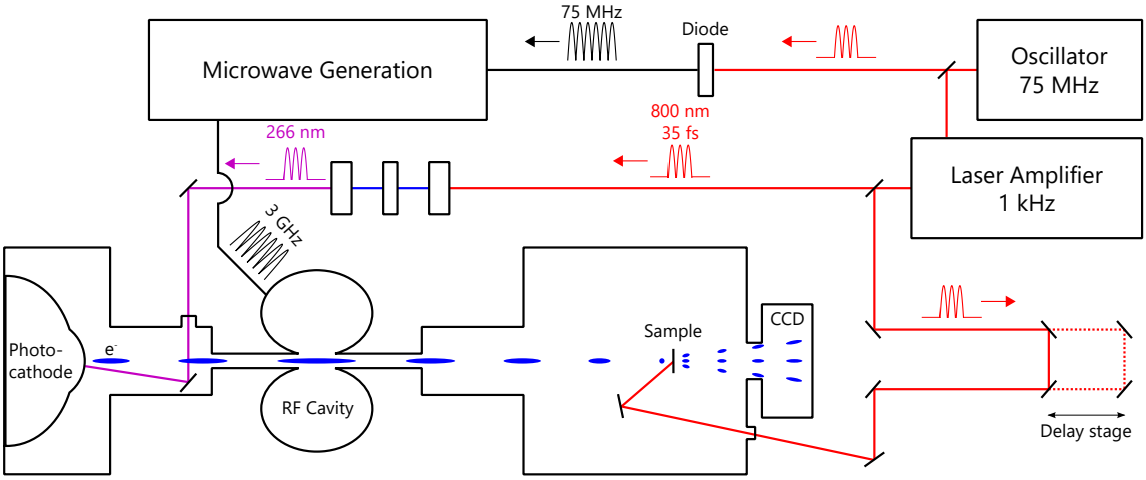

Figure 3–2: Schematic diagram of the UED instrument. The laser system outputs 3 mJ, 35fs infrared pulses which are split into two separate paths. The first path is followed by the pump pulse and is variably delayed by a retroreflector mounted on a motorized linear stage before arriving at the specimen. The second path provides the electron probe pulse by first frequency tripling to a UV wavelength by non-linear optics before photoexciting the copper cathode to emit electrons. The electron beam is accelerated by a 95 kV DC field and travels through the RF compression cavity (which is synchronized to the oscillator output), steered and focused by magnetic solenoid lenses, towards the specimen. Last, the diffraction pattern is detected at a CCD camera which can capture the total scattering from many probe pulses in a single exposure.

laser for both pump and probe pulses, separating them with a beamsplitter. The pump pulse follows a path with an adjustable length to manipulate the pump-probe delay, and is steered onto the sample to initiate the phenomenon of interest. The electron probe pulse is generated using the photoelectric effect, by steering one of the ultrashort pulses onto a copper cathode suspended in a high-voltage DC electric field. The electrons are accelerated by the field and they are steered and focused with magnetic solenoid lenses through the RF compression cavity, the sample and onto a CCD camera (Gatan UltraScan 1000). The details of this

configuration and how it was optimized for UEDS will be described in detail in the following sections.

3.3 Optical Setup and pulse generation

The ultrashort laser pulses are generated by a Newport Spitfire Pro XP CPA laser amplification system. The pre-amplified pulses are generated by a Newport Tsunami, a titanium sapphire passively mode-locked laser oscillator which produces 5 nJ, ∼100 fs pulses with a repetition rate of ∼75 MHz. The repetition rate of the oscillator can be modulated through the cavity length by a motorized linear stage. The oscillator pulse train seeds the Spitfire Pro XP Ti:sapph CPA regenerative amplifier which outputs 3 mJ, 35 fs pulses at a rate of 1 kHz which and can be periodically blocked with minimal degradation in pulse quality in order to achieve lower repetition rates. The final output pulse bandwidth is ∼40 nm centred at 800 nm. The output pulses are split with a 50/50 beamsplitter to form the pump and probe pulses.

The pump line consists of a variable ND (neutral density) filter to control pump energy, an optical delay stage and a focusing lens mounted to a vernier micrometer stage. The components of the optical delay setup are a gold coated retro-reflector mounted on a linear delay stage with a range of 20 cm, providing a variable pump-probe delay of ∼1.3 ns and a minimum step size of ∼1 μm, equivalent to a minimum temporal step size of ∼5 fs. The pump pulse is then attenuated by the ND filter and focused to a point immediately behind the sample by modulating the lens' micrometer stage. In this way the radius and energy of the excitation pulse can be controlled to achieve the desired pump fluence.

The remaining half of the beam power is used to generate the electron pulses via the photoelectric effect. Ultraviolet pulses are generated from the 800 nm pulse using a third harmonic generation scheme. First the pulses are sent through a barium borate (BBO) nonlinear crystal which converts some of the 800 nm light into 400 nm light. The 400 nm pulses are produced through type I second harmonic generation and are polarized orthogonal to the 800 nm pulses [74]. The difference in group velocity of the 800 nm and 400 nm light causes the pulses temporally separate as they travel through the BBO crystal. This relative delay is removed using a birefringent calcite crystal through which the 800 nm light has a lower group velocity than the 400 nm light reversing the temporal separation of the pulses. A second BBO crystal is then used to induce type II sum frequency generation and 266 nm pulses polarized orthogonal to the 800 nm pulses are produced. The three overlapping pulses are then separated using a prism compressor configuration where the 800 nm and 400 nm pulses are blocked while the UV pulses pass through a focusing lens before entering the electron generation and acceleration chamber striking the centre of a copper target (photocathode) from which the probe electrons are ejected and accelerated by a DC (constant) electric field.

The photocathode is mounted in a cylindrical high vacuum chamber with a pressure rating of $< 10^{-7}$ Torr. The vacuum is achieved using a turbo pump/scroll pump combination. The high voltage power supply is a Heinzinger PNChp which is connected to the photocathode by a commercially available high voltage feedthrough, rated for 100 kV. The power supply produces voltages as high as 150

kV, with a voltage stability of 0.001%, or 1 V, at 100 kV. Because of this high level of stability, the an arrival time of the electron pulse at the sample does not fluctuate more than 10 fs. Arrival time jitter directly disturbs the time resolution of the instrument by making the pump-probe delay inconsistent, so this feature of the HV supply is imperative. After acceleration by the DC field, the electrons travel down the high vacuum optical line at $\sim$ 90 kV. The beam direction and transverse beam properties are modulated using a current controlled wire solenoid functioning as a magnetic lens. The current and position of the lens are tuned to collimate the beam through the RF compression cavity.

3.4 RF cavity and synchronization

As stated previously, the concept of electron pulse compression using a time dependent electric field results from the observation that electron pulses develop a linear position-momentum correlation as a result of space-charge expansion, shown in Figure 3–1. In order to easily conceptualize the function of a compression cavity, consider a toy model in the shape of a 'pillbox', a cylindrical shape with flat conducting faces normal to the electron beam axis. The electromagnetic fields that solve Maxwell's equations in this geometry are oscillating modes with their electric fields pointed in the longitudinal direction, resulting in the the longitudinal magnetic field being zero everywhere in the cavity. The lowest of these modes, TM010, has no azimuthal and longitudinal periodicity and one node in the radial direction at the cavity wall. Since this mode offers purely longitudinal electric fields, it is commonly used in RF compression cavities [75].

Figure 3–1 shows a schematic of the approximate fields needed to reverse the phase space character of the pulse so that instead of stretching it compresses as it propagates. In order to achieve this, the cavity is driven by a RF power source which results in a electric field oscillating at a radio frequency. An electron pulse passing through the cavity will be compressed if the resonant period is long with respect to the electron pulse length and the arrival of the pulse in the cavity must coincide with the zero crossing of the oscillating field so that the pulse experiences a linear field. Figure 3–1 shows the time line of the phase space behaviour of the pulse. Initially, the electron pulse is short and the electron velocities uncorrelated. After acceleration and a sufficient propagation time, the electrons have a linear position-momentum correlation. The electric field of the cavity accelerates the leading electrons in the longitudinal direction and as the pulse transits the cavity, the field switches direction linearly, accelerating the trailing electrons in the positive z direction. The pulse then compresses ballistically as it propagates toward the temporal focus, where the sample is positioned. In practice, a more efficient cavity design is used with a resonant frequency of 2.99 GHz. The cavity has a lobed design, symmetrical around the electron beam axis [34, 76]. The field strengths in the cavity reach 10 MV/m at the centre of the cavity. The temperature dependence of the resonance frequency is linear, approximately 0.5 MHz/°C, and so a high performance recirculating chiller is used.

As the pulse travels through the cavity the compression field is effectively linear, thus small errors in the phase of the cavity do not affect the pulse duration substantially. However, if the pulse does not arrive exactly at the zero crossing,

a net acceleration/deceleration of the pulses will occur which will change the pulse arrival time at the sample. Fluctuations in the temporal synchronization of the cavity with the electron pulse results in a lower effective time resolution for the measurements which is a critical problem. To achieve a time resolution of < 100 fs, phase stability of the RF cavity must be less than $\sim$1 mrad [34]. The synchronization scheme, uses the direct generation of microwaves from the harmonics of the oscillator repetition rate and active phase stabilization. This method was implemented by Martin Otto and is detailed in reference [36]. The RF cavity approach offers probe pulses with very high brightness (10^6 electrons per pulse) allowing small changes in diffuse scattering to be measured reliably. This feature, which does not detract from the excellent time resolution ($\sim$ 100 fs) achieved through RF compression and direct synchronization, makes this instrument capable of capturing meaningful UEDS data. However, in order to measure phonon modes at any wavevector, the exact position and angle of the sample must be precisely controlled so that different planes of scattering space can be imaged. The following upgrades to the instrument were designed with this requirement in mind.

3.5 Sample chamber

Originally, the UED sample was mounted in a large cubic vacuum chamber and was manipulated with automated linear stages. Several optics were also placed in the chamber to steer the pump beam onto the target. A major problem with this design was that any angular adjustment of the sample position or pump beam steering had to be done at atmospheric pressure, requiring frequent long

pump-down times as well as difficult and unreliable beam and sample alignment. Moreover, a complete UEDS analysis requires measuring the scattered intensity from several planes in reciprocal space to observe the phonon contributions for all wavevectors $\vec{k}$. Therefore accurate and reliable angular control of the sample is imperative for a complete UEDS analysis. A new compact chamber, designed by the author with support from several technicians at the McGill department of physics, was created to solve these problems.

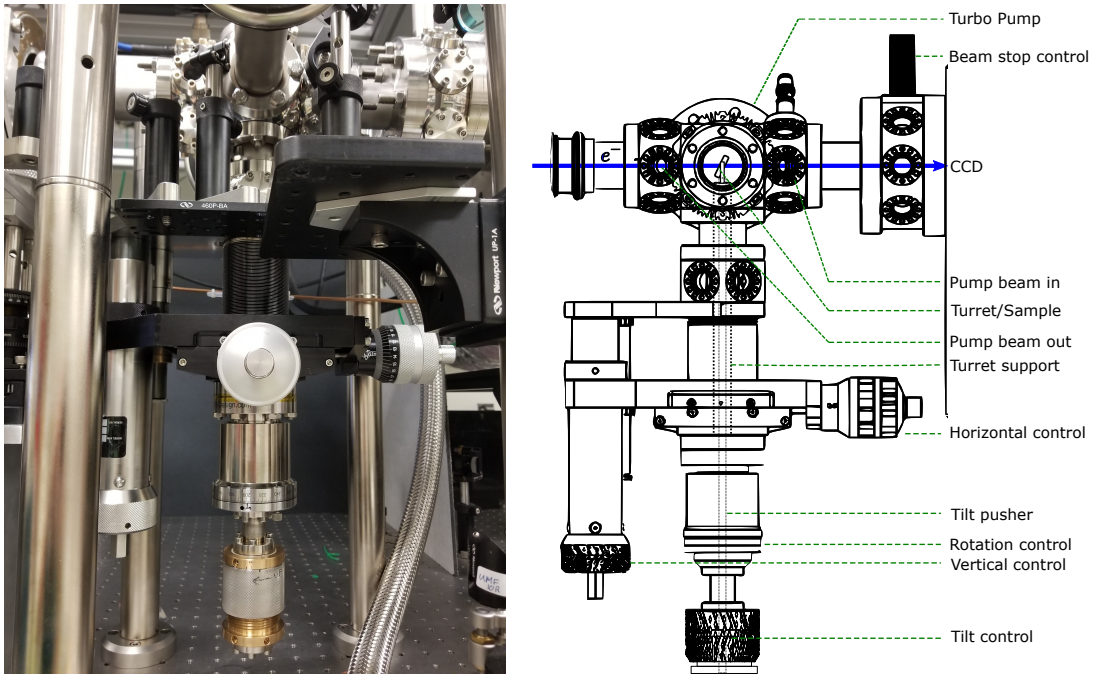

Figure 3–3: Image and drawing of the sample chamber with the various control features and important components labelled. The electron beam direction is shown in blue.

A schematic of the chamber is shown in Figure 3–3. The sample is held in a copper frame at the centre of a 2-3/4" spherical cube. The frame is mounted to a

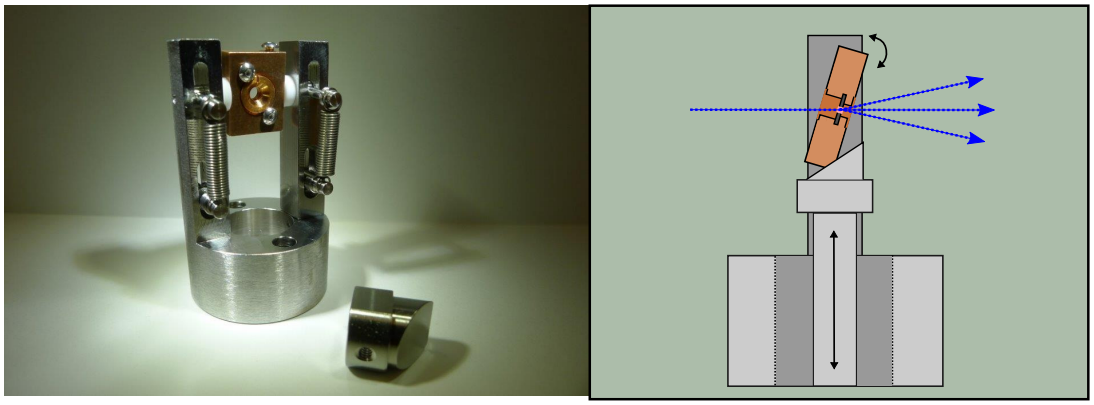

Figure 3–4: Picture and sectioned drawing of the spring loaded wedge mechanism for angluar control about the transverse axis (tilt). Linear motion of the wedge controlled by the screw action stage at the lowest end of the chamber modulates the angle with up to 35° of range.

'turret' anchored to a long, 1" diameter supporting tube which can be manipulated with a rotational feed-through allowing full 360° manual control around the vertical axis. Linear motion is achieved using a 3-way linear micrometer stage with 0.5" of horizontal range and 2" of vertical range, allowing the sample frame to be completely removed from the chamber without breaking vacuum in order to diagnose and optimize the electron beam quality. For angular control about the transverse axis (tilt), a wedge on a vertical linear rail is used, shown in Figure 3–4. A 1/4" rod anchored to a screw action vertical stage with a 1/4" range is fed through the rotational feed-through and the 1" diameter supporting tube. At the uppermost tip of the rod, a ∼45° wedge is coupled to the copper frame which is spring loaded to stay firmly braced to the wedge. Vertical movement of the wedge corresponds to an angular (tilt) adjustment of the wedge providing around ∼35° of range. The fine control provided by the sample holder turret allows the orientation

diffraction plane to be precisely set within 0.5° effectively boosting elastic and diffuse scattering signals by minimizing any misalignment of the Ewald sphere.

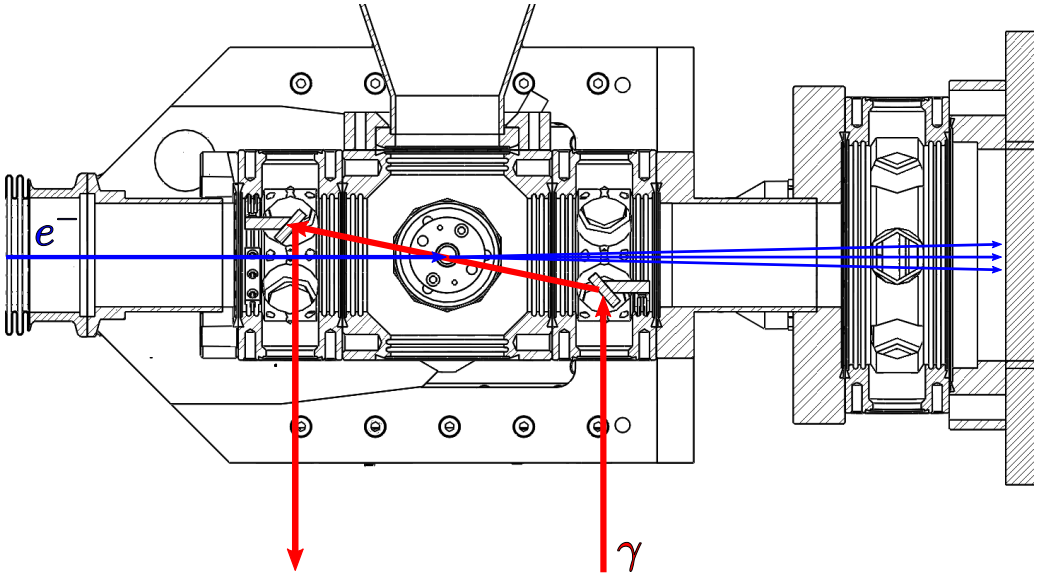

Figure 3–5: Top down sectioned view of the sample chamber. The electron beamline is shown in blue and the laser beamline is shown in red. the electron beam is steered through the sample with a magnetic solenoid lens. The pump beam is steered into the chamber using exterior optics and focused onto a point a few mm left of the sample depending on the desired beam size and fluence. The outgoing laser beam is measured by a photodiode as an alignment diagnostic tool. The mirrors shown in the diagram (7mm dia., silver) are fixed and mounted inside the vacuum chamber.

A top down view of the chamber showing the pump and probe beam lines are shown in Figure 3–5. The ability to steer the pump pulse out of the chamber after photoexcitation is imperative for assuring correct alignment of the pump beam onto the sample. The outgoing beam is measured by a photodiode so that the intensity of the beam passing through the sample can be optimized as a function of the linear position of the turret. The turret position at which the signal on

the photodiode is maximum guarantees a uniform and reliable illumination of the sample by the pump beam. The alignment process must be done *in situ*, when the sample is under vacuum, because there is a non-negligible change in beam direction due to refraction as the beam transitions from atmosphere to vacuum. Aligning the beam exactly normal to the sample chamber window also solves this issue, but in practice it is often impossible to achieve perfect alignment with both the window and sample. The improvements to the UED instrument provided by the upgraded sample chamber boosts the reliability of individual experiments via precise and reproducible pump-probe alignment and increases the quality of UED data through fine control of the incident angle of the electron beam, enabling scattering measurements of multiple planes of reciprocal space.

CHAPTER 4
Phonon couplings in Graphite

Graphene and graphite, the 2D and layered allotropes of carbon, are quintessential low dimensional materials and their properties form a basis for our understanding of the rest of carbon's various structures [77]. Graphene is an atomic monolayer in the form of a planar honeycomb lattice and is the thinest material known to material science. Due to its 2D nature it exhibits exotic and unique electronic and structural properties. During electron transport, charge carriers move with close-to-zero effective mass and have extremely long mean free paths (10^{-6} m), allowing for extremely high electrical and thermal conductivities. It is also the strongest and most rigid known material, withstanding 20% elastic strain and extremely high current densities [77–80]. These unique properties are attractive for many applications including high-speed electronics, single-molecule chemical sensors, photonics and optoelectronics [78, 81].

When graphene sheets are vertically stacked, as shown in Figure 4–1, they are held together by relatively weak Van der Walls interaction produced by a delocalized π-orbital [82], forming graphite. Graphite's structure is strongly anisotropic, as are its corresponding properties. The strong thermal and electrical conductivities of graphene are inherited by graphite but only in the planar direction. The weak inter-planar bonds allow easy lateral movement of the layers, making graphite a good lubricant, and allowing thin graphite, or even single layer

graphene, samples to be made through mechanical or liquid exfoliation [83, 84]. Ultrafast studies of graphite have focused on the electronic and structural response of the material to pulsed laser illumination. Previous ultrafast electron and x-ray diffraction studies have focused on a variety of effects, including: lattice contraction of the interlayer bond and plasmon dynamics [85–87], the graphite-diamond phase transition [88], strain [89] and unit cell disorder in the basal-plane [90].

This chapter will focus on graphite's electronic and vibrational response to pulsed laser photoexcitation as well as the interplay between the electron and lattice systems from the novel perspective of the dynamic phonon populations. Graphite is an excellent material to test the UEDS methodology due to the wealth of high-quality reliable data from other techniques available for comparison. In particular, recent results from trARPES and TRR experiments will be compared with the UEDS findings. The methodology for measuring phonon population spectra across the entire BZ developed in sections 2.6 and 2.7 will be demonstrated for the case of graphite, providing novel insights into the charge/lattice couplings and establishing a standard point of comparison for future UEDS studies.

4.1 Structure of graphite

To facilitate the calculation of the phonon dispersion and polarizations of graphite, the details of the atomic configuration are presented here. The graphite's layered structure is shown in Figure 4–1, with graphene sheets stacked in an AB sequence. The Bravais lattice is hexagonal with lattice constants $a = 2.46$ Å , $c = 6.71$ Å and lattice vectors:

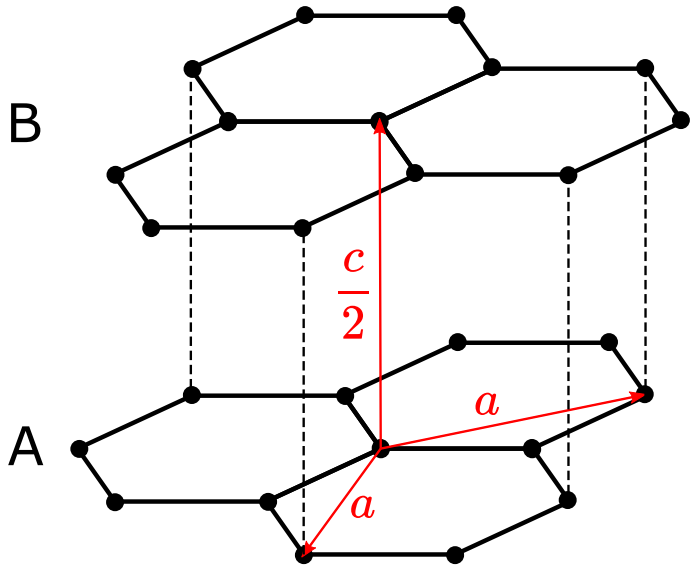

Figure 4–1: The structure of graphite with AB stacking. $a = 2.46$ Å, $c/2 = 3.35$ Å. The solid black lines represent strong covalent bonds and the dashed lines represent Van der Walls forces.

$$\vec{a}_1 = a\,[1,0,0]\,, \vec{a}_2 = a\left[-\frac{1}{2}, \frac{\sqrt{3}}{2}, 0\right], \vec{a}_3 = c\,[0,0,1] \tag{4.1}$$

There are four carbon atoms in the unit cell. Their locations in Cartesian and lattice coordinates are given in Table 4–1. The reciprocal lattice vectors for graphite are (as calculated using Eq. 1.1).

$$\vec{b}_1 = \frac{2\pi}{a}\left[1, \frac{1}{\sqrt{3}}, 0\right], \vec{b}_2 = \frac{2\pi}{a}\left[0, \frac{2}{\sqrt{3}}, 0\right], \vec{b}_3 = \frac{2\pi}{c}\,[0,0,1] \tag{4.2}$$

The high symmetry points of the hexagonal BZ including Γ, M and K are shown in Figure 1–3.

The electronic band structure for graphene near the Fermi surface is shown in Figure 4–2. So called Dirac cones are located at the K points and oriented along

Basis	$\vec{r}_1$	$\vec{r}_2$	$\vec{r}_3$	$\vec{r}_4$
Cartesian	[0, 0, 0]	$\left[0, \frac{a}{\sqrt{3}}, 0\right]$	$\left[0, 0, \frac{c}{2}\right]$	$\left[\frac{a}{2}, \frac{a}{2\sqrt{3}}, \frac{c}{2}\right]$
Lattice	[0, 0, 0]	$\left[\frac{1}{3}, \frac{2}{3}, 0\right]$	$\left[0, 0, \frac{1}{2}\right]$	$\left[\frac{1}{3}, -\frac{1}{3}, \frac{1}{2}\right]$

Table 4–1: Atomic positions in graphite with Cartesian and lattice coordinates.

the *H*-*K*-*H* line. These cones are perfectly sharp in graphene which gives the near 'massless' property to the charge carriers enabling the ultrahigh carrier mobility and fractional quantum hall effects [91]. For thin film graphite, or multiple layers of graphene sheets, the Dirac cones become rounded at the tip removing the zero mass property but the shape of the bands remain qualitatively similar retaining the semi-metallic character [92].

The phonon dispersion of graphite is shown in Figure 4–3. Graphite has 12 phonon modes where graphene only has 6 but their dispersions look very similar due to the degeneracy of the graphite vibrational energies. Each mode in graphite has a nearly degenerate pair due to the weak coupling between planes. For example, The TA mode is degenerate with the pseudo-acoustic TO' mode nearly everywhere except at zone centre. The polarizations of acoustic and pseudo-acoustic modes, however, are always different. One mode has the A and B sheets moving in phase and the paired mode has them moving out of phase. In practice, this degeneracy often results in lumping the degenerate graphite modes together and labelling them as the graphene modes. This labelling will be cautiously used here excepting when the differences in plane polarizations are relevant, especially

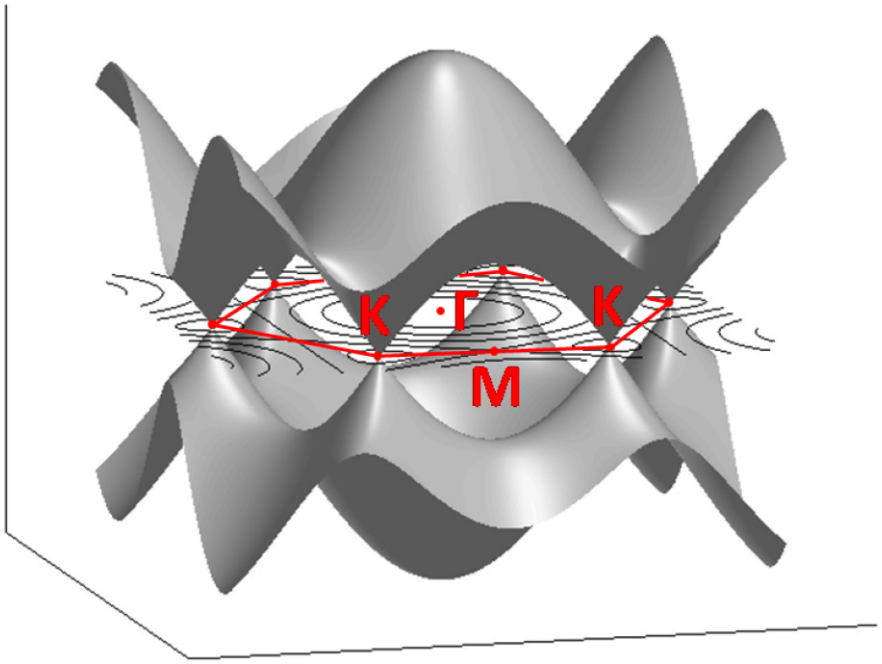

Figure 4–2: Electron band structure of graphite in the first BZ near ϵ_F showing Dirac cones at the K points. Taken with permission from Reference [2].

for the acoustic and pseudo-acoustic transverse and longitudinal modes which will be denoted as TA/TO' and LA/LO'.

Sharp softening of the optical modes (Kohn anomalies) result from a screening effect due to strong interactions with the electron system [47, 49] (Figure 4–3) as discussed in section Section 1.5. This effect only occurs at momentum vectors $\vec{q}$ when there are two electronic states $\vec{k}_1$ and $\vec{k}_2 = \vec{k}_1 + \vec{q}$ on the Fermi surface, *i.e.* nesting vectors of the Fermi surface. Figure 4–4(b) shows how the Dirac cones satisfy this condition at the K and Γ points in graphite. These modes are labelled K-A_1' and Γ-E_{2g}, after their location in the BZ and point group symmetry. Other than these strongly coupled modes, electron phonon interactions in graphite

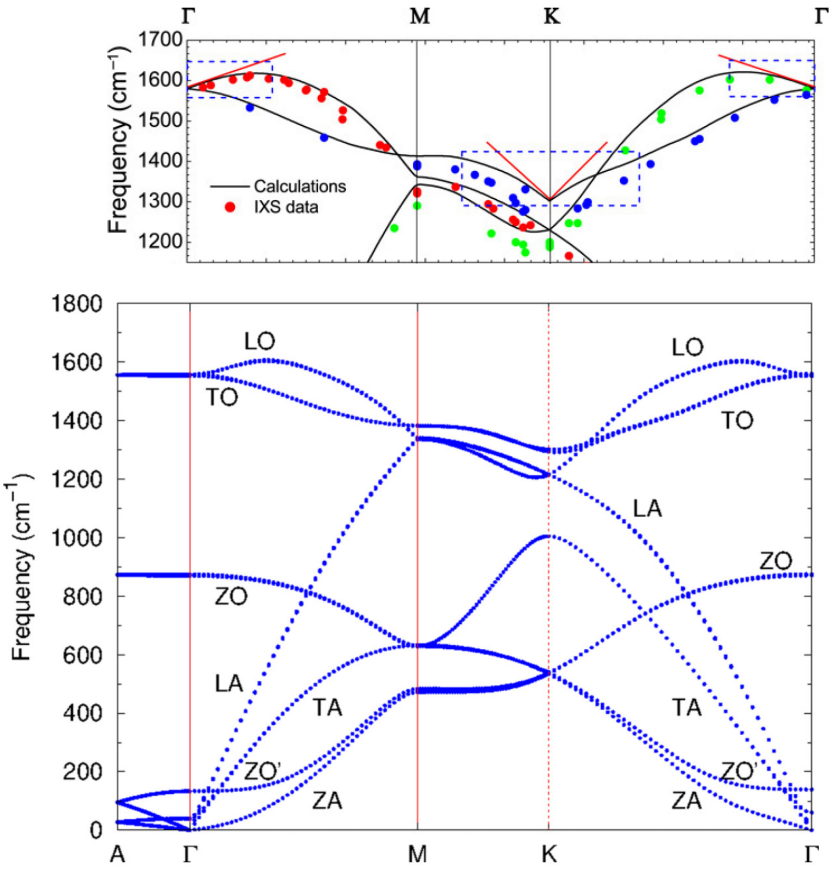

Figure 4–3: (Top) Experimental (inelastic x-ray scattering) and calculated phonon dispersion of the optical modes of graphite showing Kohn anomalies at the Γ and K points. (Bottom) Full phonon dispersion of graphite calculated using density functional theory. Figures taken with permission from References [3] and [4].

are weak on average, resulting in high carrier mobility at low current densities. At high current densities, however, the strongly coupled modes begin to have a deleterious effect [93, 94].

4.2 Photoexcitation dynamics

When 800 nm photons are incident on a graphite sample they excite electron-hole pairs forming an outlying distribution of electrons high above the Fermi level

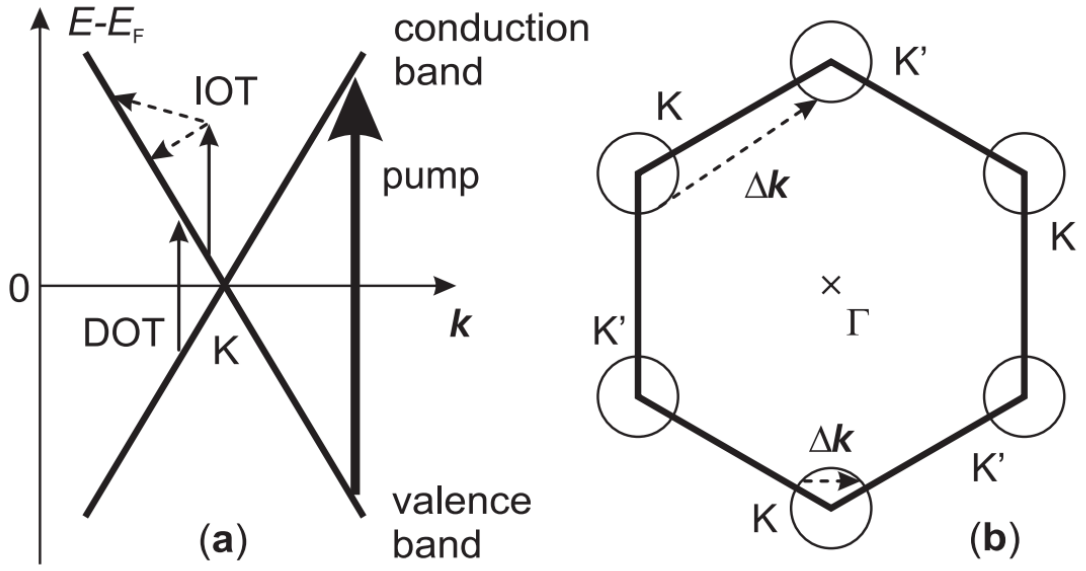

Figure 4–4: Sketch of the in-plane electronic band structure of graphite at the Fermi energy and close to the K point where the valence and conduction bands slightly overlap. Arrows indicate possible direct (DOT) and indirect (IOT) optical transitions induced by the probe pulse. (b) Brillouin zone perpendicular to the [001] axis. Nested vectors of the Fermi surface are located around the K points. Arrows mark possible scattering events of electrons and correspond to wave vector changes that are confined to the vicinity of the Γ and K points. Figure taken with permission from Reference [5].

and a corresponding peak formed by holes in the negative-energy band (Figure 4–4(a)). The photoexcitation cascade proceeds as depicted in Figure 4–5. The high-energy carriers relax, losing energy to phonons or scattering with ambient carriers until the distribution has thermalized [6]. This process has been shown to occur on a time scales from 10-100 fs [5, 95, 96]. After thermalization, the distribution of high temperature electrons cools down by the emission of phonons to the lattice [6].

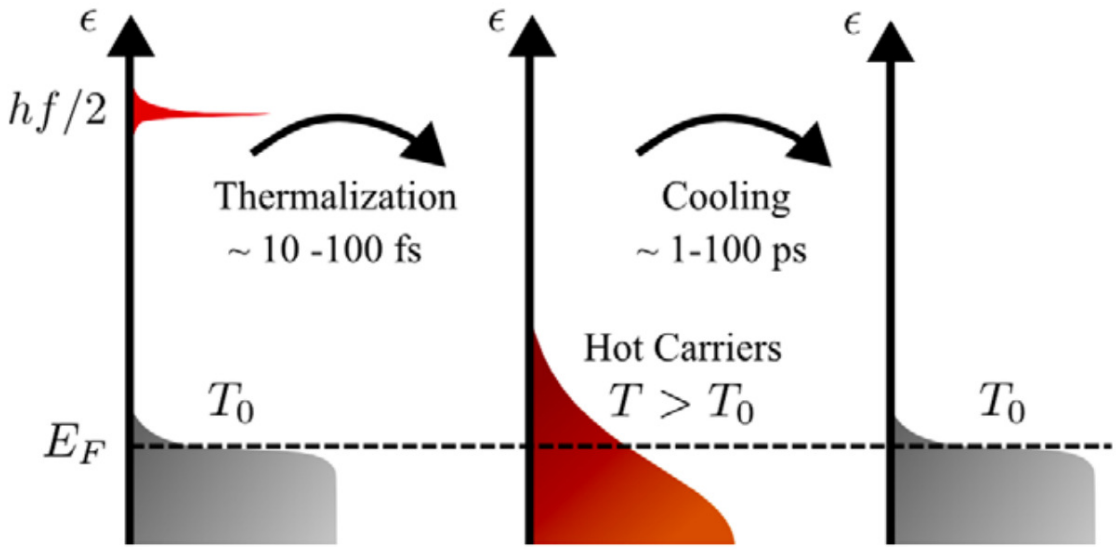

Figure 4–5: Main stages of energy relaxation of photoexcited carriers. First the high energy ($\epsilon = hf/2$) carriers lose energy to carrier-carrier and phonon scattering. These processes lead to fast thermalization, producing a relatively long-lived hot carrier distribution. In the second stage, electron-lattice cooling mediated by phonons takes place over longer time scales relaxing the hot carrier distribution back to equilibrium, T_0. Figure taken with permission from Reference [6].

Time and angle resolved photoemission spectroscopy can measure the photoexcitation cascade in graphene and graphite from the perspective of the non-equilibrium electronic occupancy on the Dirac cones and the corresponding statistical distribution of carriers in both momentum and energy space. Figure 4–6 shows trARPES spectra of graphene taken at equilibrium and different delays after the pump pulse in both raw and differential forms using 800 nm (1.55 eV) 30 fs femtosecond laser light for the pump [7]. An increase of the spectral intensity in the conduction band and a corresponding decrease in the valence band are clearly shown in the raw data (Figure 4–6(c)) and even clearer in the corresponding

difference (Figure 4–6(f)). Slicing the trARPES images at fixed energies yields electronic momentum distribution curves. The distributions have Lorentzian peaks centred at the momentum value of the electron band dispersion. The area under the this distribution can be viewed as the statistical distribution of carriers at a particular time delay and are well described by a Fermi-Dirac function [7, 8]. The evolution of the carrier distribution for graphite is shown in Figure 4–7. Clear deviations from Fermi-Dirac distributions are found only at times < 100 fs [8], which indicates the time required to establish a thermalized carrier distribution through electron-electron interactions is $\sim$50 fs [8, 97]. Afterwards, the electron temperature can be extracted from fits of the Fermi-Dirac distribution. The trace of the electron temperature is shown in figure 4–7. The fast component of the temperature decay ($\sim$ 250 fs) is associated with coupling to the strongly coupled optical modes at Γ and K [3, 47] and the slowest component ($\sim 5ps$) is a composite timescale from optical and acoustic phonon dynamics.[5, 13].

To look at the corresponding phonon occupation dynamics, TRR studies are able to follow the excitation of some optical phonons near zone-centre. The time dependance of the anti-Stokes Raman intensity, which is proportional to the population of the strongly coupled optical phonon at the Γ point, is shown in Figure 4–8(a) and the corresponding mode temperature is shown in Figure 4–8(c) [9]. The peak shift shown in Figure 4–8(b), indicates an increase in mode frequency that are very small, < 10 cm^{-1} (< 1 meV) and is associated with a dynamic weakening of the electron-phonon coupling and associated Kohn anomaly. The increase in phonon occupancy is a direct result of electron-phonon coupling

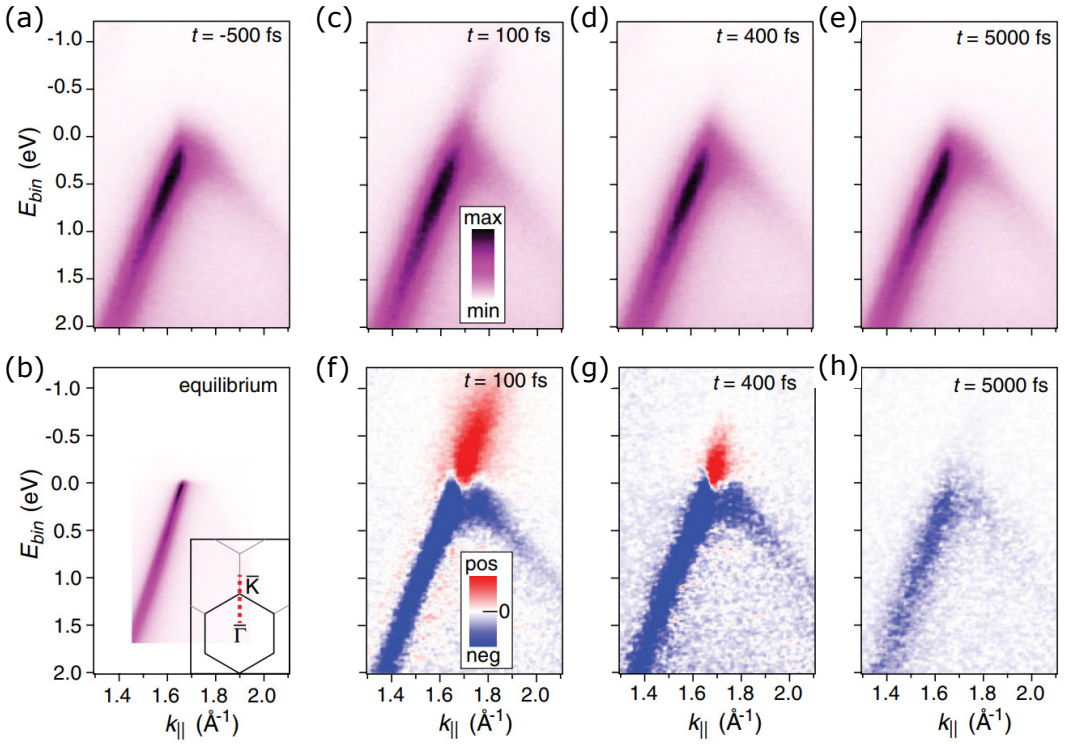

Figure 4–6: (a) Energy (E_{bin}) and momentum ($k_{\|}$) resolved photoemission intensity around the Dirac cone (no pump). (b) Equilibrium high-resolution spectrum. (Inset) Brillouin zone with measurement direction (dashed red line). (c)-(e) Spectra taken at increasing time delays. (f)-(h) Change with respect to the spectrum before the pump pulse (difference spectra). Figure taken with permission from Reference [7].

and has a time constant of less than 300 fs, comparable to the trArpes result (250 fs) and the following slow decay into acoustic modes has a time constant of 2.2 ps.

After the hot carriers relax through exchange with the strongly coupled optical modes, phonon-phonon decay will proceed by funnelling the excitations into the low frequency acoustic branches. The optical phonon anharmonic decay pathways in graphite were investigated using computational methods by Bonini *et. al.* [24]. All the calculations are performed using density-functional theory and

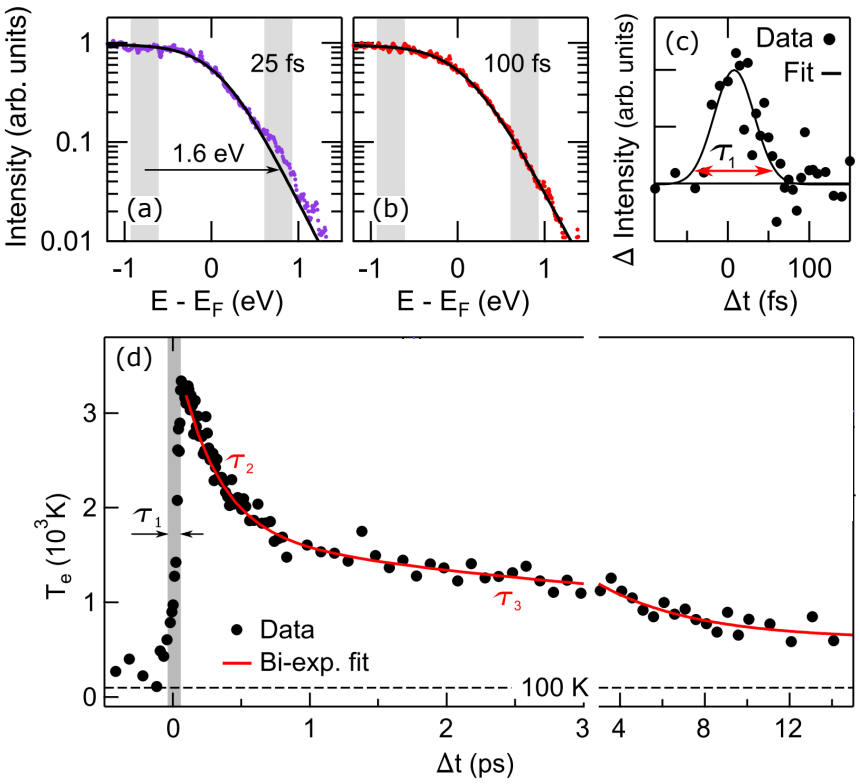

Figure 4–7: (a-b) Electron energy distribution curves derived from trARPES data illustrating the deviation from a thermalized electron distribution shortly after photoexcitation. (c) Nonthermal component of the energy distribution curves as a function of t. (d) Electron temperature transients derived from Fermi-Dirac fits to the energy distribution curves. Figure taken with permission from Reference [8].

density-functional perturbation theory as implemented in the PWSCF package of the QUANTUM-ESPRESSO distribution. The momenutm and energy conserving dominant pathways are shown in Figure 4–9. The orange bars indicate half the energy of the K-A_1' and Γ-E_{2g} modes. The dominant energy and momentum-conserving decay pathways are indicated with colored arrows. For example, the green arrows labeled A_1':TA-LA on the left represent the decay from the strongly coupled A_1' mode at K to both TA and LA modes at the midpoint of the Γ-K

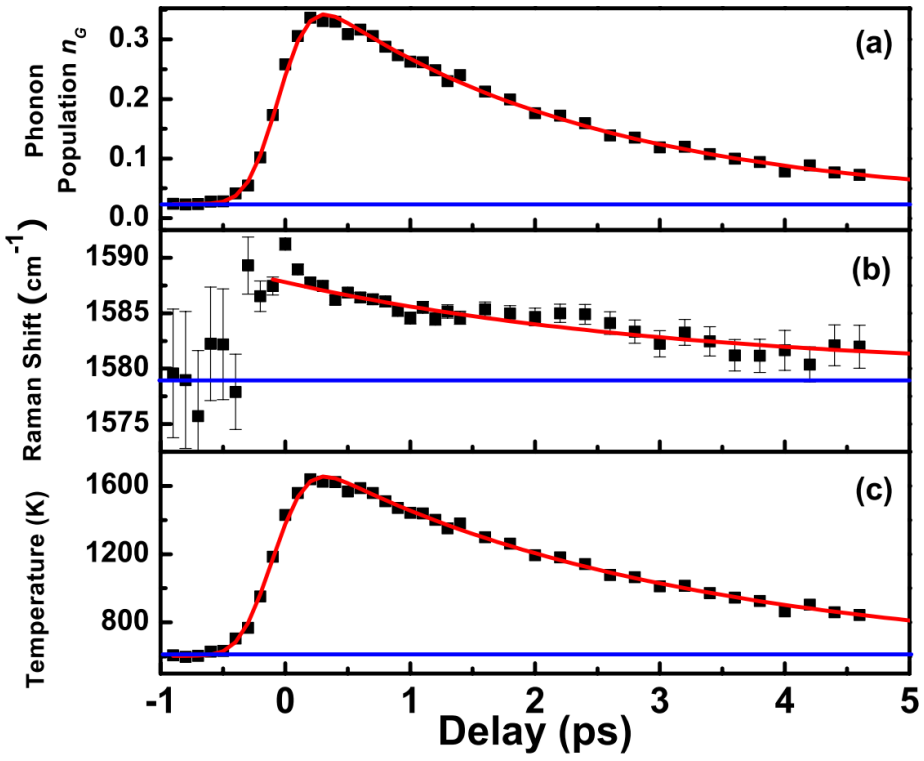

Figure 4–8: TRR graphite results, showing temporal dynamics of the Γ-E_{2g} phonon following pump excitation. (a) Experimental anti-Stokes Raman intensity, which is proportional to the phonon mode population. (b) Measured shifts of the Γ-E_{2g} mode frequency. (c) Temperature of the Γ-E_{2g} phonons inferred from the mode population in (a). Figure taken with permission from Reference [9].

line. Dotted arrows should be thought of as going in the opposite momentum direction. The side bar (red) provides a schematic of the non-equilibrium LA/TA phonon distribution produced through the decay of Γ-E_{2g} and K-A_1' phonons, predicting that most of the phonon excitations will occur at energies associated with mid-BZ phonons. A similar calculation was made for the subsequent acoustic anharmonic decay by Paulatto *et. al.* [25], using an extension of the D3 code of

the QUANTUM ESPRESSO package incorporates the DFPT $2n + 1$ approach to calculate the three-phonon scattering matrix element and therefore the anharmonic broadening/phonon lifetimes (see Section 1.5). For purely transverse modes, there are no allowed three phonon anharmonic decay processes due to momentum and energy conservation laws. Moreover, for modes that are fully transverse or longitudinal, the only allowed interband transitions are, L $\leftrightarrow$ T + T and L $\leftrightarrow$ L + T [11, 12].

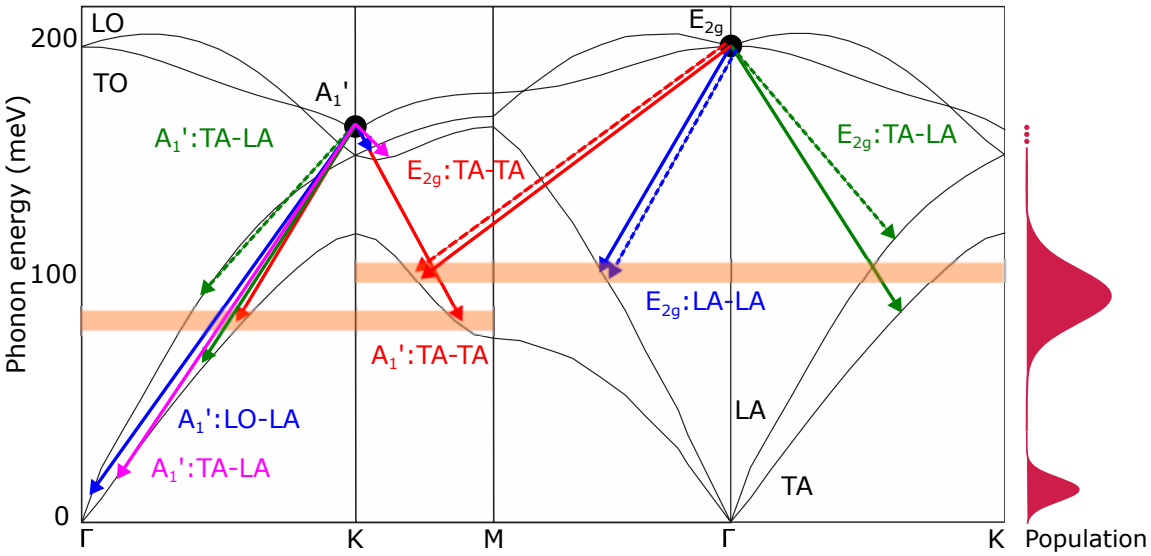

Figure 4–9: Phonon dispersion of graphite with the strongly coupled optical modes indicated. The orange bars indicate half the energy of the K-A_1' and Γ-E_{2g} modes. The dominant energy and momentum-conserving decay pathways are indicated with coloured arrows. For example, the green arrows labelled A_1':TA-LA on the left represent the decay from the strongly coupled A_1' mode at K to both TA and LA modes at the midpoint of the Γ-K line. Dotted arrows should be thought of as going in the opposite momentum direction. Side bar (red) provides a schematic of the non-equilibrium LA/TA phonon distribution produced through the decay of Γ-E_{2g} and K-A_1' phonons. Figure taken with permission from Reference [10].

4.3 UEDS results

Now, a UEDS analysis will be applied to study photocarrier relaxation dynamics in graphite following changes in phonon occupancy. The techniques presented in Chapters 1 and 2 will be demonstrated and the results compared with the literature review in the previous section. First, the specifics of the experimental configuration are presented. The samples for the UEDS experiment were made using single crystal graphite flakes, provided by Naturally Graphite®. The starting flake is glued to a 3mm copper G200 square mesh TEM grid on a glass slide using clear color crystalbond 509. Then, the flake is repeatedly exfoliated with Scotch tape until they became translucent by eye. The crystalbond is then carefully removed with acetone, applying one drop at a time via glass pipette until the TEM grid is freed from the glass slide. Measurements of other specimens made by the same method have shown a final thickness of approximately 80 nm and that the constant greyscale intensity observed by eye is a fairly good indicator of uniform thickness in the sample [75]. The configuration of the UED instrument is detailed in Chapter 3. Here, 800 nm, 35 fs with a fluence of 12 mJ/cm^2 laser pulses were used to photoexcite the thin film graphite and the scattering intensity as a function of pump probe delay, $I(\vec{q},\tau)$, was captured on a CCD camera.

The results are presented as differential diffuse intensity patterns, the difference between the unpumped scattered intensity (measured from images with negative pump-probe delay) and the measured intensity $I(\vec{q},\tau)$ is calculated using,

$$\Delta I(\vec{q},\tau) = I(\vec{q},\tau) - \frac{1}{n}\sum_{t<0} I(\vec{q},t) \tag{4.3}$$

or as fractional diffuse intensity difference for better imaging contrast,

$$\Delta_f I(\vec{q},\tau) = \frac{I(\vec{q},\tau) - \frac{1}{n}\sum_{t<0} I(\vec{q},t)}{\frac{1}{n}\sum_{t<0} I(\vec{q},t)} \tag{4.4}$$

where $I(\vec{q},\tau)$ is the diffraction measurement at time-delay τ, and n is the number of measurements for which $t < 0$ (typically between 10 and 20).

The fractional intensity maps presented in Fig. 4–10 show the raw results of the experiment and the results after several image processing steps which are described here. After the averaging of the experimental repetitions (not shown), several artifacts can be seen to occur in the raw images, two of which are indicated with red arrows in Fig. 4–10 a). The first artifact is due to the beamstop, which blocks the electrons in the center beam as well as a rectangular area in the upper half of the image. The second is a line of artificial intensity, occurring due to a read-out error in the CCD camera, which is visible in the bottom half of the image. To minimize the effect of these artifacts, these features are 'masked' out of further processing steps, which just means that the pixel values at those locations are set to zero. A hexagonal area located at the center of the image is also masked in order to block residual signals from the beam center. The masked image is shown in Fig. 4–10 b).

Even after dozens of experimental repetitions ($\sim$100), the diffuse signals in Fig. 4–10 b) are still barely distinguishable from the random background noise. To add further statistics to the diffuse signal, the natural six-fold symmetry of the features is exploited by taking six copies of the image, rotated by 0°, 60°, 120°, 180°, 240° and 300° respectively, and adding them together. This process

boosts the signal-to-noise considerably, decreasing random noise by a factor of $\sqrt{6} \sim 2.5$. The result is shown in Fig. 4–10c). After six-fold rotational averaging, the asymmetric corners are masked out and the images are smoothed using a Gaussian weighted moving average with a 4 pixel (0.03 Å^{-1}) kernel. Finally, the data is normalized by the scattering vector squared q^2 (as per equations 2.28 and 2.29) so that all features could be clearly seen with a single colormap. The final result is shown in panel d). Thanks to the processing procedure, the image can be shown with ten times the contrast compared to the previous two panels without interference from the background noise. Nonetheless, some artificial signals (the CCD read out error indicated with a red arrow) are not completely removed, so careful consideration of the images at all processing steps is imperative to distinguish different features and artifacts in the final diffuse scattering maps.

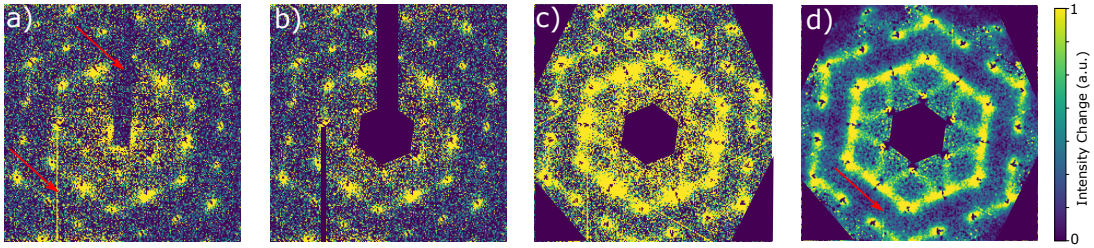

Figure 4–10: $\Delta_f I(\vec{q}, 100\text{ps})$ at various steps in the image processing procedure. a) shows the raw diffraction pattern after averaging the experimental repetitions. Artifacts from the beam block and camera read out are indicated. b) Diffraction pattern after masking of the artificial signals. c) Pattern after six-fold averaging. d) Pattern after Gaussian smoothing.

4.4 Strongly coupled optical modes

The dramatic changes in diffuse scattering shown in figure 4–11 reflect the non-equilibrium phonon populations and their time dependence according

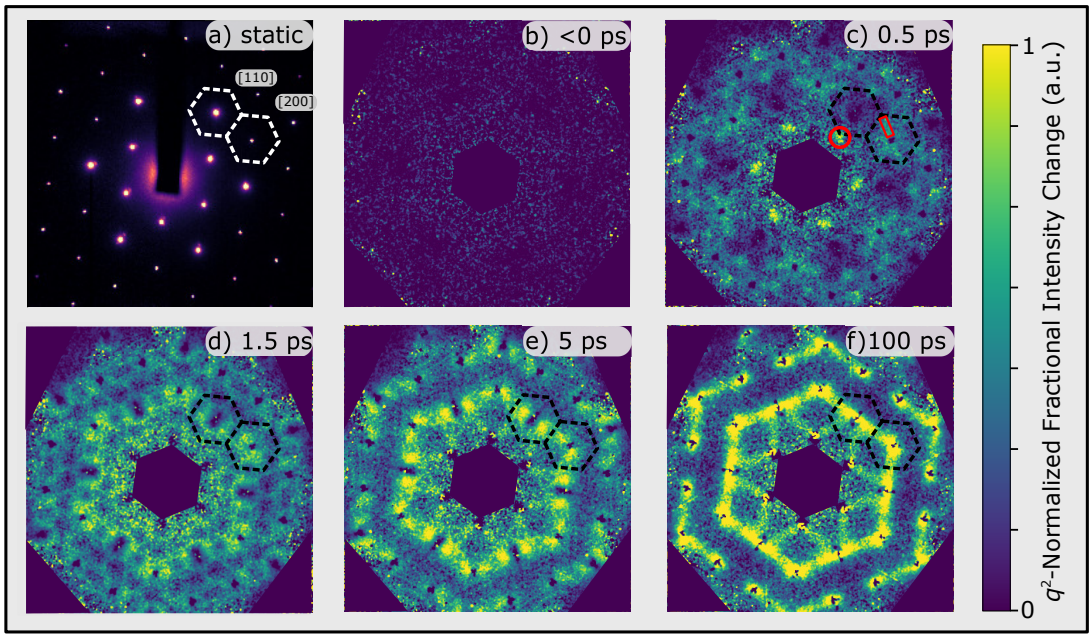

Figure 4–11: Evolution of $\Delta_f I(\vec{q}, \tau)$ following photo-excitation of graphite. The dramatic changes reflect the non-equilibrium phonon populations and their time dependence. a) Raw diffraction pattern of graphite with select BZs indicated with dashed lines. b) Differential scattering flat-field at a time before optical excitation indicating signal-to-noise. c) At early times the diffuse intensity provides a map of the relative strength of the q-dependent EPC coupling through the increased occupancy of strongly-coupled modes. Peaks in $\Delta_f I(\vec{q}, 0.5 \text{ ps})$ at certain $K-$points (circled) result from the increase in K-A_1' population. Strong coupling to the entire transverse acoustic (TO) branch is evident in the vicinity of [200] as ridges of intensity radiating from Γ to K points. (c) By 1.5 ps, a halo of scattered intensity the around the [110] peak appears due to dominant anharmonic decay pathways of the strongly coupled modes. (b) Scattered intensity collects along Γ-M lines perpendicular to the scattering vector. By diffuse scattering selection rules 1 and 2 this is scattering from the TA mode. These dynamics demonstrate interband and intraband pathways from the mid-BZ TA and LA modes. By 100 ps (c) the intensity has tightened around the Γ-M lines lines and the diffuse intensity now has the same shape as the TA structure factor map in Figure 4–12(upper right). This steady state increase in TA mode occupancy is consistent with the lack of allowed anharmonic decay pathways for transverse acoustic modes [11, 12].

to equation 2.28. Using the techniques discussed in Chapter 2, the differential phonon occupancy, $\Delta n_{j,\vec{k}}(\tau)$ as a function of pump-probe delay may be extracted from $\Delta I(\vec{q},\tau)$ by determining the mode activity at each scattering vector. At the earliest pump-probe delays, mode activity is determined qualitatively by considering the electron-phonon coupling strengths; only the most strongly coupled modes have any increased occupancy at the shortest time delays. Therefore, figure 4–11(c) can be understood as a map of the relative strength of the $\vec{q}$-dependent electron-phonon coupling through the increased occupancy of strongly-coupled modes. Peaks in $\Delta I(\vec{q}, 0.5 \text{ ps})$ at the $K-$points around the [110] Bragg peak (circled) result from the increase in K-A_1' population and outline the hexagonal BZ and strong coupling is evident in the vicinity of [200] as ridges of intensity radiating from Γ (the Bragg peak) to K points. These signals correspond with the strongly coupled optical modes discussed in Section 4.2 with the additional conclusion that there is strong coupling along the entire Γ-K line, not only with Γ-E_{2g}. Furthermore, the *a priori* assumptions about the activity of the strongly coupled optical modes at the indicated scattering vectors can be confirmed through comparison with structure factor maps calculated using the density functional theory methods described in Chapter 1.

The structure factor maps for the acoustic and optical modes of graphite are shown in Figure 4–12. They were calculated using the PwSCF and PHonon packages of Quantum Espresso using a $4 \times 4 \times 4$ k-point grid and ultrasoft pseudoptoentials for carbon (wavefunction energy cutoff of 30 Ry) in the local density approximation [45, 46]. The scattering vectors showing TO mode activity

match the locations of the features outlined in red in Figure 4–11(c) supporting the conclusion that these signals correspond to the strongly coupled optical modes and revealing strong electron-phonon coupling strength across the entire TO branch along the Γ-K line. Although TRR has previously been employed to follow the occupancy of the zone center $\Gamma - E_{2g}$ mode showing that it is indeed strongly-coupled [9, 31]. Evidence for strong coupling to the off-zone-center modes, however, have previously only been indirect [13]. The peaks in Figure 4–11 c) represent the first direct observation of this effect.

The complete time-dependence of the diffuse intensity at high symmetry points is shown in Figure 4–13. $\Delta_f I(\vec{q}, \tau)$ shows a qualitatively distinct time-dependence where the LO mode is active (Figure 4–13 b), green) versus K-points where the TO mode is active (Figure 4–13 b), red). This includes a much slower initial rise; 730 fs (K-LO) compared to 280 fs ($K-$TO). Intensity near {200} (Figure 4–13 b), cyan) reports on the occupancy of the strongly-coupled Γ-E_{2g} mode at early times, and exhibits a slower rise (430 fs) than the K-A_1' mode. For comparison the Γ-E_{2g} phonon population determined using TRR [9] is shown in grey. The red curve (K-A_1') is nearly identical to the grey curve (Raman: Γ-E_{2g}) in terms of rise time and recovery. They both indicate a rapid increase in optical phonon population due to strong electron-phonon coupling and then a subsequent depopulation of these optical modes via phonon-phonon coupling and relaxation to lower frequencies. Thus, the measurement of strongly coupled optical mode population dynamics appears qualitatively consistent for both UEDS and TRR. The slower rise time observed for the Γ-E_{2g} phonon by UEDS is likely due to the

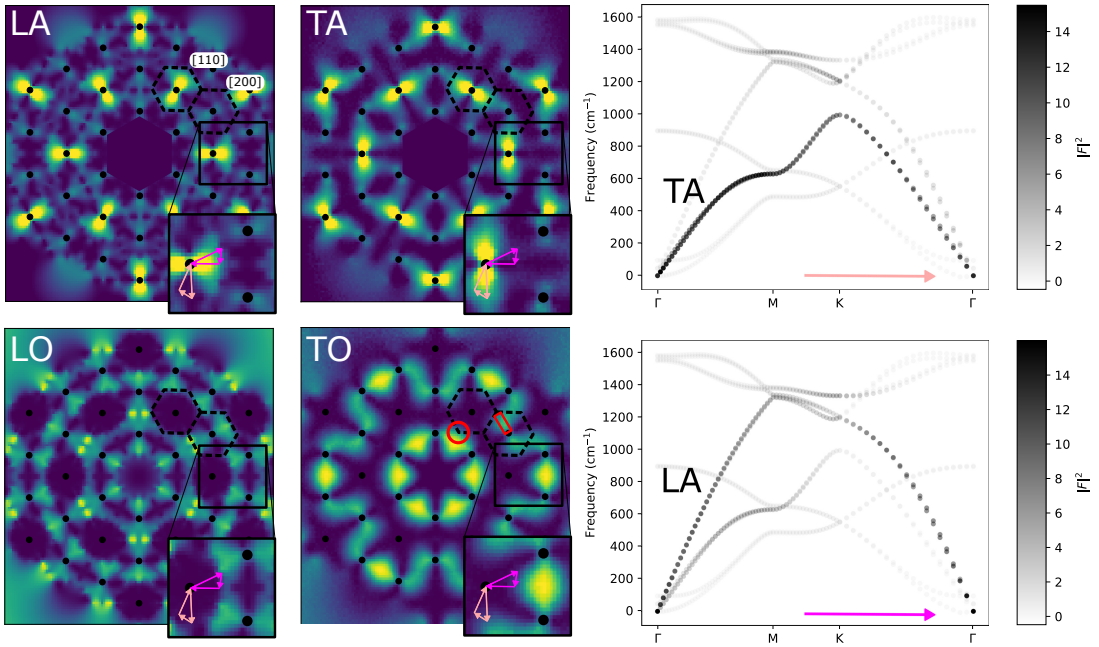

Figure 4–12: Visualizing momentum dependance of one-phonon structure factors. (Left) Numerically computed structure factor maps for the acoustic modes in graphite. TO mode activity matching the early diffuse scattering features in Figure 4–11(c) is outlined in red. The shape of the TA mode activity features match the shape of the diffuse scattering features after 5 ps in Figure 4–11(e-f). (Right) Phonon dispersion curves weighted by structure factor. The darker curves have stronger structure factors along the paths indicated in the structure factor map insets, allowing the mode activity to be easily determined along high symmetry lines and at high symmetry points (note that light grey is zero for these curves). Along the magenta path, for example, the LA mode is active along both Γ-M and Γ-K lines where the LA mode is only active on the Γ-K line. In contrast, the TA mode is the only dominant mode along most of the pink path. The paths with only one dominant mode indicate where single mode occupancy dynamics can be extracted directly via Eq. 2.30.

higher excitation conditions used (12 mJ/cm^2 compared to 0.2 mJ/cm^2) which is known to weaken the Kohn anomaly and electron-phonon coupling at the Γ point [9, 98]. Although the Γ-E_{2g} mode is also strongly coupled, the recovery

evident in the red and grey curves is not seen in cyan. This difference is due to scattering from the low-frequency LA and TA phonon modes involved in the dominant decay channel of the K-A_1' phonon (Figure 4–9) and discussed further below. These LA/TA modes are not seen in the TR-Raman study, nor do they overlap with the signals measured at the K-point [10].The effective temperature of the $K-$point TO mode can be estimated using the measured increase in diffuse intensity and applying Bose-Einstein statistics to the mode population (Equation 1.8).The effective temperature of the $K-$point TO mode is $\sim$ 1150 K by 1 ps, and by 10 ps it has cooled back down to $\sim$ 500 K. The strongly-coupled TO modes reach a pre-equilibrium with the laser-generated carriers in $<$ 1 ps, while all other phonon modes remain at or near room temperature on this timescale.

4.5 Acoustic modes

The character of the differential diffuse scattering pattern changes dramatically through Figure 4–11 c-f) as the non-equilibrium phonon distribution evolves, demonstrating profound sensitivity to the details of the phonon occupancies. The diffuse scattering patterns in Figure 4–11 c-e) reveal the decay channels for the population of strongly-coupled optical phonons as they relax. The time-scale separation between the electron-phonon coupling into K-A_1', Γ-E_{2g}, and the LO branch ($200 - 400$ fs) and the subsequent decay out of these modes ($1 - 3$ ps) means that the diffuse scattering pattern at 1.5 ps effectively maps their momentum-dependent decay probability of the strongly-coupled optical phonons in a manner analogous to the way in which the 0.5 ps pattern indicates the relative electron-phonon coupling strength. The dominant decay channels determined by density functional

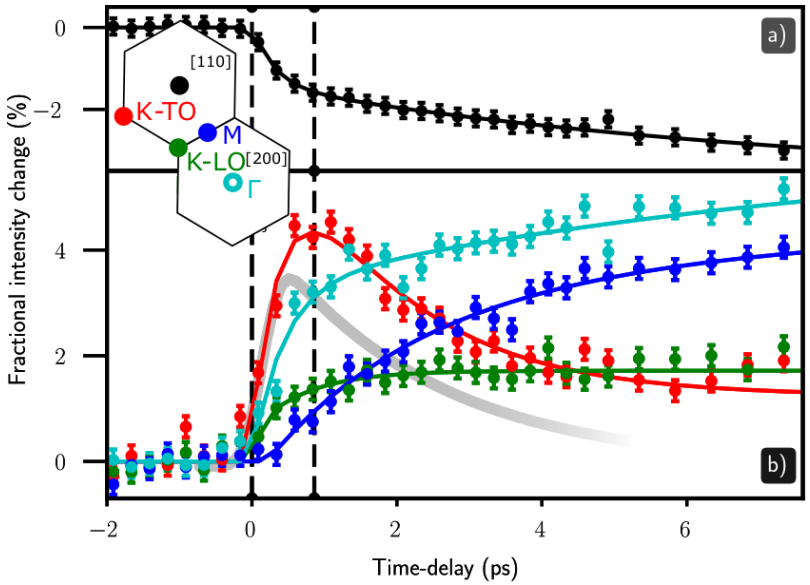

Figure 4–13: Ultrafast electron diffuse scattering at early times. a) Intensity of the [110] Bragg peak showing non-exponential Debye-Waller dynamics [13]. b) $\Delta_f I(\vec{q},\tau)$ at select points in the BZ (inset) and the E_{2g} occupancy dyanamics measured with TR-Raman[9] shown in grey. The rate of increase in the the population of the TO K-A_1' phonon from electronic coupling (red, 280 fs) is faster than that for the Γ-E_{2g} (cyan, 430 fs) and matches the fast Bragg peak dynamics. The population K-LO phonons (green, 730 fs) rises much slower that both TO K-A_1' and Γ-E_{2g} phonons. The rise in diffuse intensity at the M-point (blue, 2.1 ps) is almost an order of magnitude slower than that associated with the TO K-A_1' phonon. The slow timescale decay evident in the Bragg peak and reported in earlier ARPES measurements [14] does not emerge from the dynamics of any single mode, but is a composite of the decay in population of the strongly coupled optical modes (e.g. red, 1.7 ps) and the increase in population of all other modes.

theory [24] (Figure 4–9) compare well with $\Delta I(\vec{q},\tau = 1.5$ ps) in Figure 4–11 c). The hexagonal distribution of diffuse intensity approximately halfway between Γ and the BZ edges is associated with the TA-LA (green) and E_{2g}:LA-LA (red) decay channels.

By 5 ps, the strongest scattering has moved from the Γ-K to the Γ-M lines perpendicular to the scattering vector (Figure 4–11(e)) and the diffuse intensity features have entered a quasi steady state. Here the generalized diffuse scattering selection rules (Section 2.7) may be employed to deduce the final modes of the photoexcitation cascade. By the first selection rule, the diffuse scattering features perpendicular to the Bragg scattering vector $\vec{H}_{110}$ must be scattering from a transverse mode ($k \perp H$) and by the third selection rule this must be an acoustic mode (near the bright [110] Bragg peak). The corresponding weighted dispersion curve (Figure 4–11 pink path) confirms the dominant TA mode and also shows that it also dominates along the entire Γ-M line. There is also strong scattering along the Γ-M and lines near the [200] peak. By consulting the weighted dispersion curves, both the TA and TO modes could be scattering here. These results support the conclusion is that by 5 ps most of the increased phonon population is in the TA mode. In fact, the shape of the features in the 500 ps differential diffuse scattering pattern Figure 4–11(f) match those present in the TA mode structure factor map in Figure 4–12. From 5-100 ps, the pattern relaxes into tighter Γ-M lines, indicating a further increase in TA mode occupancy and a decrease in other in-plane modes. As stated in section 4.2, there are no three phonon anharmonic decay processes that start in a purely transverse mode due to momentum and energy conservation[11, 12]. So a buildup of population in the TA mode reaching a steady state is to be expected.

More details of the phonon relaxation are shown in transient differential phonon population spectra along single mode dominant symmetry lines in Figure

4–14. These curves are determined from the differential intensity profiles measured at selected time delays, normalized by the factors given by Equation 2.30 and represent an unprecedented measure of phonon decay in intricate detail. The difference spectra here robustly represent the nonequilibrium phonon dynamics in the LA/TA branches since they are taken along momentum lines where scattering from other modes is negligible. This is evident in the weighted dispersion curves shown in Figure 4–12. At times < 1.5 ps, there is a large peak Figure 4–14(c) near the K point. Here, the TO mode is active as shown in the weighted dispersion curve in Figure 4–11. This rapid effect is attributed to electron phonon coupling also seen in Figure 4–11(c). The second fastest peak occurs in the LA phonon spectrum at around $\sim 0.5K$ at 2.5 ps followed by other mid-BZ peaks in the TA spectra at 5 ps. These peaks occur due to relaxation of the strongly coupled optical modes to mid-BZ phonons, as discussed above, and shown with blue arrows in Figure 4–14. It is clear from these spectra that the anharmonic coupling to the LA mode is significantly faster than the TA mode. This is in qualitative agreement with previously reported density functional theory (DFT) predictions of the decay probability of the strongly coupled E_{2g} mode to the LA (23%) and TA (16%) modes [24]. Subsequent decay of the acoustic modes is indicated by red arrows in Figure 4–14. The LA mode occupancy decays evenly across the Γ-K line as the TA mode continues to be populated at momenta approaching the Γ point along both symmetry lines. At late times the behaviours of the TA spectra diverge. Along the Γ-K line $> 0.5K$, phonons are funnelling out while TA population increases on the Γ-M line $> 0.5M$. As previously noted, purely

transverse modes, *i.e.* TA modes in the long wavelength limit, have no allowed interband decay pathways, which is consistent the buildup and steady state behaviour of the TA modes near Γ. The different behavior of the modes on the BZ edge corresponds with DFT computations of anharmonic decay lifetimes that report steadily increasing lifetimes for TA modes along Γ-M and constant lifetimes along Γ-K [25]. The lower frequencies of the Γ-M modes compared to those on Γ-K could also contribute to this behaviour. All spectra reach a steady state by around 100 ps. Dotted lines indicate approximate equilibrium difference spectra between a room temperature and an elevated (500 K) temperature graphite lattice, and are in qualitative agreement with the steady state phonon spectra.

These results constitute a unique and powerful and view of phonon dynamics, previously inaccessible though experimental means, that compliment other pump-probe techniques by directly observing electron-phonon and phonon-phonon coupling through the changes in occupancy of individual phonon modes across the BZ. The method for measuring differential phonon population spectra established in Chapters 1 and 2 have been presented and demonstrated for the case of graphite, showcasing the rich and complex phonon dynamics hidden in the diffuse scattering data. In the next chapter, the UEDS method will be used on a very different 2D material, $TiSe_2$, to investigate electron-phonon coupling in a completely different way; by observing the effect of photoexcitation on the renormalized phonon frequencies at characteristic CDW momenta.

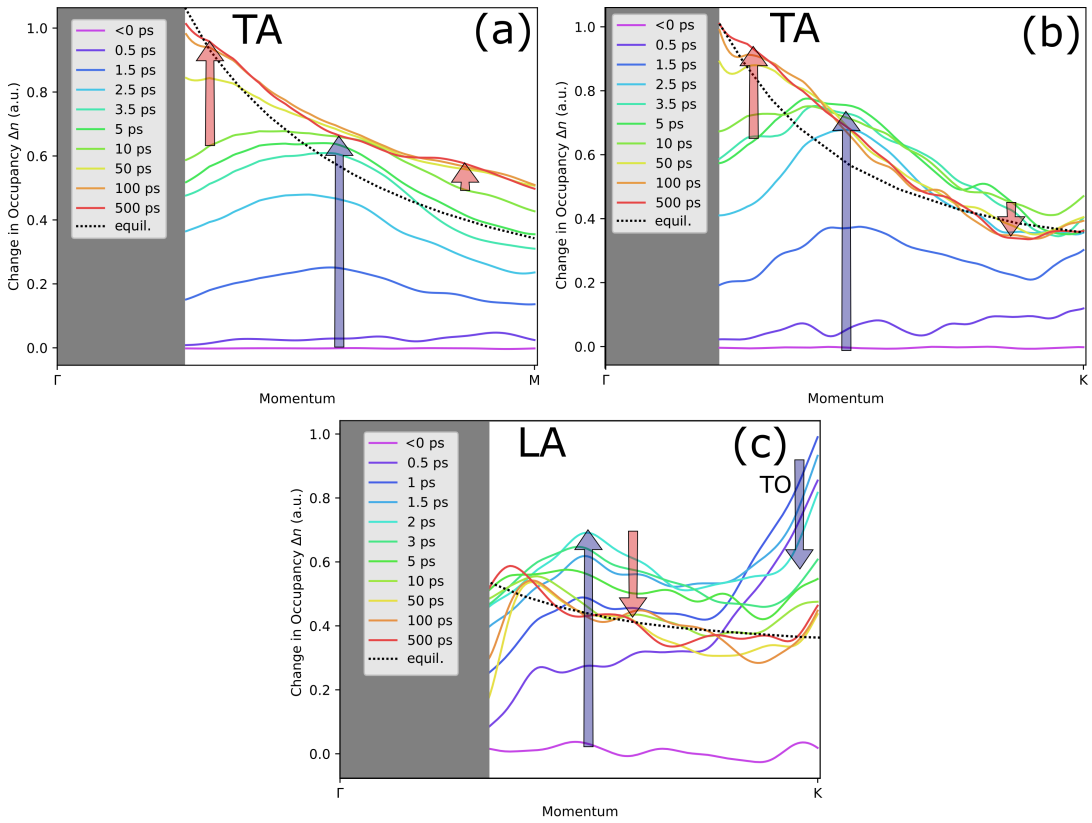

Figure 4–14: Transient differential phonon population spectra. Blue arrows indicate anharmonic decay from optical modes to mid-BZ acoustic modes. Red arrows indicate inter and intraband decay of acoustic modes. (a) TA occupation dynamics along the Γ-M line. By 5 ps, a peak appears around $0.5M$. Population then collects near Γ and M points.(b) (a) TA occupation dynamics along the Γ-K line. In contrast with (a), the population decreases near the BZ edge. (a) LA occupation dynamics along the Γ-K line. The rapid increase near K is due to the TO mode which strongly couples to the photoexcited electron system and has a significant structure factor at these scattering vectors 4–11(lower right). Subsequently, LA mode population decreases everywhere along the Γ-K line.

CHAPTER 5
Phonon renormalization in titanium diselenide

Titanium diselenide is a member of the family of materials known as transition metal dichalcogenides (TMDs). These materials have a crystal structure in which a transition metal atom such as molybdenum, tungsten or titanium is sandwiched between two layers of group 16 (chalcogen) atoms such as sulphur, selenium or tellurium. Because bulk crystals are formed of monolayers a few angstroms thick bound by Van-der-Waals interactions, they are considered 2D materials like graphite and graphene. The members of the TMD family demonstrate a great variety of exotic properties, and have been the subject of intense study. Like graphite, bulk TMDs can be exfoliated into single or few-layered structures by physical or chemical means [99]. Due to quantum confinement and surface effects, monolayer and few-layered TMDs exhibit properties not present in their bulk counterparts. For example, a population of carriers can preferentially lie in one of two or more minima in the conduction band. This phenomenon is called valley polarization and has been observed to be dynamically controlled by optical pumping in monolayers of MoS_2, an effect that is crucial for engineering valley-based electronic and optoelectronic devices [100]. Other applications include photovoltaic devices, energy storage, hydrogen evolution catalysis, transistors, photodetectors, DNA detection, and memory devices [101, 102]. This work is concerned with 1T-$TiSe_2$, a well studied TMD which has a charge density wave transition at $\sim$ 200 K, forming a

$2a \times 2a \times 2c$ superlattice in the bulk. The nature of the transition is the subject of debate and been attributed variably to excitonic interaction [15, 103, 104] and a phonon driven Pierels-like phase [16, 105]. Here, the early results from a UEDS study of 1T-$TiSe_2$ will be presented. Unlike the study of graphite, which focused on the occupancy dynamics of individual phonon modes, these results demonstrate an extremely rapid change in renormalized phonon frequency that provides an unprecedented measure of the Lindhard response at the BZ edge and insight into the nature of the CDW transition.

5.1 Properties of $TiSe_2$

As in the previous chapter, the details of the atomic structure will be presented to enable the calculation of the phonon dispersion and polarizations. The structure of 1T-$TiSe_2$ is shown in Figure 5–1, showing two stacked unit cells with lattice constants $a = 3.536$ Å , $c = 6.004$ Å [15]. The expression for the lattice and reciprocal lattice vectors in terms of a and c are the same as in graphite (see Equations 4.1 and 4.2). The locations of the atoms in Cartesian and lattice coordinates are given in Table 5–1.

Basis	$\vec{r}_{\mathrm{Ti}}$	$\vec{r}_{\mathrm{Se},1}$	$\vec{r}_{\mathrm{Se},2}$
Cartesian	[0, 0, 0]	$\left[0, \frac{a}{\sqrt{3}}, \frac{c}{4}\right]$	$\left[\frac{a}{2}, \frac{a}{2\sqrt{3}}, \frac{3c}{4}\right]$
Lattice	[0, 0, 0]	$\left[\frac{1}{3}, \frac{2}{3}, \frac{1}{4}\right]$	$\left[\frac{1}{3}, -\frac{1}{3}, \frac{3}{4}\right]$

Table 5–1: Atomic positions in $TiSe_2$ with Cartesian and lattice coordinates.

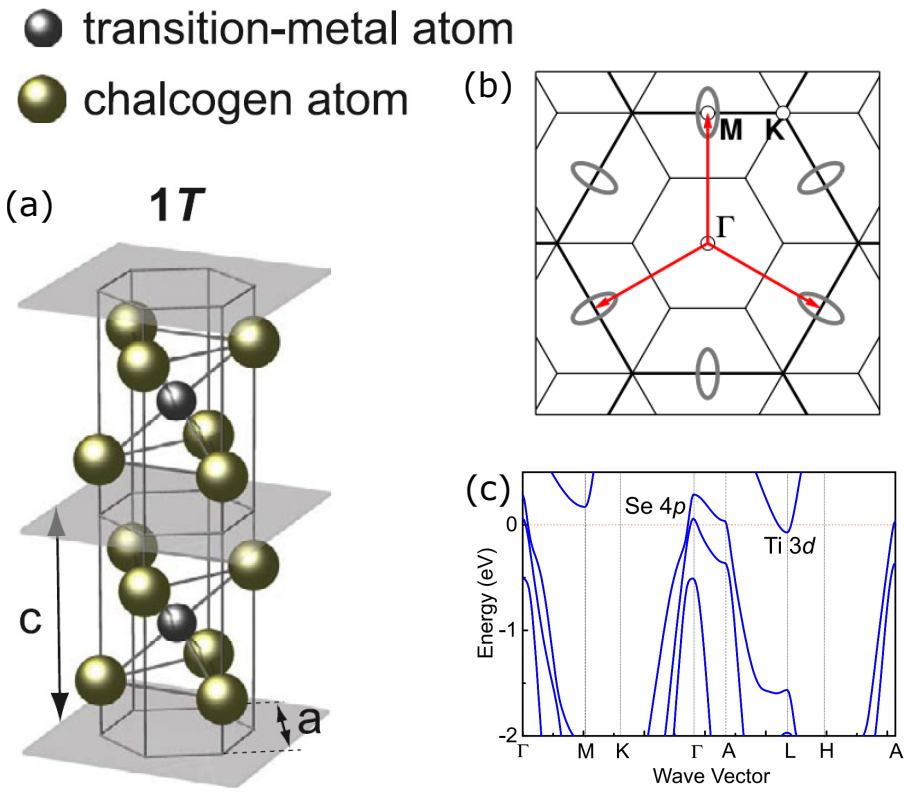

Figure 5–1: The structure of $TiSe_2$. (a) Atomic configuration of two stacked unit cells. (b) Brillouin zones in the normal phase (thick outline) and the CDW phase (thin outline). Red arrows indicate the in-plane wavevectors of the CDW and the gray contours illustrate the topology of the equi-energy contours. (c) Electronic structure in the normal phase. There is an indirect band gap across Γ to M and a negative indirect band gap across Γ to L. Excitonic behaviour at these wave vectors provides an alternate mechanism for the CDW transition. Figures taken with permission from References [15] and [16]

.

At temperatures around 200 K, 1T-$TiSe_2$ undergoes a second-order phase transition to a commensurate $2 \times 2 \times 2$ CDW phase [15]. There are two competing explanations for the CDW transition. The first proposed mechanism is consistent with the concepts presented in Section 1.5, where the transition is enabled by a

strong electron-phonon coupling constant g and a Kohn anomaly at the M and L high symmetry points arising from nested vectors at the Fermi surface. Evidence of the strength of g in $TiSe_2$ includes the large amplitudes of the periodic lattice distortion in the CDW phase and high electrical resistivity (roughly 50 times larger than Cu) above the transition temperature [15]. A schematic of degenerate band surfaces in the BZ, and therefore the CDW wave vectors, are shown in Figure 5–1(b). These properties all suggest a Peierls-like periodic lattice distortion, however it has been argued that the nesting of the Fermi surface is not clear [106]. The calculated electronic band structure is shown in Figure 5–1(c). Here, the nesting at the Fermi surface is not obvious compared to the Dirac cones of graphite. An alternate explanation is that the transition is mediated by excitons (electron-hole quasi-particles) that occur due to the indirect band gaps in the electronic structure. With sufficient electron-hole coupling, the system is unstable to the formation of excitons and deforms with a periodicity governed by the wave vector connecting them; which in the case of $TiSe_2$ leads to a doubling of the lattice spacing. [103, 106].

Figure 5–2 shows simulated phonon dispersions of $TiSe_2$ demonstrating the predicted effect of electron temperature on the severity of the Kohn anomaly at the M and L points. These results were computed using *ab initio* methods and also predict the CDW transition temperature when the phonon is renormalized to zero frequency [107]. In order to simulate the change in electron temperature, the Fermi-Dirac distribution is used to smear the electronic functions, where the smearing factor takes on a physical meaning to directly reflect the electronic

temperature [108]. As the smearing decreases the renormalized TA phonon frequency tends towards zero, where the CDW transition occurs as described in Section 1.5. This also indirectly characterizes the temperature dependence of the the Lindhard response function $\chi(\vec{q}, T)$ via Equation 1.21.

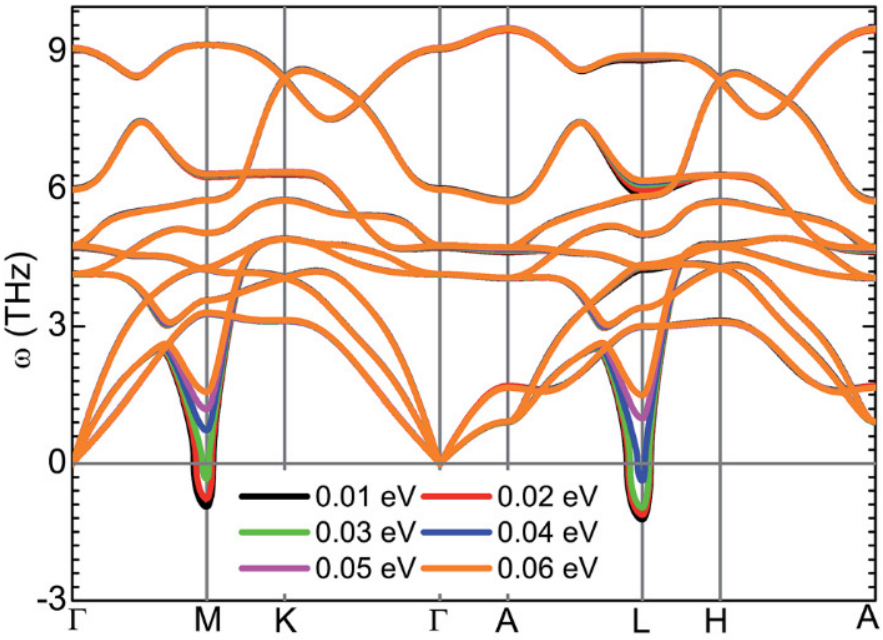

Figure 5–2: Simulated phonon dispersion curves of $TiSe_2$, showing the severity of the TA mode renormalization as a function of temperature. In order to quantitatively calculate the CDW transition temperature, the Fermi-Dirac distribution is used to smear the electronic functions, where the smearing factor takes on a physical meaning to directly increase the electronic temperature and has the effect of increasing the TA phonon frequency at the M and L points.

5.2 UEDS results

There are a number of salient differences between UEDS methodology applied to $TiSe_2$ and graphite due to the very different properties of their phonon systems

and electron-phonon interactions. As shown in figure 5–2, the TA phonon renormalization at the M and L points are very sensitive to electronic temperature, so photoexcitation has a substantial effect on phonon frequency. The resulting phonon hardening will appear as a negative differential in the diffuse intensity signal (Equation 2.28) which appear at the M and L points where the TA mode is active. Moreover, the L point is not in the normal diffraction plane, so the electron pulse must be oriented at an angle relative to the sample such that the L points are visible in the diffraction pattern. The improvements to the sample manipulation shown in Section 3.5 allow this to be done. Therefore, these experiments focus on measuring transient phonon frequency renormalization by measuring UEDS signals at two angles; perpendicular to [001] (sample normal) and $[10\bar{1}]$ to view the effect of diffuse scattering at both M and L points. The experiments were performed by the author with support from Martin Otto and the analysis and discussion are solely the work of the author.

The $TiSe_2$ thin film samples used for this experiment were made using crystals purchased from hq Graphene®. The bulk crystals were mechanically sliced into 90 nm thin films by ultramicrotomy [109] performed by technicians at the Facility for Electron Microscopy Research at McGill University. The configuration for the UEDS experiment was the same as the experiments on graphite except the direct synchronization for the RF cavity was implemented [36] improving the effective temporal resolution as well as the upgraded sample manipulation and beam geometry described in Section 3.5. The pump pulses were 800 nm and 35 fs long with a fluence of 4 mJ/cm^2.

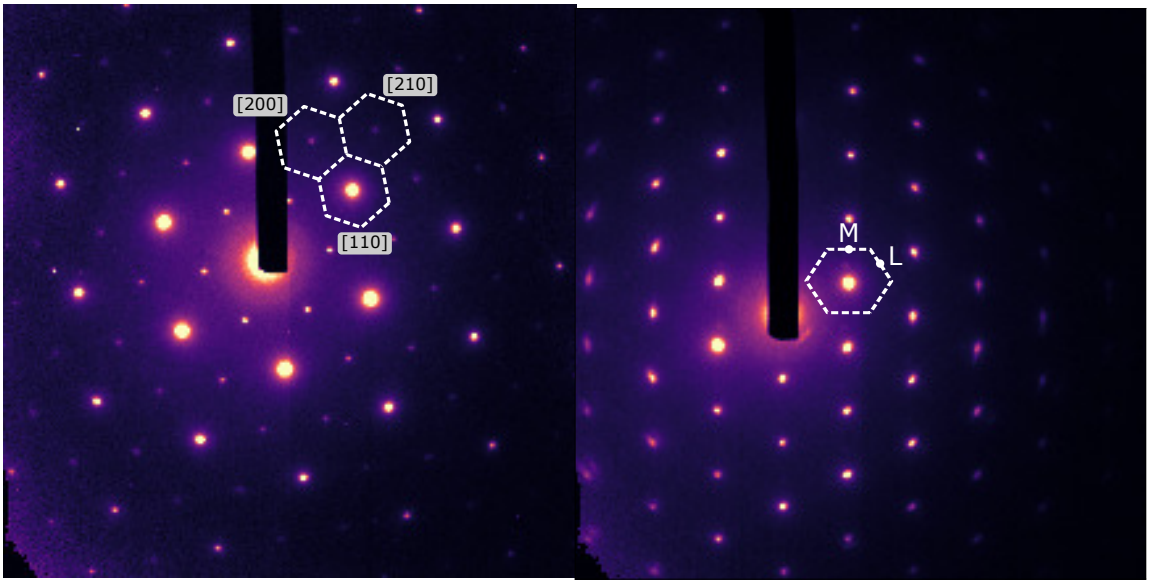

Figure 5–3: Static diffraction patterns of $TiSe_2$. (Left) Diffraction at normal incidence along [001]. Select BZs indicated by reciprocal lattice coordinates. (Right) Diffraction along $[10\bar{1}]$, the BZ edge is indicated with M and L high symmetry points.

Figure 5–3 shows the raw diffracted intensity when the sample is positioned normal to the electron beam and at an angle of 30.5° in order to look at the $[10\bar{1}]$ plane of reciprocal space which includes the L-point. The time resolved fractional intensity results at normal incidence are presented in Figure 5–4. The data has been six-fold rotationally averaged and smoothed with a 4 pixel (0.03 $Å^{-1}$) Gaussian kernel. As in the previous chapter, the data is normalized by the scattering vector squared q^2. An important distinction between these maps and those of the previous chapter is that the colormap has been inverted so green shows a decrease in diffracted intensity. For graphite, all of the diffuse scattering differentials are positive, so the negative signal seen at select M-points at 0.5 ps

and 1 ps represents a completely different physical phenomena then any of those discussed in the last chapter. These negative diffuse scattering peaks, or dips in intensity, form a gear-like shape surrounding the bright family of [110] peaks and is repeated at higher orders. By 2 ps, the intensity dip has completely dissipated and the remainder of the negative signal is located at the Bragg peaks due to Debye-Waller suppression. The positive (blue) signals lack the defined structure of the graphite diffuse scattering patterns and are more or less constant after a 2 ps rise. Due to the constant and unstructured signals at later time delays the discussion will focus on the signals in the first few picoseconds after photoexcitation.

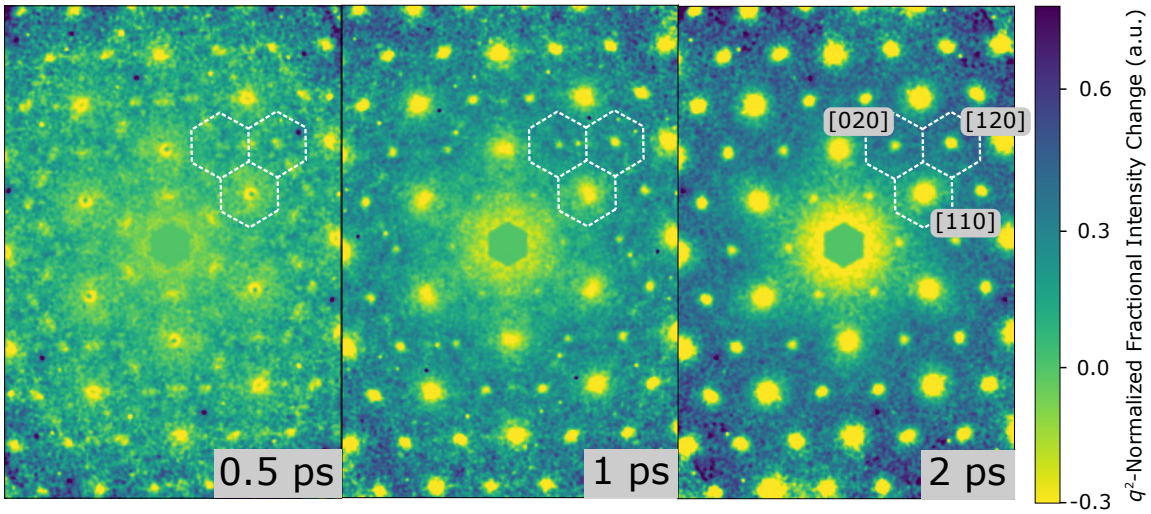

Figure 5–4: Evolution of $\Delta_f I(\vec{q}, \tau)$ following photo-excitation of $TiSe_2$. By 0.5 ps, negative diffuse scattering features (green) appear at M-points surrounding the [110] family of peaks forming a gear-shaped pattern. Through 1 and 2 ps, the M-point signals fade into a uniform diffuse scattering increase at all points away from the Bragg peaks.

5.3 Impulsive phonon hardening

The details of the early time scale dynamics at various high symmetry points is shown in Figure 5–5(b). All curves show an increase in diffuse scattering that occurs in the first 2 ps after photoexcitation; matching the fast component of the Debye-Waller suppression of the Bragg peaks (Figure 5–5(a)). This is the expected general behaviour of the phonon occupancy after coupling with the hot carriers induced by the pump pulse. The distinctive feature of these curves is an extremely fast dip in diffuse intensity that recovers in about 1 ps at certain M points. A one-phonon structure factor analysis reveals that this dip only occurs at scattering vectors where the TA mode is active and dominant (Figure 5–5(c)). The structure factors were calculated using the methods outlined in section 2.6. Specifically, the PwSCF and PHonon packages of Quantum Espresso were applied using a $4 \times 4 \times 2$ k-point grid, ultrasoft pseudoptoentials for titanium and selenium (wavefunction energy cutoff of 70 Ry) and BLYP exchange correlation potentials [45, 46]. This is the same M point mode that has a renormalized frequency dependent on electronic temperature in the simulations shown in Figure 5–2. The time scale of the onset of the TA mode dip appears to be nearly impulsive; at least as fast as the time resolution of the instrument, matching the time scale of temperature thermalization and carrier-carrier interactions [6]. The changes in the electron temperature from photoexcitation will produce the same phonon renormalization as the *ab initio* simulations shown in Figure 5–2. Therefore, through the inverse dependance of diffuse intensity on phonon frequency shown in Equation 2.24, the dip can be attributed to the renormalization (hardening) of the TA mode

phonons at the M-point via Equation 1.21. In this way the behaviour of the Lindhardt response function $\chi(\vec{q}, T)$, and therefore the transient electronic structure is being measured.

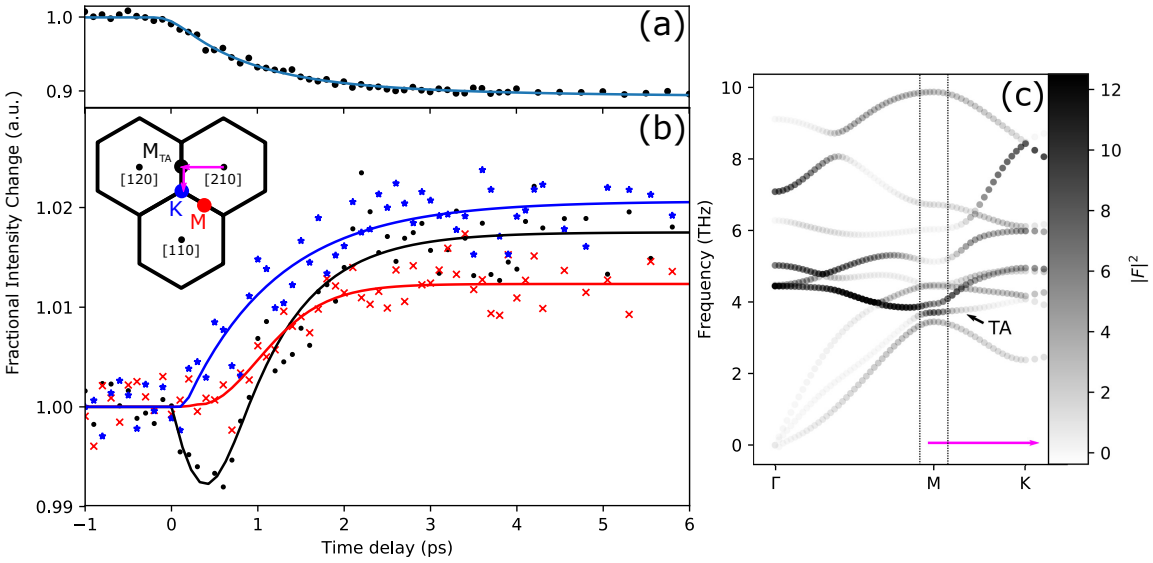

Figure 5–5: Fractional scattered intensity changes. (a) Bragg peak dynamics showing showing Debye-Waller suppression. (b) Diffuse scattering dynamics at high symmetry points. All three curves increase during the first 2 ps after photoexcitation, corresponding to an overall phonon occupancy increase due to coupling with photoexcited electrons. An extremely fast dip in diffuse intensity that recovers in about 1 ps appears at M points where the TA mode is active and dominant as shown in the computed weighted dispersion curve (c).

The difficulty in obtaining this measurement should not be understated. It is a testament to the exceptional signal-to-noise and time resolution of the UED instrument that a $< 1\%$ change in *diffuse* scattering with a nearly instantaneous onset and a recovery within 1 ps was clearly measured. Unfortunately, the effect could not also be measured L point as angled UED experiments have additional challenges. First, the six-fold symmetry of the normal diffraction plane is not

present normal to $[10\bar{1}]$ reducing the signal-to-noise by a factor of $\sqrt{6}$. Additionally, the electron pulse striking the sample at an angle causes the electrons to probe at different times/moments regions of the sample surface, which are excited simultaneously by the pump pulse. Thus, a mismatch in group velocities affects the overall time resolution [110]. Nonetheless, the measurement at the M-point represents the first experimental study of phonon renormalization with non-zero momenta. The measured effect on the phonon frequency is qualitatively predicted by the linear response theory described in Section 1.5 and is consistent with the nested Fermi surface picture of the CDW transition.

5.4 Conclusions and outlook

UEDS provides a unique and unprecedented vantage point from which photoexcitation dynamics can be observed. By providing a detailed look at the ultrafast changes in phonon occupancy, unrestricted by wave vector or symmetry, the strength of electron-phonon interactions in graphite can be viewed not only at the high symmetry points but across all of momentum space. The anharmonic decay of the strongly coupled optical modes the subsequent acoustic mode decay channels, processes that were previously explored only through simulation, can be followed in detail at any point of the Brillouin zone. Minuscule and impulsive phonon frequency renormalization can be detected in the form of scattering differentials that are 1% of a signal 10^4 times smaller than elastic scattering. UEDS is also profoundly complementary to trARPES and TRR which give similar measurements of electronic occupancy dynamics and Γ-point phonon dynamics,

providing a complete picture of the events following photoexcitation from the perspective of both electron and lattice systems.

Even so, the experiments shown here are very limited in scope compared to the potential of UEDS as a technique. Graphite is the perfect test sample, not only because it is a well studied material, but it has extremely hard (high frequency) vibrational modes resulting low occupancy at room temperature. This causes the occupancy dynamics to be more dramatic and easier to measure. Other materials, including $TiSe_2$, would greatly benefit from the ability to perform UEDS on samples at low temperatures. Moreover, one would expect the signal from the TA mode renormalization in $TiSe_2$ to become much larger near the charge density wave transition temperature. Future UED studies could measure the periodic lattice distortion melt in real time via the Bragg peak dynamics, while simultaneously measuring changes in the phonon frequency and occupancy, perhaps shedding light on the true nature of the CDW transition.

UED instruments and techniques continue to evolve with higher electron pulse brightness, shorter electron pulses, larger and faster detectors, and improved configurations. Eventually, the signal-to-noise and detection area may reach the level needed to measure the diffuse scattering at dozens of scattering vectors all with equivalent reduced wave vectors. In this case the matrix solution for all phonon occupanices derived in Section 2.6, could be found. This would provide complete knowledge of time-resolved phonon behaviour for all modes and all momenta, perhaps revealing the mechanisms behind the many ordered phases and

diverse electronic and thermal properties that arise from interplay between electron and lattice systems.

REFERENCES

[1] W. Setyawan and S. Curtarolo, Computational Materials Science **49**, 299 (2010).

[2] D. R. Cooper et al., ISRN Condensed Matter Physics **2012**, 1 (2012).

[3] J. Maultzsch, S. Reich, C. Thomsen, H. Requardt, and P. Ordejón, Physical review letters **92**, 075501 (2004).

[4] E. Hazrati, G. A. de Wijs, and G. Brocks, Physical Review B **90**, 155448 (2014).

[5] T. Kampfrath, L. Perfetti, F. Schapper, C. Frischkorn, and M. Wolf, Physical Review Letters **95**, 187403 (2005).

[6] J. C. W. Song and L. S. Levitov, Journal of Physics: Condensed Matter **27**, 164201 (2015).

[7] J. C. Johannsen et al., Physical Review Letters **111**, 027403 (2013).

[8] A. Stange et al., Physical Review B **92**, 184303 (2015).

[9] H. Yan et al., Physical Review B **80**, 121403 (2009).

[10] M. J. Stern et al., Physical Review B **97** (2018).

[11] M. Lax, P. Hu, and V. Narayanamurti, Physical Review B **23**, 3095 (1981).

[12] A. Khitun and K. L. Wang, Applied Physics Letters **79**, 851 (2001).

[13] R. P. Chatelain, V. R. Morrison, B. L. Klarenaar, and B. J. Siwick, Physical Review Letters **113**, 235502 (2014).

[14] S.-i. Tanaka, M. Matsunami, and S.-i. Kimura, Scientific Reports **3**, 3031 (2013).

[15] K. Rossnagel, Journal of Physics: Condensed Matter **23**, 213001 (2011).

[16] P. Chen et al., Scientific Reports **6**, 37910 (2016).

[17] G. Grimvall, *The electron-phonon interaction in metals*, North-Holland Pub. Co., 1981.

[18] J. Bardeen, L. N. Cooper, and J. R. Schrieffer, Physical Review **108**, 1175 (1957).

[19] B. E. Warren, *X-ray diffraction*, Addison-Wesley Pub. Co., Reading, Mass., 1969.

[20] A. Kotani and S. Shin, Reviews of Modern Physics **73**, 203 (2001).

[21] G. L. Squires, *Introduction to the Theory of Thermal Neutron Scattering*, Cambridge University Press, Cambridge, 2012.

[22] A. Damascelli, Z. Hussain, and Z.-X. Shen, Reviews of Modern Physics **75**, 473 (2003).

[23] D. J. Gardiner, P. R. Graves, and H. J. Bowley, *Practical Raman spectroscopy*, Springer-Verlag, Berlin, 1989.

[24] N. Bonini, M. Lazzeri, N. Marzari, and F. Mauri, Physical Review Letters **99**, 176802 (2007).

[25] L. Paulatto, F. Mauri, and M. Lazzeri, Physical Review B **87** (2013).

[26] C. Burda and M. A. El-Sayed, Pure and Applied Chemistry **72**, 165 (2000).

[27] M. Chollet et al., Journal of Synchrotron Radiation **22**, 503 (2015).

[28] M. Buzzi, M. Först, R. Mankowsky, and A. Cavalleri, Nature Reviews Materials (2018).

[29] B. J. Siwick, J. R. Dwyer, R. E. Jordan, and R. J. D. Miller, Science (New York, N.Y.) **302**, 1382 (2003).

[30] S. Hellmann et al., Nature Communications **3**, 1069 (2012).

[31] J.-A. Yang, S. Parham, D. Dessau, and D. Reznik, Scientific Reports **7**, 40876 (2017).

[32] H. Ihee, Science **291**, 458 (2001).

[33] V. R. Morrison et al., Science **346**, 445 (2014).

[34] R. P. Chatelain, V. R. Morrison, C. Godbout, and B. J. Siwick, Applied Physics Letters **101**, 081901 (2012).

[35] V. R. Morrison, R. P. Chatelain, C. Godbout, and B. J. Siwick, Optics Express **21**, 21 (2013).

[36] M. R. Otto, L. P. René de Cotret, M. J. Stern, and B. J. Siwick, Structural Dynamics **4**, 051101 (2017).

[37] R. O. Jones, Reviews of Modern Physics **87**, 897 (2015).

[38] N. Ashcroft and N. Mermin, *Solid State Physics*, Holt, Rinehart and Winston, 1976.

[39] M. P. Marder, *Condensed Matter Physics*, John Wiley & Sons, Inc., Hoboken, NJ, USA, 2010.

[40] E. Prince, *International Tables for Crystallography*, volume A, International Union of Crystallography, Chester, England, 2016.

[41] L. Falkovsky, Physics Letters A **372**, 5189 (2008).

[42] S. Baroni, S. de Gironcoli, A. Dal Corso, and P. Giannozzi, Reviews of Modern Physics **73**, 515 (2001).

[43] P. Hohenberg and W. Kohn, Physical Review **136**, B864 (1964).

[44] W. Kohn and L. J. Sham, Physical Review **140**, A1133 (1965).

[45] P. Giannozzi et al., Journal of Physics: Condensed Matter **21**, 395502 (2009).

[46] P. Giannozzi et al., Journal of Physics: Condensed Matter **29**, 465901 (2017).

[47] S. Piscanec, M. Lazzeri, F. Mauri, a. C. Ferrari, and J. Robertson, Physical Review Letters **93**, 185503 (2004).

[48] G. Grüner, Density waves in solids, 2000.

[49] W. Kohn, Physical Review Letters **2**, 393 (1959).

[50] J. M. Cowley, *Diffraction physics*, Elsevier Science B.V., Amsterdam; New York, 1995.

[51] R. Xu and T. C. Chiang, Zeitschrift fur Kristallographie **220**, 1009 (2005).

[52] J. J. Thomson and G. P. Thomson, The Journal of Physical Chemistry **38**, 987 (1933).

[53] E. Prince, *International Tables for Crystallography*, volume C of *International Tables for Crystallography*, International Union of Crystallography, Chester, England, 2006.

[54] H. A. Hauptman, Reports on Progress in Physics **54**, 1427 (1991).

[55] R. Colella and B. W. Batterman, Physical Review B **1**, 3913 (1970).

[56] N. S. Orlova, Physica Status Solidi (b) **93**, 503 (1979).

[57] A. H. Zewail, The Journal of Physical Chemistry A **104**, 5660 (2000).

[58] S. Mukamel, Annual Review of Physical Chemistry **41**, 647 (1990).

[59] S. Mukamel, Annual Review of Physical Chemistry **51**, 691 (2000).

[60] E. T. J. Nibbering and T. Elsaesser, Chemical Reviews **104**, 1887 (2004).

[61] N. Tamai and H. Miyasaka, Chemical Reviews **100**, 1875 (2000).

[62] B. Ferguson and X.-C. Zhang, Nature Materials **1**, 26 (2002).

[63] P. Jepsen, D. Cooke, and M. Koch, Laser & Photonics Reviews **5**, 124 (2011).

[64] P. Szymanski, S. Garrett-Roe, and C. Harris, Progress in Surface Science **78**, 1 (2005).

[65] T. Rohwer et al., Nature **471**, 490 (2011).

[66] S. Williamson, G. Mourou, and J. Li, Physical Review Letters **52**, 2364 (1984).

[67] J. Williamson, M. Dantus, S. Kim, and A. Zewail, Chemical Physics Letters **196**, 529 (1992).

[68] B. J. Siwick, J. R. Dwyer, R. E. Jordan, and R. J. D. Miller, Journal of Applied Physics **92**, 1643 (2002).

[69] M. Harb et al., Physical Review Letters **100**, 155504 (2008).

[70] R. D. Miller, Annual Review of Physical Chemistry **65**, 583 (2014).

[71] J. B. Hastings et al., Applied Physics Letters **89**, 184109 (2006).

[72] P. Musumeci, J. T. Moody, C. M. Scoby, M. S. Gutierrez, and M. Westfall, Applied Physics Letters **97**, 063502 (2010).

[73] G. H. Kassier, K. Haupt, N. Erasmus, E. G. Rohwer, and H. Schwoerer, Journal of Applied Physics **105**, 113111 (2009).

[74] R. Boyd, Nonlinear optics, 2008.

[75] R. Chatelain, *Radio-Frequency Compressed Electron Pulses for Ultrafast Electron Diffraction*, PhD thesis, McGill, 2014.

[76] T. van Oudheusden et al., Journal of Applied Physics **102**, 093501 (2007).

[77] A. H. Castro Neto, F. Guinea, N. M. R. Peres, K. S. Novoselov, and A. K. Geim, Reviews of Modern Physics **81**, 109 (2009).

[78] A. A. Balandin et al., Nano Letters **8**, 902 (2008).

[79] A. K. Geim, Science **324**, 1530 (2009).

[80] A. King, G. Johnson, D. Engelberg, W. Ludwig, and J. Marrow, Science **321**, 382 (2008).

[81] M. J. Allen, V. C. Tung, and R. B. Kaner, Chemical Reviews **110**, 132 (2010).

[82] D. D. Chung, Journal of Materials Science **37**, 1475 (2002).

[83] K. S. Novoselov, Science **306**, 666 (2004).

[84] Y. Wei and Z. Sun, Current Opinion in Colloid & Interface Science **20**, 311 (2015).

[85] F. Carbone, P. Baum, P. Rudolf, and A. Zewail, Physical Review Letters **100**, 035501 (2008).

[86] F. Carbone, O.-H. Kwon, and A. H. Zewail, Science (New York, N.Y.) **325**, 181 (2009).

[87] F. Carbone et al., Chemical Physics Letters **468**, 107 (2009).

[88] R. Raman et al., Physical Review Letters **101**, 077401 (2008).

[89] M. Harb et al., Physical Review B **84**, 045435 (2011).

[90] S. Schäfer, W. Liang, and A. H. Zewail, New Journal of Physics **13** (2011).

[91] J. Wang, S. Deng, Z. Liu, and Z. Liu, National Science Review **2**, 22 (2015).

[92] K. F. Mak, M. Y. Sfeir, J. A. Misewich, and T. F. Heinz, Proceedings of the National Academy of Sciences **107**, 14999 (2010).

[93] A. Javey et al., Physical Review Letters **92**, 106804 (2004).

[94] S. Pisana et al., Nature Materials **6**, 198 (2007).

[95] C. H. Lui, K. F. Mak, J. Shan, and T. F. Heinz, Physical Review Letters **105**, 127404 (2010).

[96] D. Brida et al., Nature Communications **4**, 1987 (2013).

[97] T. Winzer and E. Malic, Journal of Physics: Condensed Matter **25**, 054201 (2013).

[98] K. Ishioka et al., Physical Review B **77**, 121402 (2008).

[99] K. F. Mak, C. Lee, J. Hone, J. Shan, and T. F. Heinz, Physical Review Letters **105**, 136805 (2010).

[100] K. F. Mak, K. He, J. Shan, and T. F. Heinz, Nature Nanotechnology **7**, 494 (2012).

[101] H. Li, J. Wu, Z. Yin, and H. Zhang, Accounts of Chemical Research **47**, 1067 (2014).

[102] R. Lv et al., Accounts of Chemical Research **48**, 56 (2015).

[103] J. van Wezel, P. Nahai-Williamson, and S. S. Saxena, Physical Review B **81**, 165109 (2010).

[104] A. Kogar et al., Science **358**, 1314 (2017).

[105] M. Calandra and F. Mauri, Physical Review Letters **106**, 196406 (2011).

[106] T. E. Kidd, T. Miller, M. Y. Chou, and T.-C. Chiang, Physical Review Letters **88**, 226402 (2002).

[107] Z.-G. Fu et al., RSC Advances **6**, 76972 (2016).

[108] D. L. Duong, M. Burghard, and J. C. Schön, Physical Review B **92**, 245131 (2015).

[109] J. J. Bozzola and L. D. T. A. T. T. Russell, Electron microscopy : principles and techniques for biologists, 1999.

[110] F. Pennacchio et al., Structural Dynamics **4**, 044032 (2017).